LATVIAN
JOURNAL
of
PHYSICS
and TECHNICAL
SCIENCES

ISSN 0868 - 8257

6

(Vol. 61)

2024

CONTENTS

LATVIAN JOURNAL of PHYSICS and TECHNICAL SCIENCES

LATVIJAS FIZIKAS un TEHNISKO ZINĀTŅU ŽURNĀLS

Published six times a year since February 1964
Iznāk sešas reizes gadā kopš 1964. gada februāra

6 (Vol. 61) • **2024**

RĪGA

Language Editor: O. Ivanova
Computer Designer: I. Begicevs

INDEXED (PUBLISHED) IN

www.scopus.com
www.sciendo.com
EBSCO (Academic Search Complete, www.epnet.com), INSPEC (www.iee.org.com).
VINITI (www.viniti.ru), Begell House Inc/ (EDC, www.edata-center.com).

Issuers: Institute of Physical Energetics,
Institute of Solid State Physics, University of Latvia
Registration Certificate Number: 000700221

Editorial Contacts:
14 Dzerbenes Street, Riga, LV-1006
LATVIA
tel: +371 26245896
M: +371 29363105
leo@lza.lv

LATVIAN JOURNAL OF PHYSICS
AND TECHNICAL SCIENCES
2024, N 6

DOI: 10.2478/lpts-2024-0040

MODELLING SUITABLE LAYOUT FOR A SMALL ISLAND HARBOUR: A CASE STUDY OF RUHNU IN THE GULF OF RIGA, EASTERN BALTIC SEA

R. Männikus[1*], W. W. Wang[2], M. Eelsalu[1],
F. Najafzadeh[1], H. Bihs[2], T. Soomere[1,3]

[1]Wave Engineering Laboratory,
Department of Cybernetics, School of Science,
Tallinn University of Technology,
Ehitajate tee 5, 19086 Tallinn, ESTONIA
[2]Norwegian University of Science and Technology,
1 Høgskoleringen Str., Trondheim, 7034, NORWAY
[3] Estonian Academy of Sciences,
6 Kohtu Str., Tallinn, 10130, ESTONIA
[*] e-mail: rain.mannikus@gmail.com

We explore the complexity of various drivers and local constraints from the viewpoint of developing a feasible re-design of a small harbour that is affected by ultra-refraction of storm waves. Waves propagating towards the Port of Ruhnu on a small island in the central part of the Gulf of Riga are systematically redirected by underwater features so that saturated waves in virtually all storms propagate almost exactly into the harbour entrance. A new design of the port entrance and associated set of breakwaters is largely steered by the location of the port and options for the fairway into the port. The re-design of the breakwaters and possible relocation of the entrance considers the specific features of the local wind, wave, and water level climate, including period-depending refraction of storm waves. We present systematic analysis of these aspects using recorded and modelled wind and water level time series. Wave properties are reconstructed using the WAVE module (SWAN) of the Delft3D suite forced with ERA5 and local wind information. Phase-resolving modelling of waves (REEF3D software) reveals the presence of a bi-modal wave field in the interior of the port and provides alternatives for the design of effective protection options that suppress single wave components. On many occasions, greatly simplified models and local one-point wind properties provide even better match with recorded wave properties than sophisticated models and global data sets.

Keywords: *Breakwater design, Delft3D, port planning, REEF3D, SWAN model, wave modelling.*

1. INTRODUCTION

A harbour has to provide protection for the vessels against the impact of wind, waves and currents, and sometimes against large variations in the water level. This is usually achieved by a combination of choice of the layout of the harbour and characteristics of its structures. However, the situation gets more complicated when there is a possible sediment movement nearby. Wave and current-driven sediment transport can turn a perfectly sheltered harbour or waterway into an expensive maintenance project (e.g., [1]–[3]). Additionally, several other conditions (accessibility on land and on water, man-made objects etc.) must be considered for an optimal harbour design ([4], [5], among many others). As virtually every port is unique, modern port design covers a wide range of different aspects of planning, and management and case studies offer great insights to understand them.

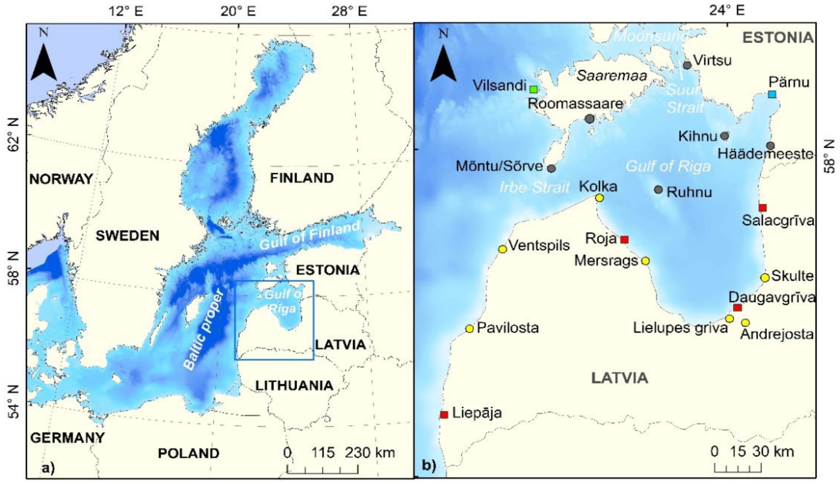

Fig. 1. Location scheme of the Gulf of Riga in the eastern Baltic Sea (left) and the island of Ruhnu in the Gulf of Riga (right). The right panel shows the locations of water level stations in Latvia (red and yellow) used in the analysis.

The Port of Ruhnu (called Port of Ringsu or colloquially Ringsu harbour in the past [6]) is situated on the southern tip of a small island of Ruhnu in the middle of the Gulf of Riga (Fig. 1). Wave fields in this water body are mostly locally generated and follow the wind patterns [7]. Only a small amount of wave energy generated in the Baltic proper penetrates into the Gulf of Riga through Irbe Strait and affects to some extent the northern part of the gulf. The "climate" of waves of appreciable height is driven by a two-peak wind regime in this region. Moderate and strong winds blow usually either from the south-west (SW) or (less frequently) from the north-north-west (NNW) [8], [9]. The port is sheltered against waves from the NNW by the island itself. It is protected against waves from the SW and refracted waves from the northern directions by two rubble mound breakwaters. To enhance the protection, the tip of the southern breakwater is turned to the south-east. The entrance and waterway to the port are oriented to the south-east (SE). This is the direction from where winds are infrequent and weak [8], [9].

Despite this careful design that considers the directional structure of predominant moderate and strong wind, inconveniently high waves often penetrate into the port interior that also suffers from rapid changes in the water level. The situation is especially difficult in the narrow entrance channel where a vessel entering the port may experience strong bow waves. Undesirable wave conditions often occur even during westerly and northerly winds against which the harbour is geometrically protected. A likely reason for such conditions is refraction of wind waves. Namely, waves excited in the Gulf of Riga at wind speeds of 10–15 m/s eventually undergo extensive refraction on underwater slopes of the island of Ruhnu and possibly its neighbouring shallow area. This process systematically redirects waves so that intense waves may propagate directly into the entrance of the Port of Ruhnu during virtually any strong wind event as described in detail in [6].

The refraction-induced rotation of wave propagation direction is relatively mild for weak winds but becomes more effective for strong winds [6]. This feature simply reflects an increase in the wave period and length under stronger winds as longer waves are more affected by refraction. Interestingly, the range of wave approach directions converges around 120° (clockwise from the North) for a wind speed of 15 m/s. This is exactly the orientation of the fairway that enters the port [6]. Such ultra-refraction is not unique and is known, e.g., for SW swells propagate into San Francisco Bay [10].

Another long-term issue for the Port of Ruhnu has been an accumulation of sediments (sand) at the harbour entrance. It is not clear where the sand is coming from. An estimate of sediment transport based on archive documents about coastal processes, the appearance of morphology of the beaches next to the port and nearby coasts concluded in the 1990s that the fine sand was coming from the north along the eastern coast of Ruhnu [11] (Fig. 2). Hence, an extension of the northern breakwater was proposed. However, due to costs, it was built shorter than necessary and sand accumulation continued. The port authorities addressed the problem by dredging the sand and placing it to the west of the port where a sandy beach was located (Fig. 3). As sand accumulation continued, it was hypothesised that sediment transport from the west could also be its possible reason.

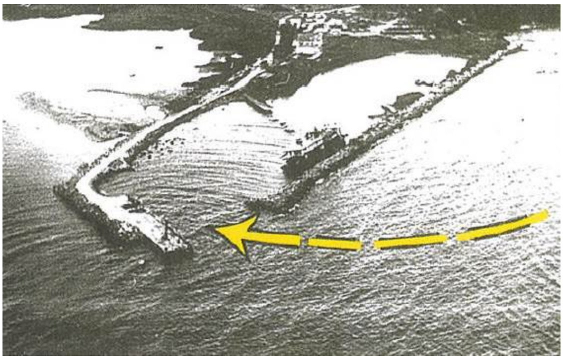

Fig. 2. A possible pathway of the inflow of sand from the north. The photo shows the configuration of breakwaters o the Port of Ruhnu in the 1990s [10]. Reproduced with a permission from the Tallinn University Publishers.

Fig. 3. A sandy beach is located to the west of the contemporary configuration of the Port of Ruhnu (base map: Estonian Land Board, 2020).

In this article, we address possible solutions to both described issues. The goal is to better understand their reasons and to employ this understanding to develop options for a new layout of the Port of Ruhnu. We start with a description of in situ wave measurements in the vicinity of the port entrance and validation of the SWAN wave model forced with different winds based on recorded time series of wave properties. Wave simulations using a phase-average model are employed to analyse suitable layouts for the port. We first analyse properties of waves in different scenarios to specify eventual new layouts of the port. This analysis is complemented by more detailed, phase-resolving examination of wave propagation in a prospective new layout using the 3-dimensional hydrodynamic model REEF3D. Finally, we evaluate the design wave parameters for this layout, by using extreme value analyses of wind properties and reconstructed water level time-series.

2. DATA, METHODS AND MODELS

2.1. Wave Measurements

Time series of wave properties were measured at and near the Port of Ruhnu in the period of 2021–2023 with pressure-based devices (Table 1) and directional waveriders (Table 2).

Table 1. Measurement Periods and Locations of Pressure Sensors

No	Name	N°	E°	Depth, m	Start date	End date	Data points	max H_s
1	PR_CTRL	57.7787	23.2753	4.6	01.05.2021	26.06.2021	5472	0.86
2					28.06.2021	22.08.2021	5376	1.47
3					24.08.2021	11.10.2021	4704	1.40
4	PR_ENTR	57.7796	23.2724	3.3	01.05.2021	26.06.2021	5472	1.13
5					28.06.2021	22.08.2021	5376	1.64
6					24.08.2021	12.10.2021	4700	1.49
7					13.10.2021	25.11.2021	4224	1.18
8					04.08.2022	08.09.2022	3456	0.41
9					26.09.2022	03.11.2022	3744	1.09
10	PR_PORT	57.7806	23.2701	1.6	01.05.2021	27.06.2021	5472	0.24
11					28.06.2021	23.08.2021	0	0
12					24.08.2021	27.08.2021	384	0.28
13					13.10.2021	26.11.2021	4320	0.27
14					04.08.2022	24.09.2022	4992	0.31

Table 2. Measurement Periods and Locations of Waverider Buoys

No	Name	N°	E°	Depth, m	Start date	End date	Data points	max H_s
1	LP_PORT	57.7782	23.2753	4.6	03.05.2021	17.11.2021	9516	1.64
2	LP_SEA	57.7695	23.3420	19	03.05.2021	17.11.2021	9516	2.45
3	LP_PORT	57.7785	23.2768	4.6	04.11.2022	30.04.2023	11622	2.02

The loggers manufactured by the Centre of Biorobotics of Tallinn University of Technology recorded continuously pressure fluctuations with a frequency of 5 Hz in three locations (Fig. 4) with water depths of 1–4 m. The length of each measurement session (1.5 months) was limited by the capacity of the batteries. The measurements were only performed in spring, summer and autumn 2021 and 2022 due to problems with winter maintenance of the instruments. The pressure data saved locally on the instrument was first converted into water level fluctuations and then into significant wave heights H_S, and 15-minute-interval periods were calculated with MatLab scripts from [12].

The directional waverider called LainePoiss® produced by WiseParker Ltd is a spherical buoy with a diameter of 32 cm, a height of 22 cm, and a weight of 3.5 kg. The output stream of LainePoiss® was validated through (i) sensor tests, (ii) wave tank experiments, (iii) a field validation against a Directional Waverider, (iv) an intercomparison of several buoys in the field, and (v) field measurements in the Baltic Sea marginal ice zone [13]. The bias of H_S was 1 cm, with a correlation coefficient of 0.99 and a scatter index of 8 % against the output of similar devices. The mean absolute deviation of mean wave direction was 70 °.

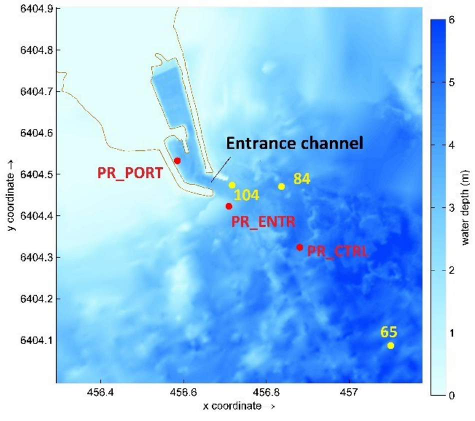

Fig. 4. Locations of pressure sensors in 2021 and 2022 (red) and calculation points (yellow) in [6]. Brown line indicates the waterline.

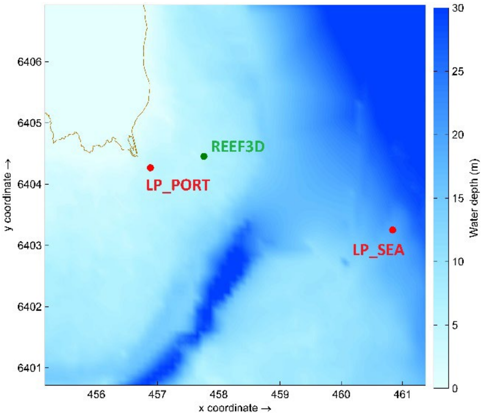

Fig. 5. Locations of waverider buoys in the period of 2021–2023 (red) and calculation point for REEF3D (green). Brown line indicates the waterline.

In 2021, two waveriders were deployed near the port entrance to validate the wave models and quantify the refraction-driven changes of wave propagation directions (Fig. 5) suggested by the numerical analysis [6]. In winter 2022/23, one waverider was set near the port entrance at point LP_PORT (Table 2).

The correlation coefficient between H_S recorded with the waverider and pressure sensor at LP_PORT and PR_CTRL (Fig. 4), respectively, was 0.91. The wave heights evaluated from pressure data were smaller (bias –0.19 m; root mean square deviation (D_{rms}) 0.22 m, maximum difference 0.82 m). The bias is apparently because of a relatively large water depth (4.6 m) in the location of the pressure sensor. The wave periods recorded by the waverider were 2–4 s. These periods are characteristic in this area [7], [14]. As pressure fluctuations generated by such short waves rapidly decay in the water column, the pressure sensor is not able to register some part of shorter waves. As a result, the average and instantaneous H_S may be underestimated even though the highest single waves may be recorded adequately.

The damping effect of the port structures was assessed by comparing the H_S recorded in- and outside of the port (Fig. 4). The H_S in the interior of the port was at least two times smaller than H_S outside the port during measurements performed in 2021. The difference (and thus the protection offered by the breakwaters) increased with the decrease of the wave height. In cases when $H_S > 0.5$ m outside the port, this ratio was about 4 and increased to >10 for very low wave conditions ($H_S < 0.2$ m outside the port). A slight change in the measurement location in 2022 led to slightly different values of this ratio. The core message from the measurements is that the significant wave height at the ferry berth in the port interior is less than 25 % from the wave height outside the port, whereas H_S in the entrance channel is about 50 % of the H_S outside the port.

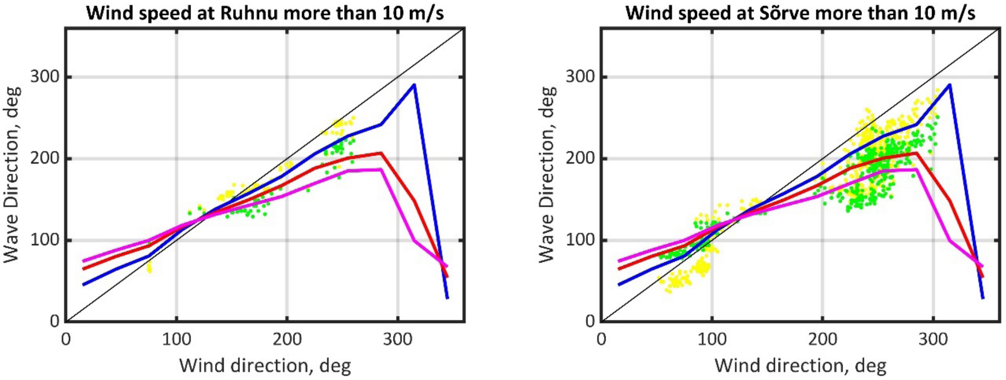

Fig. 6. Comparison of wind and wave directions hindcast using wind information from Ruhnu (left) and Sõrve (right). Note that the wind measurement location on Ruhnu may be shadowed by the forests on the island. Blue, red and magenta lines show the modelled directions of waves for points 65 (Fig. 4), 84 (fairway) and 104 (entrance channel) with constant wind speed of 10 m/s (evaluated as in [6]). Yellow and green dots indicate the recordings at LP_SEA and LP_PORT (Fig. 4), respectively.

The modelling exercise in [6] demonstrates that refraction of waves is the strongest and redirects the waves directly into the port entrance when the wind speed is 15 m/s. Such wind speeds did not occur during the measurement campaigns. For this reason, we compare wave directions for all wind speeds ≥10 m/s at Ruhnu and Sõrve (Fig. 1). Figure 6 confirms that refraction clearly redirects waves in the vicinity of the port entrance even though the rate of change in the wave direction is in some occasions smaller than evaluated in [6].

2.2. Wave Models and Wind Data

The waves were modelled using the SWAN (version 40.11) wave model [15] in Delft3D suite (WAVE module). SWAN is a third-generation phase-averaged spectral wave model developed at Delft University of Technology. A more detailed description of the particular implementation of this model for the study area is provided in [6] and [16]. We used a four-level nested scheme of regular rectangular model grids. Even though only very limited amount of wave energy created in the Baltic proper enters the Gulf of Riga, propagation of specific swells into the gulf and their refraction along underwater sandy features near Cape Kolka towards Ruhnu cannot be excluded. For this reason, a coarse model was run for the whole Baltic Sea on a grid with a step of 5000 m (251 × 271 grid points). The second level grid covered the Gulf of Riga with a step of 1000 m (171 × 181 grid points). The third level grid (Fig. 3) covered the neighbourhood of Ruhnu with a step of 100 m (211 × 171 grid points). The innermost (finest) model focused on the Port of Ruhnu (Fig. 3) with a resolution of 3 m (300 × 300 grid points). The resolution of the third- and fourth-level grids is evidently fine enough to replicate detailed properties of waves in the vicinity of Ruhnu and Port of Ruhnu. The bathymetry was taken from the databases of Estonian Transport Administration, Baltic Sea Bathymetry Database by the Baltic Sea Hydrographic Commission [17] (http://data.bshc.pro/legal/) and Saarte Liinid LLC.

We compared the output of the SWAN model with estimates produced by a semi-empirical fetch-based wave model, called SPM-method [18] and denoted as SPM. The idea was to see how a very simple model compares with a sophisticated contemporary numerical model. We followed the procedure given in [19]. For each measurement site we measured the fetch with a 20 ° step. Wave models were forced with wind speed and direction from nearby meteorological stations. We calculated wave parameters (H_S and peak period T_p) with 1 h time step.

The SWAN and SPM models were forced with wind information from several sources. The aim was to select the most suitable source of wind in terms of the match of modelled and recorded data. We used measured wind data from Ruhnu, Kihnu, Sõrve and Vilsandi (Fig. 1) and modelled ERA5 winds [20], [21]. The ERA5 dataset is the fifth-generation global atmospheric reanalysis produced by the European Centre for Medium-Range Weather Forecasts (ECMWF) [22] from 1940 to present. We use the ERA5 data from 2021 and 2022 since the data from 2023 has not been available yet. This wind data realistically represents spatio-temporal variations in the wind properties with a time step of 1 h and spatial resolution 0.25 ° (about 30 km). The recorded wind properties are used to construct one-point homogeneous unidirectional non-stationary wind fields with a temporal resolution of 1 h. Such conditions (referred to as SWANhom) are used for modelling waves in extreme conditions with long return periods. ERA5 wind data was not used in SPM models.

Ruhnu, Kihnu, Sõrve and Vilsandi meteorological stations (Fig. 1) are operated by the Estonian Environment Agency. Automatic systems were installed in all stations in 2003. The Ruhnu station, active since 1958, is located on the southern part of the island, about 200 m from sea. It is open to all directions, except to the north and north-east (NE) where the forest grows. Its data set is not homogeneous. Initially measurements were carried out four times a day, then eight times. No measurements were performed in the period of 1987–1996, and thereafter only two recordings a day were taken. The Kihnu station is sheltered by the forest in the north and east. It has been operating since 1931. Digitised records are available since 1958 when the wind speed and direction were measured four times a day. The Sõrve station is located at the tip of the Sõrve peninsula and is open to all directions. It is somewhat influenced by the peninsula to the north of the station. The measurements commenced in 1866. The digitised records are available from 1961.

Vilsandi meteorological station is located on a small island, to the west of the island of Saaremaa (Fig. 1). The data from Vilsandi is often used as a standard, high-quality representation of wind properties in the northern Baltic proper. The wind data at Vilsandi is highly reliable except for easterly winds [23] that are generally less frequent and weaker than SW or NNW winds in this region. The station has been operating since 1865. The digitised records are available since 1947 when the wind speed and direction were measured four times a day. Starting from 1966, the measurements were performed eight times a day.

2.3. Validating the Wave Model

The comparison of the modelled wave heights and periods with recorded data covers the whole time period of measurements (Table 3) and includes a detailed assessment of wave conditions during the most severe recorded events (Tables 4 and 5; Figs. 7 and 8).

Table 3. Comparison of Modelled H_s with the Recorded ones during 3 May 2021 –17 November 2021 (The positive bias means that the modelled H_s are higher than the recorded H_s. D_{max} (m), D_{rms} (m), and R denote the maximum difference, root mean square difference and correlation coefficient, respectively, between measured and modelled values.)

No	Wind	Type of model	PR_ENTR H_s, m				LP_PORT H_s, m				LP_SEA H_s, m			
			bias	D_{max}	D_{rms}	R	bias	D_{max}	D_{rms}	R	bias	D_{max}	D_{rms}	R
1	ERA5	SWAN	0.18	0.83	0.23	0.89	0.06	0.69	0.14	0.92	0.02	0.80	0.15	0.93
2	Ruhnu	SWANhom	0.03	1.02	0.16	0.80	-0.20	0.76	0.25	0.86	-0.38	2.15	0.47	0.76
3	Vilsandi	SWANhom	0.02	1.10	0.24	0.50	-0.12	1.30	0.28	0.55	-0.23	1.67	0.44	0.55
4	Ruhnu	SPM	-0.08	1.17	0.21	0.66	-0.25	1.23	0.32	0.71	-0.45	2.22	0.57	0.62
5	Vilsandi	SPM	-0.03	1.09	0.24	0.42	-0.19	1.43	0.33	0.46	-0.37	2.22	0.54	0.47

Table 4. Comparison of Modelled H_s with the Recorded ones during 19 October 2021–24 October 2021 (The positive bias means that the modelled H_s are higher than the recorded H_s. D_{max} (m), D_{rms} (m), and R denote the maximum difference, root mean square difference and correlation coefficient, respectively, between measured and modelled values.)

No	Wind	Type of model	PR_ENTR H_s, m				LP_PORT H_s, m				LP_SEA H_s, m			
			bias	D_{max}	D_{rms}	R	bias	D_{max}	D_{rms}	R	bias	D_{max}	D_{rms}	R
1	ERA5	SWAN	0.31	0.83	0.36	0.84	0.19	0.44	0.24	0.93	0.11	0.59	0.23	0.88
2	Ruhnu	SWANhom	0.06	0.60	0.25	0.71	-0.19	0.49	0.28	0.86	-0.51	1.32	0.61	0.71
3	Vilsandi	SWANhom	0.24	1.10	0.36	0.52	0.05	0.63	0.27	0.65	-0.08	1.21	0.41	0.62
4	Ruhnu	SPM	-0.09	0.84	0.25	0.57	-0.35	0.95	0.40	0.76	-0.70	1.81	0.78	0.69
5	Vilsandi	SPM	0.01	0.86	0.25	0.50	-0.22	1.00	0.36	0.53	-0.57	1.75	0.71	0.40

Table 5. Comparison of H_s with the Measurements during 17 August 2021–21 August 2021 (The bias indicates that the modelled H_s are higher than the measured H_s. D_{max} (m), D_{rms} (m), and R denote the maximum difference, root mean square difference and correlation coefficient, respectively, between measured and modelled values.)

No	Wind	Type of model	LP_PORT H_s, m				LP_SEA H_s, m			
			bias	D_{max}	D_{rms}	R	bias	D_{max}	D_{rms}	R
1	ERA5	SWAN	0.07	0.40	0.15	0.96	0.05	0.46	0.18	0.95
2	Ruhnu	SWANhom	-0.26	0.76	0.29	0.94	-0.44	1.18	0.49	0.90
3	Vilsandi	SWANhom	-0.23	1.12	0.39	0.60	-0.36	1.62	0.57	0.55
4	Ruhnu	SPM	-0.47	1.20	0.52	0.79	-0.69	1.74	0.77	0.71
5	Vilsandi	SPM	-0.41	1.43	0.56	0.34	-0.65	2.00	0.81	0.31

As expected, recorded wave properties have the best match in terms of the correlation with those modelled using spatially varying ERA5 wind information. However, the bias between the modelled and recorded data was larger for this data set than in other models during the whole modelled period in 2021 and in October 2021. The SWAN model forced with ERA5 winds overestimates wave heights during relatively severe seas (Fig. 7). The use of one-point homogenous wind based on Vilsandi data overestimates wave heights in October, but underestimates in August 2021.

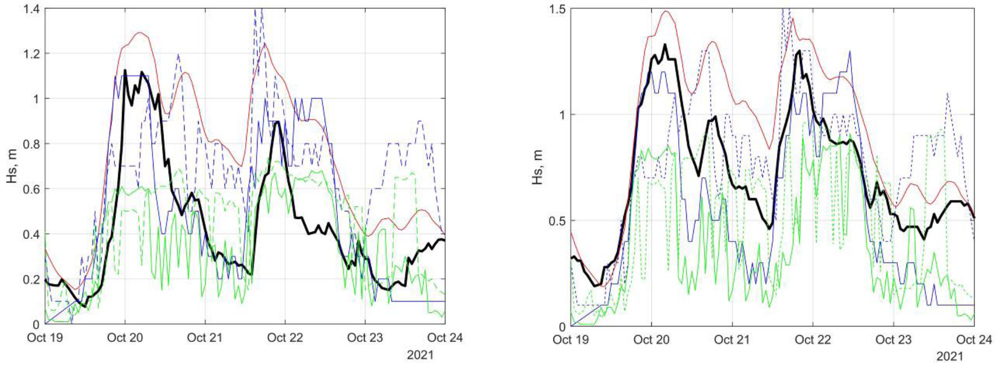

Fig. 7. Recorded H_s in October 2021 (black line) in point PR_ENTR (on the left, Fig. 4) and point PR_PORT (on the right). Red line indicates the modelled H_s with ERA5, blue H_s modelled with homogenous wind from Ruhnu (continuous) and Vilsandi (dashed), and green H_s modelled with SPM with wind from Ruhnu (continuous) and Vilsandi (dashed).

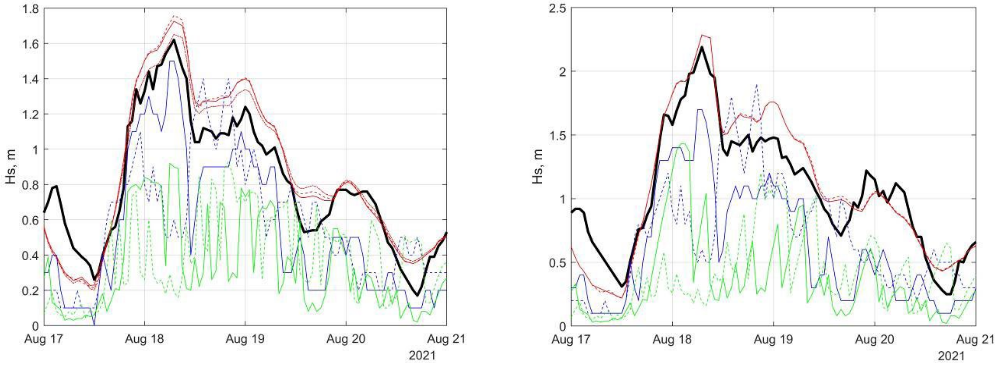

Fig. 8. Recorded H_s in August 2021 (black line) in point PR_ENTR (on the left, Fig. 4) and point LP_PORT (on the right). The colour and line type code is the same as for Fig. 7.

Somewhat surprisingly, the best match of the recorded and modelled wave properties at the entrance of the port (point PR_ENTR, Fig. 4) provides the combination of the SWAN model and one-point homogenous wind forcing based on wind recordings from Ruhnu. The relevant bias and D_{rms} are smaller than similar values for other simulation exercises (except for August 2021). We also checked the wave directions by comparing refraction described in [6] with measured directions. The modelled results had a good correspondence with the measured results. As no strong winds occurred during the measurement campaign, it was not possible to detect strong refraction-driven effects. Based on this analysis, we use SWAN wave model with homogenous wind forcing from Ruhnu to evaluate design wave parameters for the port structures.

2.4. Water Level

Water level was observed visually at Ruhnu two to four times a day in the period of 1945–1988. Measurements resumed after a long pause with an automatic device in 2012. As water level information is crucial for structural design, we fill the water level data for missing years using recordings at the coastal stations in Estonia and Latvia. These data are converted into the European Vertical Reference System, EVRS.

Table 6. Comparison of Reconstructed Water Levels Based on Two Different Stations (WL1 and WL2) with Measured Values at Ruhnu in the Period of 2012–2020 (D_{max} (cm), D_{rms} (cm), and R denote the maximum difference, root mean square difference and correlation coefficient, respectively, between measured values at Ruhnu and constructed values.)

No	WL1	WL2	Weight of WL1	Weight of WL2	D_{max}, cm	D_{rms}, cm	Bias, cm	R
1	Roja	Salacgriva	0.5	0.5	26.8	5.5	0.7	0.91
2	Roja	Salacgriva	0.6	0.4	27.3	5.7	1.4	0.91
3	Roja	Salacgriva	0.7	0.3	28.5	6.0	2.1	0.90
4	Liepaja	Daugavgriva	0.5	0.5	45.8	12.1	7.7	0.69
5	Liepaja	Daugavgriva	0.4	0.6	39.1	10.4	5.8	0.74
6	Liepaja	Skulte	0.5	0.5	41.3	12.3	9.2	0.77
7	Liepaja	Skulte	0.4	0.6	31.7	10.4	7.5	0.83
8	Liepaja	Skulte	0.6	0.4	50.8	14.4	10.8	0.69
9	Liepaja	Skulte	0.3	0.6	34.3	15.3	13.9	0.85
10	Liepaja	Skulte	0.5	0.7	43.2	10.9	-6.8	0.82
11	Liepaja	Skulte	0.5	0.6	32.6	8.3	1.2	0.80

The most complete datasets in terms of hourly measurements among Latvian water level recordings are at Liepaja and Daugavgriva [24]. To a first approximation, we assume that the water level changes linearly between any two stations. It is likely that this approximation is adequate for stations that are located along relatively straight coastline segments. This is the case for Latvian water level measurement locations on the Baltic proper shore and in the Gulf of Riga [24]. To validate this assumption, we compared the outcome of this simple model with the measurements at Ruhnu in the period of 2012–2020 (Table 6). The strongest correlation, lowest bias and smallest D_{rms} are reached if this model is fed with recorded water level values from Roja and Salacgriva with equal weights. The resulting estimates of water level at Ruhnu are thus used below for calculating return periods for extreme water levels near the port structures.

3. MODELLING THE HARBOUR LAYOUT

3.1. Choosing the Layout Based on Wave Modelling

The properties of wave climate form just one criterion for the (re)design of the harbour layout. One must also consider the current fairway for the ships that may potentially make a port call, variation of water depths in the sea, and access roads and structures in the port. Several these constraints cannot be adjusted within a reasonable budget, efforts and time even for small ports, such as Ruhnu.

Most likely it is not possible to radically change the location of the entrance to the Port of Ruhnu as this is the only relatively deep-water location around the island that is maintained by the existing hydrodynamic loads. The idea of possible new openings in the eastern or western quays and breakwaters seems unrealistic because of likely very large costs of repeated dredging even if a re-design of structures is not considered. To a first approximation, the feasible solution would be to improve protection of the entrance channel, by relocating and/or extending the breakwaters.

We start this analysis from rough estimates of extreme wave conditions near the port entrance under strongest winds from different directions with different return periods. The goal is to select the configuration of breakwaters that provides, on average, the best protection of the port interior in theoretically possible worst conditions.

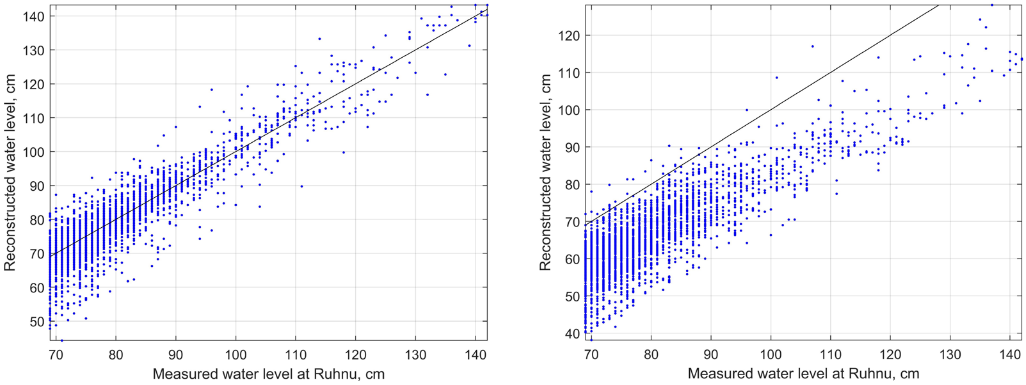

Fig. 9. Comparison of reconstructed water levels from Roja and Salacgriva (left panel, line 1 in Table 6) and Liepaja and Skulte (right panel, line 9 in Table 6) with measurements at Ruhnu in the period of 2012–2020.

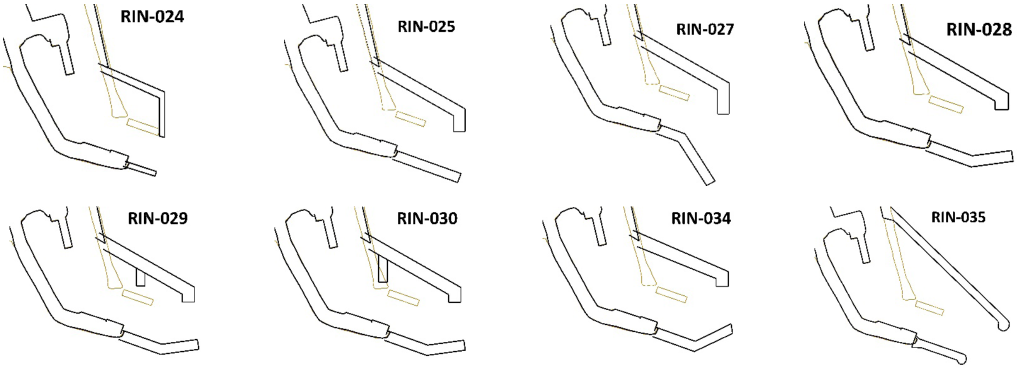

Fig. 10. Modelled new layouts (black thick line). Thin brown line indicates the current layout.

The SWAN wave model in Delft3D suite (see above) was forced with homogenous unidirectional stationary winds over the entire Baltic Sea from 12 directions with a step of 30°. For every direction, extreme wind speeds with return periods of 2, 5, 10, 20, 50 and 100 yr were applied. These wind speeds were calculated from time series of wind properties recorded on Ruhnu by applying peak-over-threshold method [25], [26].

Wind speeds corresponding to different percentiles of strong winds were used to mimic more frequently occurring severe wave conditions. For every return period, the runs were performed for a selection of elevated water levels with a step of 30 cm. Doing so may lead to certain overestimation of the impact of extreme wave conditions because for some directions high water levels and severe wave conditions do not necessarily occur simultaneously [27]. For example, strong easterly winds are not associated with substantially elevated water levels at Ruhnu. Doing so still gives some indication of properties of possible worst-case scenarios.

This approach was applied to eight potential new layouts built around the existing interior of the port and the fairway out of the port (Fig. 10). The spatial distributions of differences of were assessed visually and based on virtual wave recorders in key locations in the port (Fig. 11).

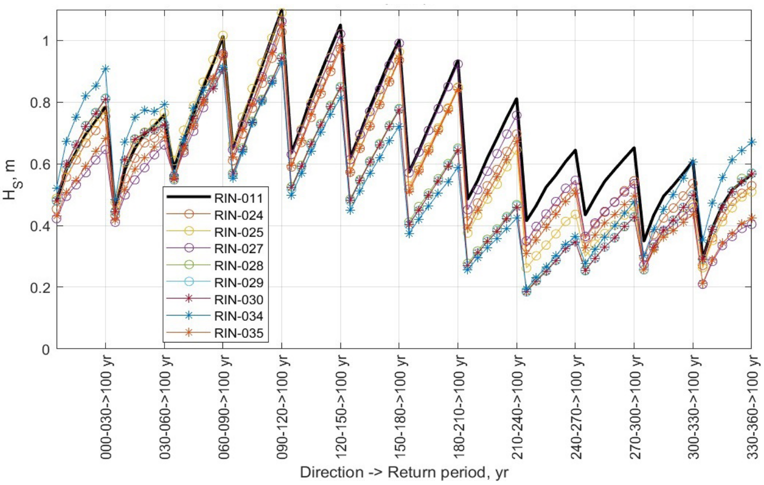

Fig. 11. Modelled H_s in the port interior (point 5 in Fig. 17) for breakwater layouts shown in the legend of Fig. 10. The layout RIN-011 reflects the current situation. The markers show values for extreme wind speeds with return periods of 2, 5, 10, 20, 50 and 100 years with a directional resolution of 30 °.

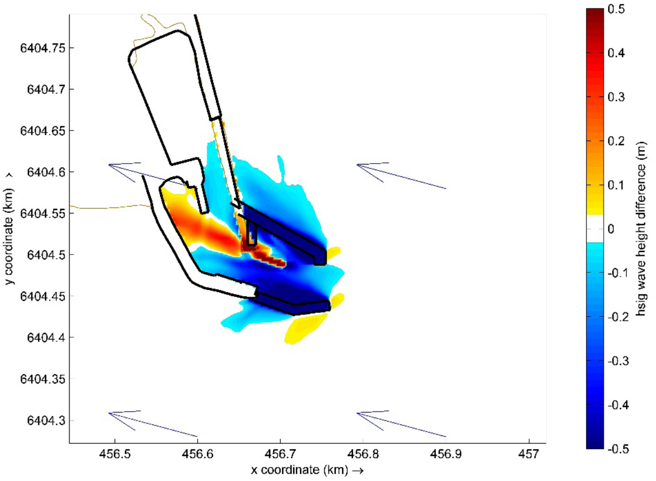

Fig. 12. Differences of H_s in an east-south-eastern storm that occur in the port area with layout RIN-030 compared with H_s that occur in the current (RIN-011) layout. Negative values mean that the wave heights are lower in RIN-030 layout. Blue arrows show the wind direction.

Consultations with the harbour owner (personal communication, January 2023) led to a conclusion that the best layout was RIN-030 (Fig. 12). It (i) reduces wave heights in the entrance channel and (ii) makes the entrance channel wider which is important for ship manoeuvrability. Also, (iii) small inner breakwater reduces the waves compared with other solutions and (iv) this layout is a cost-effective solution. A drawback of this solution is that wave heights will be larger at the present berthing area in strong storms. This feature was not deemed a big problem by the owner. From the owners' viewpoint, the most problematic issue was moving a ship into the harbour through the narrow entrance. Wave reflection coefficients for obstacles are given in Section 3.2. We take this layout (called new (breakwater) layout for simplicity) as the basis of further analysis.

3.2. Phase-Resolving Modelling

Significant diffraction of wave energy often takes place around breakwaters, creating extremely complicated wave regime inside the port. This (often nonlinear) diffraction is challenging for phase-averaging models but can be captured by more local phase-resolving models. For this reason, the phase-resolving fully nonlinear potential flow model REEF3D::FNPF [28], [29] within the open-source hydrodynamics code REEF3D [30] was used to investigate the wave propagation inside the port for both the old and new breakwater layouts with various offshore wave directionalities.

The REEF3D::FNPF code solves the Laplace equation and nonlinear boundary conditions for the velocity potential and free surface elevation using the parallelized geometric multigrid preconditioned conjugate gradient solver provided by the *hypre* library [31]. High-order discretisation methods were used to further ensure the accuracy and stability of nonlinear and steep waves. For example, 5th-order WENO spatial discretisation [32] and 3rd-order Runge-Kutta temporal schemes [33] were used for the simulations. The code utilised a message-passing interface (MPI) for parallel high-performance computations, allowing multiple-processor large-scale simulations. A novel coastline algorithm and robust breaking wave algorithm were introduced to the code to resolve most of strongly nonlinear coastal wave transformations [28]. A relaxation method [34] was used for wave generation and numerical beaches in the presented study.

The numerical domain focuses on the Port of Ruhnu and its offshore area to the SE, with east-west/north-south dimensions of 1250 m and 1000 m, respectively. The objective was to investigate what happens in both the old and new breakwater layouts and the effectiveness of the improvements. For each layout, three offshore wave directions were investigated, approaching from the east (90^o), SE (135^o) and NE (45^o) waves. These waves propagate in directions roughly aligning with the port entrance and fairway and were thus specifically chosen as potential extreme scenarios associated with intense wave refraction in strong storms from other directions [6]. The new harbour layout is better represented in the numerical wave tank than the old layout thanks to the improved data fidelity especially around the new breakwaters and the western beach coastlines. However, the most relevant structures are sufficiently resolved to investigate the influence of the wave propagation and transformation in both scenarios.

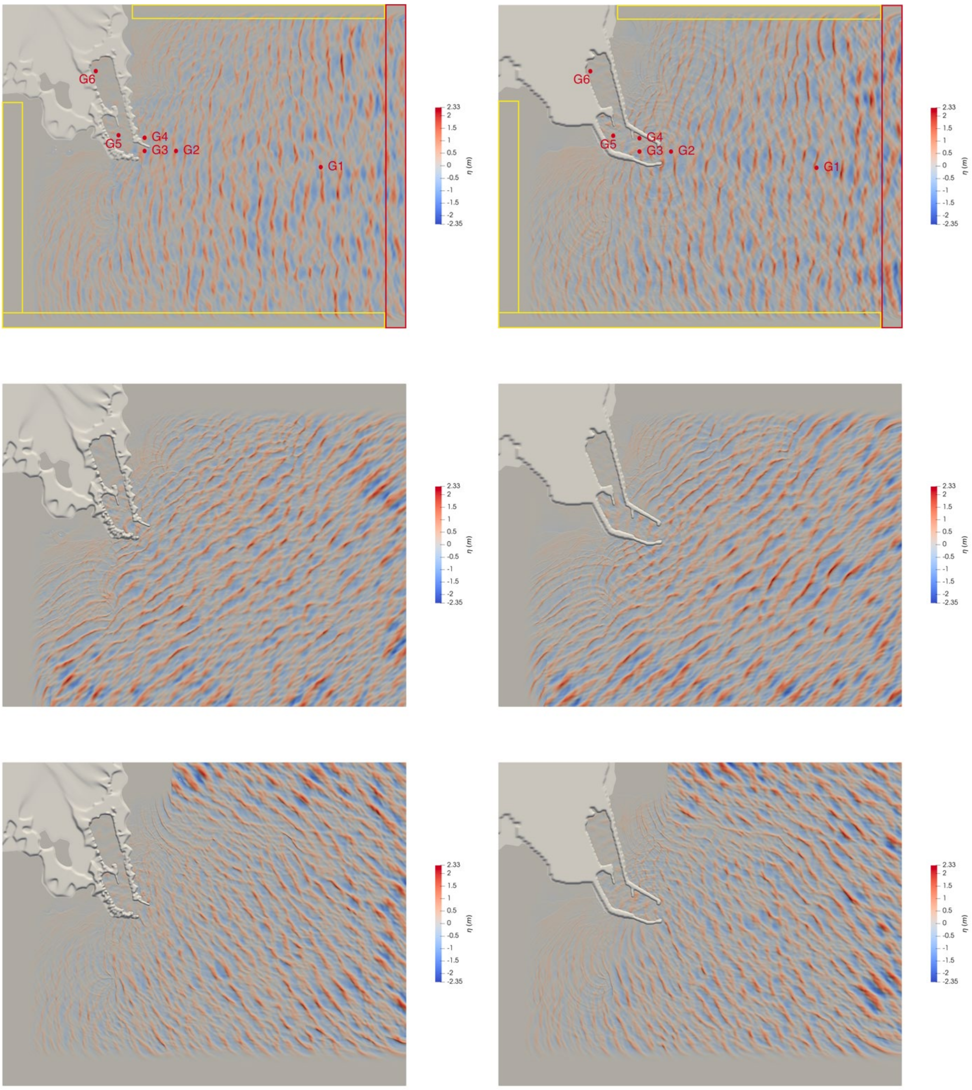

Fig. 13. Simulated wave surface elevation at the last simulation time step for both the old (left) and new (right) breakwater layouts with three offshore wave principal directions – East (top), SE (middle) and NE (bottom). The numerical wave gauges (nodes) are indicated as red circles in the uppermost panels. The red boxes are wave generation zones, and the yellow boxes are numerical beaches for the eastern wave case. The wave generation zones are allocated at the income wave boundaries with numerical non-reflecting beaches allocated on the opposite boundaries for the SE and NE waves.

Six numerical wave gauges (called (wave) nodes below) were arranged from the offshore area to the inner harbour (Fig. 13). The maximum H_s and the corresponding T_p were chosen based on the offshore SWAN simulation at node (Fig. 4) which was located at the eastern boundary of the phase-resolving computational domain, resulting in the input irregular wave with H_s = 2.2 m and T_p = 6.3 s. A cell size of 2 m was used after a 2D grid convergence study, which ensured over 30 cells per wavelength corresponding to the peak period. The DNV(Det Norske Veritas)-recommended JONSWAP spectrum and a Mitsuyasu directional spreading function (e.g., [35]) with a shape factor 28 were used as input for the narrowly spreading short-crested multi-directional irregular wind-wave simulations. While 3.5 hours of simulations were performed for each scenario, the last 3-h time series was used for processing statistical properties of the wave field. With 128 cores on the local computing station, each simulation took about 4 to 5 hours to complete. The numerical wave tank (NWT) configurations and the simulated free surface elevations for all scenarios are presented in Fig. 13.

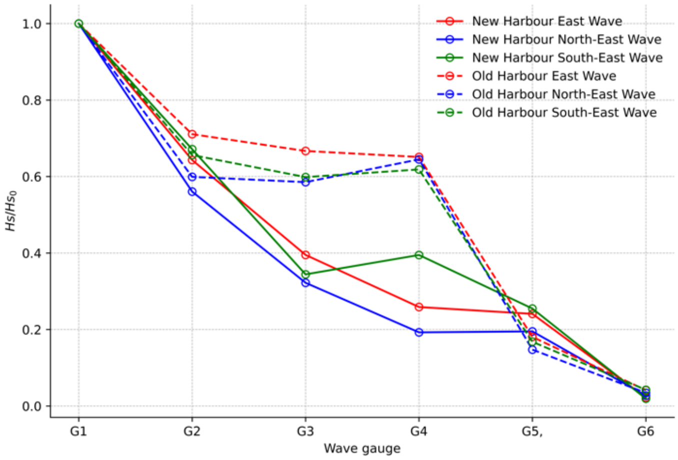

Fig. 14. Variations of from offshore to the inner harbour.

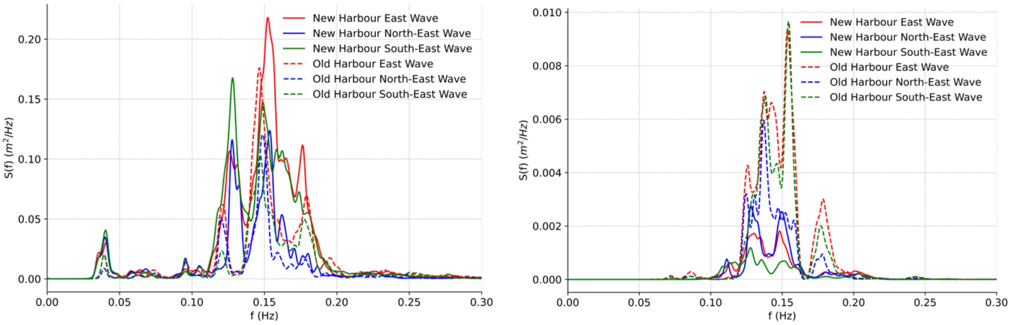

Fig. 15. Wave spectra at numerical wave gauges (nodes) 5 (left) and 6 (right) for the old and new breakwater layouts with various offshore wave directionality.

The H_s correlation factors to the input waves at the wave nodes for all scenarios are shown in Fig. 14. The extended harbour layout provides extended sheltered areas, as can be seen from the much-reduced waves at nodes 3 and 4. This is beneficial for the ferry navigations along the narrow entrance. The highest waves along the fairway are observed for southeast waves, as the H_s at node 4 indicates, which is expected since the wave direction aligns with the harbour opening. The wave height reduction for the inner harbour area is less obvious when comparing H_s. To further illustrate the effect of the extended harbour, the wave spectra at nodes 5 and 6 at the inner harbour were compared in Fig. 15. Though the new layout reduces the H_s along the navigation channel significantly, the wave heights and spectra at node 5 near the berth are quite comparable to the old layout. This feature is to some extent alarming; however, the significant wave height is about 0.2 m that is on most occasions not dangerous.

The wave spectra show a four-peak pattern for both layouts, which could be a result of the reflections from the compactly configured breakwaters. Such reflections might create resonance, standing wave patterns and infra-gravity waves which may be indicated by the increased low frequency peak around 0.04 Hz (25 s). Only about half the energy is able to propagate towards the inner harbour at node 6 with the new layout in comparison with the old configuration. A four-peak spectrum pattern was also observed with the old harbour layout, especially a high-frequency peak near 0.175 Hz (about 5.7 s) containing a significant amount of wave energy. The new extended layout constrains the wave energy in a predominantly two-peak spectrum near the peak frequency. This bi-modal wave behaviour makes it simpler to avoid modal resonance when designing coastal structures.

3.3. Evaluation of Design Parameters for the Breakwaters

The design parameters of hydrodynamic loads to coastal engineering structures are commonly evaluated based on critical combinations of wave loads and water levels. The properties of these combinations may substantially vary depending on the wind direction in strong storms in the study area [27]. To comply with this feature, the reconstructed water level time series at Ruhnu (Section 2.4) was binned to different sectors according to the instantaneous wind directions at Ruhnu with 30 ° step. The resulting subsets were employed to evaluate very high-water levels with different return periods that are associated with different wind directions. As single projections of extreme water levels may have substantial uncertainties in the Baltic Sea basin [36], we use several versions of extreme value distributions to construct an ensemble of projections. These distributions are theoretical limiting distributions for maxima or minima (extreme values) of statistically independent and identically distributed samples [25].

We use the so-called block maximum method (e.g., [25]). To remove correlations between single maxima, one should consider only values that are sufficiently separated in time. Monthly maxima and minima are often serially correlated in the Baltic Sea because of inertia of the formation of Baltic Sea water levels [37], [38]. Therefore, longer blocks are necessary for an application of this method. Even annual values could be correlated to each other. For example, the highest values of two subsequent years could occur during a windy period that involves December and January. Eelsalu et al. [36] compared extreme water level projections based on annual and so-called stormy season maxima (from July to June next year, [24]). The extreme water levels projected using the maxima over stormy seasons were usually higher than those based on the annual maxima. Following a conservative view, we rely on maxima of stormy seasons.

A large variety of empirical distributions of recorded water level data and the presence of outliers in the neighbourhood of the study area [9] suggest that none of the classic extreme value distributions perfectly estimates extreme water levels for longer return periods. It is reasonable to assume that the errors of projections made using single distributions are randomly distributed [36]. This assumption justifies the concurrent use of several distributions to form an ensemble. Thus, we include results obtained using a general Generalized Extreme Value (GEV) distribution and its limiting case, a Gumbel distribution, into such an ensemble (Fig. 16). To provide an estimate of the lower limit of extreme water levels, we also included the 2-parameter Weibull distribution into the ensemble. It is likely that the average of such an ensemble provides a sensible estimate of the true value of extreme water levels that is necessary for coastal design and management. The spreading of projections adds information about their possible bias and variability of these projections that are also needed in the assessment of engineering applications. We used a freely available general-purpose software tool *Hydrognomon* [39] for specification of parameters of these distributions.

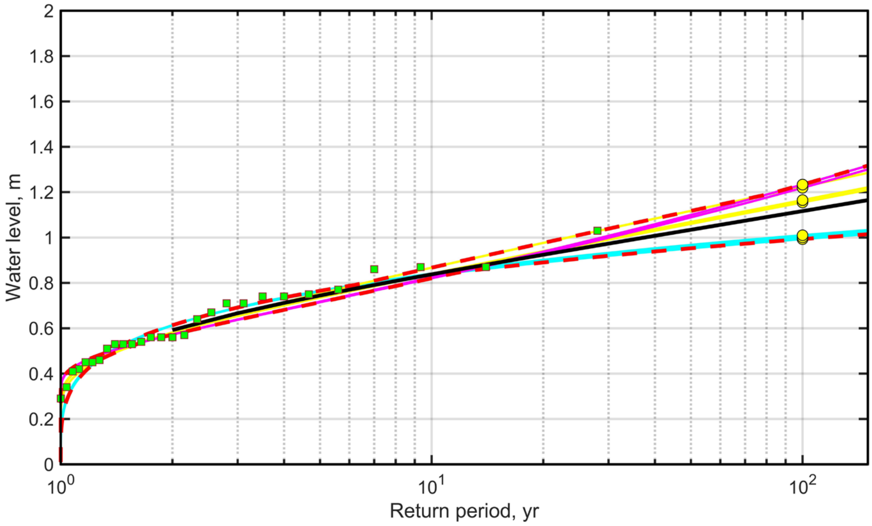

Fig. 16. Return periods of extreme water levels associated with wind directions 120–150 ° according to different projections at Ruhnu. Green rectangles show stormy season maxima and yellow circles depict water levels with return period of 100 yr for different projections. Yellow lines: projections using the Gumbel distribution; magenta – GEV distribution; cyan – 2-parameter Weibull distribution; black – weighted average of projections.

The developed ensemble for Ruhnu (Fig. 16) signals that the projections of extreme water levels form a narrow (width less than 0.2 m) corridor for return periods up to 30 yr. This time scale characterises half of the length of the underlying time series. For even longer return times the projections spread considerably. This spreading reaches about 0.3 m for a 100 yr return period, i.e., for the time interval that is almost twice as long as the time series.

The wind climate in the study area has greatly varying probability of strong wind speeds from different directions [8]. We address this feature by addressing separately extreme wind speeds and their return periods for winds from different 30 ° wide sectors. To avoid serial correlation of maxima, we only included winds ≥10 m/s into the set of block maxima, thus concentrating on the events that dominate the extremes. It is likely that such samples are identically distributed. Extreme wind speeds from single sectors and their return periods are evaluated using a Gumbel distribution that is well suited to evaluate wind speed maxima [25].

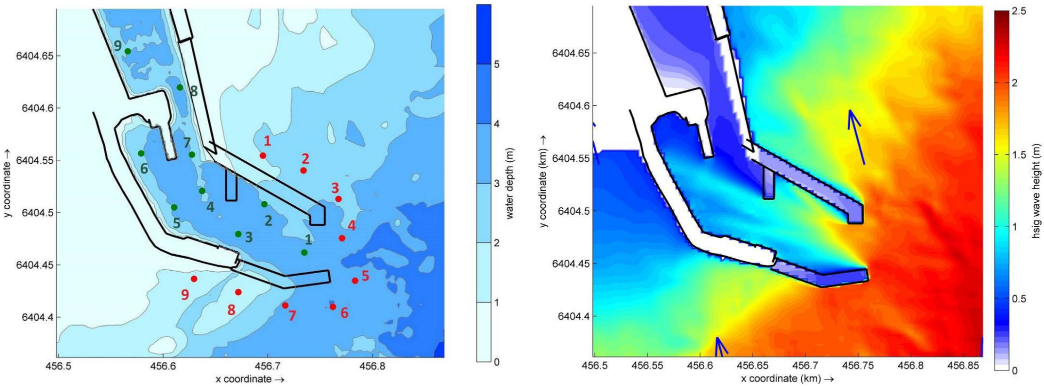

Fig. 17. Virtual wave gauges (nodes) of the Delft3D (SWAN) runs forced with stationary extreme wind conditions used for the final design of breakwaters (left panel). Black lines indicate the water line of the new layout. An example of the distribution of corresponding to extreme wind properties from south-south-east with 50-yr return period (right panel; wind direction is shown with blue arrows).

The projections of extreme water levels with different return periods were applied to describe increased water depths in the above-described four-level nested wave model SWAN (Section 2.2). This model was forced with homogenous unidirectional stationary winds from single sectors. Wave conditions were evaluated using extreme wind speeds with return periods of 2, 10, 50 and 100 yr until saturation of the wave field. The parameters (H_s, T_p, T_m, directions, etc.) of the resulting saturated wave conditions were analysed in several locations (virtual wave gauges or nodes) around the breakwaters and in the port interior. Following the recommendations from [40], the points were selected at a distance about 5 times H_s away from the toe of breakwaters (Fig. 17). These combinations of water level and wave properties were used to specify the design parameters of hydrodynamic loads to the elements of the proposed new layout of breakwaters. The resulting wave parameters were used to design the cross-sections of breakwaters. Wave parameters for navigation season (from April till October and possibly November) were calculated in a similar fashion. A map of significant wave heights in the vicinity of the port and in the harbour interior during the worst of analysed wave conditions attacking the harbour (Fig. 17) signals that the new layout provides sufficient protection for the inner harbour.

4. DISCUSSION AND CONCLUSIONS

The performed wave measurement campaigns, first of all, demonstrate that a kind of ultra-refraction that translates storm waves from virtually any direction into a wave system that propagates directly into the entrance of the Port of Ruhnu [6] is a highly interesting and instructive feature of the local environment and not just a spurious result of a wave modelling exercise. Still, a few multi-week measurement campaigns over past 3 years are not yet enough to exactly quantify all transformations of waves caused by strong (higher than about 15 m/s) winds. An appropriate quantification of these transformations requires much longer measurement campaigns.

However, the wave measurements provided vital data for validation of the wave models. As expected, the best match with the wave recordings obtained using several pressure sensors and two directional waveriders provided the 3rd generation wave model SWAN which was forced with the modelled ERA5 winds. Notably, this model systematically overestimated wave heights in the measurement locations.

Interestingly, wave properties modelled using homogenous one-point wind recorded in the local meteorological station on Ruhnu had comparable and in several occasions even better match with the recorded wave properties. This feature is similar to the outcome presented in [41] and encouraged the use of this kind of computationally much less expensive modelling exercises to analyse different layouts of the port and to calculate design parameters.

The correct specification of design parameters could not be done without proper water level data. The local water level recordings had long gaps. To address this shortage, it was necessary to reconstruct a “synthetic” time series of water levels by using the data from other water level stations in the Gulf of Riga and even on the Baltic proper shore of Latvia. This exercise showed that the best results were yielded by a linear combination of recordings from Roja and Salacgriva that are located at almost opposite sides of the Gulf of Riga.

The adequate design of harbour breakwaters has to take into account not only waves, water level and sediment movements, but also suitable fairway, bathymetry, access roads and other limiting structures in the harbour. These aspects set major restrictions for the improvement of the geometry and layout of breakwaters. Thus, the analysed layouts were focused on improving and extension of the current layout. To evaluate advantages and disadvantages of 11 different layouts (out of which eight were presented above), wave and water level parameters for different return periods were modelled with the SWAN wave model, and resulting wave heights in key points in the interior of the port were compared. Although the phase-averaged SWAN wave model is not designed to be used in small basins, the comparison of its results with the output of phase-resolving REEF3D showed that it gave reasonable results and could be used in similar studies.

It is likely that, for any reasonably extension of breakwaters, the intrusion of sand into the port entrance will continue. It is likely that this issue could be mitigated using appropriately placed submerged breakwaters [42] that slow down sand motion similarly to the impact of tombolos [43]. The situation would still need regular monitoring of sediment transport and accumulation.

Perhaps the most instructive lesson from the variety of measurement, design and modelling exercises is that a combination of greatly different methods and approaches is needed to gather progress in solving a seemingly simple problem of re-design of breakwaters in such a complicated environment. Another lesson is that surprisingly simple models provide very good information in environments that possess extensive small-scale variability in geometry and bathymetry. However, they are not able to highlight particularly intricate features, such as the formation of a bi-modal wave system in the port interior. This information can be used for fine-tuning the breakwater configuration to provide better protection in the port interior by suppressing one mode instead of addressing the entire wave spectrum.

ACKNOWLEDGEMENTS

The research was co-supported by the Estonian Research Council (grant PRG1129) and the European Economic Area (EEA) Financial Mechanism 2014–2021 Baltic Research Programme (grant EMP480). Rain Männikus acknowledges the support by Saarte Liinid AS (LLC), contract LTEE21048. The entire study was initiated by the local port authority, Saarte Liinid AS to address the problem of mitigation of inconvenient waves at the port entrance and accumulation of sand in the port interior by concerted field work and modelling exercises.

REFERENCES

1. Kirby, R. (2011). Minimising Harbour Siltation-findings of PIANC Working Group 43. *Ocean Dynamics*, *61* (2–3), 233–244. https://doi.org/10.1007/s10236-010-0336-9
2. Lojek, O., Goseberg, N., & Schlurmann, T. (2021). Projecting Hydro-Morphodynamic Impacts of Planned Layout Changes for a Coastal Harbor. *Journal of Waterway, Port, Coastal and Ocean Engineering*, *147* (6), 05021013. https://doi.org/10.1061/(ASCE)WW.1943-5460.0000666
3. Kuang, C. P., Li, H. Y., Huang, G. W., Han, X. J., Zou, Q. P., & Song, H. L**.** (2022). Sediment Transport and Morphological Responses of a Silty Coast to a Cold Front Event in the Southwest Bohai Bay of China. *Estuarine, Coastal and Shelf Science*, *278*, 108106. https://doi.org/10.1016/j.ecss.2022.108106
4. Diab, H., Younes, R., & Lafon, P. (2017). Survey of Research on the Optimal Design of Sea Harbours. *International Journal of Naval Architecture and Ocean Engineering*, *9* (4), 460–472. https://doi.org/10.1016/j.ijnaoe.2016.12.004
5. Bell, M. G. H., Pan, J. J., Teye, C., Cheung, K. F., & Perera, S. (2020). An Entropy Maximizing Approach to the Ferry Network Design Problem. *Transportation Research Part B-Methodological*, *132*, 15–28. https://doi.org/10.1016/j.trb.2019.02.006
6. Männikus, R., Soomere, T., & Najafzadeh, F. (2022). Refraction May Redirect Waves from Multiple Directions into a Harbour: A Case Study in the Gulf of Riga, Eastern Baltic Sea. *Estonian Journal of Earth Sciences*, *71* (2), 80−88. https://doi.org/10.3176/earth.2022.06
7. Najafzadeh, F., Jankowski, M. Z., Giudici, A., Männikus, R., Suursaar, Ü., Viška, M., & Soomere, T. (2024). Spatiotemporal Variability of Wave Climate in the Gulf of Riga. *Oceanologia*. Early access. https://doi.org/10.1016/j.oceano.2023.11.001.
8. Soomere, T. (2003). Anisotropy of Wind and Wave Regimes in the Baltic Proper. *Journal of Sea Research*, *49* (4), 305–316. https://doi.org/10.1016/S1385-1101(03)00034-0
9. Männikus, R., Soomere, T., & Kudryavtseva, N. (2019). Identification of Mechanisms that Drive Water Level Extremes from In Situ Measurements in the Gulf of Riga during 1961−2017. *Continental Shelf Research*, *182*, 22−36. https://doi.org/10.1016/j.csr.2019.05.014.
10. Hanes, D.M., Erikson, & L.H. (2013). The Significance of Ultra-Refracted Surface Gravity Waves on Sheltered Coasts, with Application to San Francisco Bay. *Estuarine, Coastal and Shelf Science*, *133*, 129–136. https://doi.org/10.1016/j.ecss.2013.08.022
11. Orviku K. (2018). *Rannad ja rannikud* [*Beaches and Shores*]. Tallinn University Publishers. [in Estonian].
12. Karimpour, A. (2013). *OCEANLYZ, Ocean Wave Analyzing Toolbox. User Manual*. Available at http://www.arashkarimpour.com/download.html

13. Alari, V., Björkqvist, J.-V., Kaldvee, Mölder, K., Rikka, S., Kask-Korb, A., … & Tõnisson, H. (2022). LainePoiss®—A Lightweight and Ice-Resistant Wave Buoy. *Journal of Atmospheric and Oceanic Technology*, *39* (5), 573–594. https://doi.org/10.1175/JTECH-D-21-0091.1
14. Eelsalu, M., Org, M., & Soomere, T. (2014). Visually observed wave climate in the Gulf of Riga. In *The 6th IEEE/OES Baltic Symposium Measuring and Modeling of Multi-Scale Interactions in the Marine Environment*, May 26–29, Tallinn, Estonia. IEEE Conference Publications, 6887829. https://doi.org/10.1109/BALTIC.2014.6887829
15. Booij, N., Ris, R.C., & Holthuijsen, L.H. (1999). A Third-Generation Wave Model For Coastal Regions: 1. Model Description and Validation. *Journal of Geophysical Research-Oceans*, 104 (C4), 7649–7666. https://doi.org/10.1029/98JC02622.
16. The SWAN team. (2021). *SWAN Scientific and Technical Documentation.* Technical Report. Delft University of Technology. Available at http://swanmodel.sourceforge.net/download/zip/swantech.pdf
17. Baltic Sea Hydrographic Commission. (2013). *Baltic Sea Bathymetry Database Version 0.9.3.* Available at http://data.bshc.pro/
18. Shore Protection Manual. (1984). *Coastal Engineering Research Center.* Department of the Army. US Army Corps of Engineers, Washington DC.
19. Kamphuis, J.W. (2010). *Introduction to Coastal Engineering and Management* (2nd ed.). Advanced Series of Ocean Engineering, 30. World Scientific, New Jersey. https://doi.org/10.1142/7021
20. Hersbach, H., Bell, B., Berrisford, P., Biavati, G., Horányi, A., Muñoz Sabater, J., … & Thépaut, J-N. (2018). *ERA5 Hourly Data on Pressure Levels from 1979 to Present.* Copernicus Climate Change Service (C3S) Climate Data Store (CDS). Available at https://doi.org/10.24381/cds.bd0915c6
21. Hersbach, H., Bell, B., Berrisford, P., Hirahara, S., Horanyi, A., Munoz-Sabater, J., … & Thepaut, J. N. (2020). The ERA5 Global Reanalysis. *Quarterly Journal of the Royal Meteorological Society*, *146* (730), 1999–2049. https://doi.org/10.1002/qj.3803
22. ECMWF. (2006). *IFS Documentation – Cy41r2. Operational Implementation 8 March 2016. Part IV: Physical Processes*. Available at https://www.ecmwf.int/en/elibrary/79697-if
23. Soomere, T., & Keevallik, S. (2001). Anisotropy of Moderate and Strong Winds in the Baltic Proper. *Proceeding of the Estonian Academy of Sciences. Engineering*, *7* (1), 35–49. https://doi.org/10.3176/eng.2001.1.04
24. Männikus, R., Soomere, T., & Viška, M. (2020). Variations in the Mean, Seasonal and Extreme Water Level on the Latvian Coast, the Eastern Baltic Sea, during 1961–2018. *Estuarine, Coastal and Shelf Science*, *245*, 106827. https://doi.org/10.1016/j.ecss.2020.106827
25. Coles, S. (2004). *An Introduction to Statistical Modeling of Extreme Values* (3rd printing). Springer, London.
26. Holthuijsen, L. H. (1999). *Waves in Oceanic and Coastal Waters*. Cambridge University Press, Cambridge.
27. Männikus, R., & Soomere, T. (2023). Directional Variation of Return Periods of Water Level Extremes in Moonsund and in the Gulf of Riga. Baltic Sea. *Regional Studies in Marine Science*, 57, 102741. https://doi.org/10.1016/j.rsma.2022.102741
28. Wang, W., Pákozdi, C., Kamath, A., Fouques, S., & Bihs, H. (2022). A Flexible Fully Nonlinear Potential Flow Model for Wave Propagation over the Complex Topography of the Norwegian Coast. *Applied Ocean Research*, *122*, 103103. https://doi.org/10.1016/j.apor.2022.103103
29. Wang, W., Pákozdi, C., Kamath, A., & Bihs, H. (2023). Fully Nonlinear Phase-Resolved Wave Modelling in the Norwegian Fjords for Floating Bridges along the E39 Coastal Highway. *Journal of Ocean Engineering and Marine Energy*, *9*, 567–586. https://doi.org/10.1007/s40722-023-00284-z

30. Bihs, H., Kamath, A., Alagan Chella, M., Aggarwal, A., & Arntsen, Ø. A. (2016). A New Level Set Numerical Wave Tank with Improved Density Interpolation for Complex Wave Hydrodynamics. *Computers & Fluids*, *140*, 191–208. https://doi.org/10.1016/j.compfluid.2016.09.012
31. Van der Vorst, H. (1992). BiCGStab: A Fast and Smoothly Converging Variant of Bi-CG for the Solution of Nonsymmetric Linear Systems. *SIAM Journal of Scientific Computing*, *13* (2), 631–644. https://doi.org/10.1137/0913035
32. Jiang, G. S., & Shu, C. W. (1996). Efficient Implementation of Weighted ENO Schemes. *Journal of Computational Physics*, *126* (1), 202–228. https://doi.org/10.1006/jcph.1996.0130
33. Shu, C.W., & Osher, S. (1988). Efficient Implementation of Essentially Non-Oscillatory Shock Capturing Schemes. *Journal of Computational Physics*, *77* (2), 439–471. https://doi.org/10.1016/0021-9991(88)90177-5
34. Larsen, J., & Dancy, H. (1983). Open Boundaries in Short Wave Simulations – A New Approach. *Coastal Engineering*, *7* (3), 285–297. https://doi.org/10.1016/0378-3839(83)90022-4
35. Mazzaretto, O.M., Menéndez, M., & Lobeto, H. (2022). A Global Evaluation of the JONSWAP Spectra Suitability on Coastal Areas. *Ocean Engineering*, *266* (2), 112756. https://doi.org/10.1016/j.oceaneng.2022.112756.
36. Eelsalu, M., Soomere, T., Pindsoo, K., & Lagemaa, P. (2014). Ensemble Approach for Projections of Return Periods of Extreme Water Levels in Estonian Waters. *Continental Shelf Research*, *91*, 201–210. https://doi.org/10.1016/j.csr.2014.09.012
37. Johansson, M., Boman, H., Kahma, K. K., & Launiainen, J. (2001). Trends in Sea Level Variability in the Baltic Sea. *Boreal Environment Research*, *6* (3), 159–179.
38. Soomere, T., & Pindsoo, K. (2016). Spatial Variability in the Trends in Extreme Storm Surges and Weekly-Scale High Water Levels in the Eastern Baltic Sea. *Continental Shelf Research*, *115*, 53–64. https://doi.org/10.1016/j.csr.2015.12.016
39. Kozanis, S., Christofides, A., Mamassis, N., Efstratiadis, A., & Koutsoyiannis, D. (2010). Hydrognomon – Open Source Software for the Analysis of Hydrological Data. *Geophysical Research Abstracts*, *12*, 12419. http://dx.doi.org/10.13140/RG.2.2.21350.83527
40. Goda, Y. (2010). *Random Seas and Design of Maritime Structures* (3rd ed.). Advanced Series on Ocean Engineering 33. World Scientific, New Jersey. https://doi.org/10.1142/7425
41. Männikus, T., Soomere, T., & Suursaar, Ü. (2024). How do Simple Wave Models Perform Compared with Sophisticated Models and Measurements in the Eastern Baltic Sea? *Estonian Journal of Earth Sciences*, *73* (2).
42. Ranasinghe, R., & Turner, I. L. (2006). Shoreline Response to Submerged Structures: A Review. *Coastal Engineering*, *53* (1), 65–79. https://doi.org/10.1016/j.coastaleng.2005.08.003
43. Fitri, A., Hashim, R., Abolfathi, S., & Maulud, K. N. A. (2019). Dynamics of Sediment Transport and Erosion-Deposition Patterns in the Locality of a Detached Low-Crested Breakwater on a Cohesive Coast. *Water*, *11* (8). https://doi.org/10.3390/w11081721

sciendo

LATVIAN JOURNAL OF PHYSICS
AND TECHNICAL SCIENCES
2024, N 6

DOI: 10.2478/lpts-2024-0041

RETROFITTING URBAN HEATING SYSTEMS UNDER THE EU FIT FOR 55 PACKAGE: METHODOLOGY FOR FEASIBILITY STUDIES OF PROJECTS

G. Karnitis[1*], S. Gendelis[2], M. Pukis[3], U. Sarma[4], E. Diebelis[1],
E. Karnitis[1], J. Bicevskis[1]

[1]University of Latvia, Faculty of Computing,
19 Raina Blvd., Riga, LV-1586, LATVIA
[2]University of Latvia, Faculty of Physics,
Mathematics and Optometry,
3 Jelgavas Str., Riga, LV-1004, LATVIA
[3]University of Latvia, Faculty of Business,
Management and Economics,
5 Aspazijas Blvd., Riga, LV-1050, LATVIA
[4]Latvenergo AS
12 Pulkveza Brieza Str., Riga, LV-1230, LATVIA
*e-mail: girts.karnitis@lu.lv

Heating accounts for significant primary resource consumption and generation up to 30 % of total GHG emissions in the EU27. The ambitious emissions reduction goals outlined in the European *Green Deal* and *Fit for 55* package necessitate not only the massive renovation of building stocks, but also reconstruction of heat generation and supply systems. With 76 % of the EU building stock located in urban areas, the renewal of urban heating systems is crucial.

An easy-to-use methodology has been developed for managing long-term renovation programmes and regularly assessing renovation projects, thereby forming a comprehensive dynamic vision on the progress. This methodology enables flexible, rapid and, at the same time, sufficiently accurate and objective analysis of the potential and benefits of various heating system renovation projects and their variants at the pre-design stage, as well as their comparison according to efficiency. It employs a limited number of open indicators and does not require specialised knowledge in thermal physics, economics and/or construction.

The developed methodology provides insights into (1) achievable heat consumption and primary energy savings, (2) reduction of dominant CO_2 emissions, (3) changes in heating tariffs and costs, and (4) required investments.

The methodology is intended for use by: (1) municipalities to streamline sustainable planning and management of urban heating systems and to facilitate interaction with owners of buildings and local heating systems, and (2) national authorities monitoring the implementation of national programmes under *Fit for 55*.

Keywords: *Energy efficiency, Fit for 55, renovation, simulation, urban heating system.*

1. INTRODUCTION

The political initiative European Green Deal (GD) [1] and supporting Fit for 55 (FF55) legislative package [2] envisage an ambitious target – achieving a climate-neutral European Union (EU) by 2050. It is expected to reduce net greenhouse gas (GHG) emissions by 55 % by 2030. The regulatory documents of the FF55 package were updated [3], heightening the mandatory requirements for the EU countries.

The building sector is responsible for generation of up to 30 % of total GHG emissions in the EU27; up to 75 % of the EU's 120 million building stock remains energy inefficient. The revised Energy Performance of Buildings Directive [4] mandates that at least 3 % of the total floor area of buildings owned by the public administration at all levels must be renovated each year. Since public buildings constitute only 10 % of the total EU building stock, achieving these ambitious targets will require similar dynamics in the massive deep renovation of private buildings, as well as in reconstruction of heat production and supply systems. The amended Renewable Energy Directive [5] has increased the EU's renewable energy target for 2030 to a minimum of 42.5 %, with a perspective target of 45 %, nearly doubling the current share of renewable energy in the EU.

Given that 76 % of the EU building stock is in urban areas, the active and successful implementation of the programme in cities is crucial. The term *renovation wave* has appeared in policy documents [6], analytical papers [7], and studies [8], [9], figuratively comparing the scale of the required retrofitting in Europe to the magnitude of the Marshall Plan [10].

The FF55 will not provide full funding for long-term (until 2050) heating system retrofitting programmes. Consequently, management must reckon with lot of various financing options with different conditions and target variables. A prompt and convincing response to each call for projects with an application, tailored to specific requirements, is critical for a successful retrofitting process at the national and/or urban scale. This necessitates a flexible pre-design assessment of the project's potential benefits.

Numerous methodologies have been proposed for evaluating retrofitting scenarios. Renovation of individual buildings is the most studied issue. These methodologies are based on various approaches, primarily but not limited to economic (e.g., [11]), sustainability (e.g., [12]), architectural (e.g., [13]), environmental (e.g., [14]) aspects and benefits. Studies in this area include both theoretical and experience-based research (e.g., [15]).

Published methodologies are also available for large-scale retrofitting of building blocks [16] and for buildings with centralised or local energy sources [17], [18]. Along with the calculators from pipe manufacturers [19], the integration of the heating system's reconstruction with the transition to 4G district heating (DH) system [20], and the impact of global warming on heat consumption [21] have also been studied. An urban model based on energy prosumption within building blocks is described in [22].

Managing such large-scale programmes is a significant challenge. The main management duties and responsibilities related to the renovation wave are defined at the national level [23]. However, the proactive involvement of municipalities is essential [24]. Municipalities are responsible for strategic development planning of the territory and sustainable management of urban heating systems [25]–[27], including reducing the burden of heating costs on municipal and household budgets [28].

The proposed methodologies are often poorly usable for pre-design modelling and evaluation of the potential benefits of the specific project to comply with:

- the defined obligations of the EU Member States in reduction of GHG emissions and primary energy resource consumption;
- the interests of local governments in the sustainable socio-economic development of their territories;
- the interests of the population and entrepreneurs in reducing heating costs.

To address these needs, an easy-to-use methodology has been created for developing and managing long-term heating system retrofitting programmes and for the regular assessment of ongoing retrofitting projects to form a comprehensive dynamic vision on the progress. The developed methodology provide insights into (1) achievable heat consumption and primary energy savings, (2) reduction of dominant CO_2 emissions, (3) changes in heating costs, and (4) necessary investments. It employs a limited number of key indicators and does not require specific knowledge in thermal physics, economics and/or construction. The methodology is based on directly computing changes in the aforementioned target variables, including in the simulation only those aspects that are affected by the retrofitting process.

The proposed methodology allows for flexible, rapid, and sufficiently accurate and objective simulation of the potential and benefits of various renovation projects and their variants at the pre-design stage, as well as their comparison in terms of efficiency from various perspectives.

The methodology is intended for use by: (1) national authorities to control and monitor the implementation of national programmes under FF55, including one-stop shops [4], (2) municipalities to streamline the sustainable planning and management of the urban heating systems, and (3) owners and managers of buildings and local heating systems to maintain properties.

2. MATERIALS AND METHODS

2.1. Basics of the Methodology

So far, no universal, user-friendly model has been developed for simulating entire urban heating systems. The number of drivers is vast, including the specific locations of buildings and heat sources (HSs), as well as the unique topography of each city's DH network. Physical causal relationships are week between most of the parameters of system components, and often between the indicators of each component. Therefore, it is impossible to mathematically determine the key drivers of the overall heating process (e.g., using algorithms described in [29]), only specific, narrower tasks can be solved (e.g., [28]). Instead, evaluations have been performed on a per-element basis to identify and exclude less significant entities and their indicators from the calculations.

EU policy documents and the following normative and financial conditions of the renovation projects are primarily focused on achievable saving in consumption of heat (ΔQ) and primary energy resources (ΔR), reductions in dominant CO_2 emissions (ΔE) and heating costs (ΔC). This focus allows for the use of direct computing of these changes within the methodology's algorithm [30], [31]. This approach offers a significant comparative advantage over calculations of heat consumption before and after retrofitting. Aspects unaffected by retrofitting actions, such as building orientation (solar heat gains), their functionality (internal heat gains and hot water consumption), DH network configuration and temperature regime, fixed costs of heat production, can be ignored. This algorithm significantly reduces the number of key indicators and effectively minimises uncertainties in the calculations, thereby enhancing both accuracy and simplicity.

The methodology is intended for the integration of many potential urban heating system reconstruction projects, forming a long-term retrofitting programme. The analysis of each project variant and the search for the optimum solution for the individual project, as well as the overall optimum of the programme, can be conducted at the pre-design stage to achieve set goals at the lowest possible cost, following the principle of an innovative sandbox.

Given the typically short deadlines for submission of project application, the pre-design stage prioritises quick, simplified computations for comparative assessment of project variants over high accuracy. Therefore, the simulation uses the minimum possible number of indicators.

Figure 1 illustrates the methodology applied to the simulation of a virtual urban heating system retrofitting project. The project involves renovating a block of seven buildings B_1–B_7. Each renovated building achieves a reduction in heat energy demand denoted as ΔQ_B, except for building B_7, which will not be renovated ($\Delta Q_{B7}=0$). Local heat sources (LHSs) are used in buildings B_1 and B_4. Buildings B_2, B_3, B_5, B_6 and B_7 are connected to the DH network via inlet pipes, with nominal diameters (D_B) and lengths (L_B). Many blocks of buildings connected to the DH network will not be renovated within this specific project. The network is connected to the centralised heat source (CHS); heat loss from pipes Q_{lsec} occurs in each network section, with the total network losses being Q_{lnet}.

After the project completion, the heat sources (HSs) generate the necessary amounts of thermal energy reduced by ΔQ_{sup} and correspondingly emit reduced amounts of CO_2. The ΔQ_{sup} for LHSs, equal to heat energy savings ΔQ_{B1} and ΔQ_{B4}, respectively, do not affect the calculations for centralised heating; they are included when calculating the total reduction in the project's thermal energy consumption ΔQ_{proj}.

The methodology does not require specialised information, as all necessary data is available:

- City-level indicators are available in normative documents:
  - heating period for DH – P_{heat} [days/year];
  - minimum temperature during the heating period – T_{min} [°C];
  - average temperature during the heating period – T_{out} [°C].

- Energy performance certificates for properties are mandatory documents [4] meticulously prepared by qualified professionals; they provide comprehensive qualitative data essential for evaluating the energy performance of buildings; their relevant supporting documents are also available.

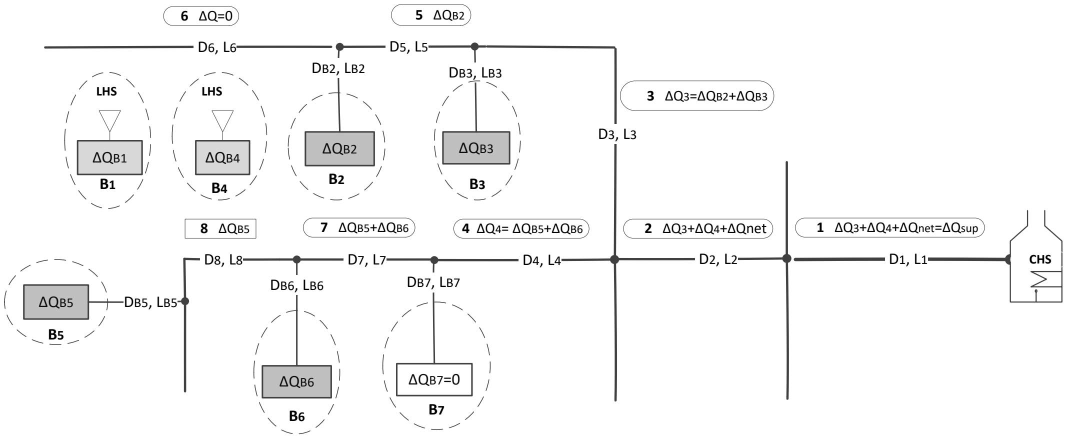

Fig. 1. Virtual urban heating system's retrofitting project. Developed by the authors.

- DH network operators possess:
  - topographic and constructive data of the network and pipes;
  - hot water supply period – P_{hw} [days/year].
- CHS operator have data on centralised heat production.
- Building managers have data on LHS and their operation.

The methodology assumes that efficient heat production and transmission/distribution has been ensured:

- heat sources have been technologically retrofitted, their thermal efficiency meets current standards, and they are properly maintained and operated;
- DH network's pre-insulated pipes comply with the norms [32]; they have been constructed according to the maximum heat load.

The methodology does not cover the reconstruction of the internal pipe network of buildings, as well as changes in the topography of the DH network.

2.2. Renovation of Buildings

In the context of data processing, a building is a complex system consisting of technologically and structurally related elements, such as walls, windows, doors, roof, foundation, ventilation systems as well as technical systems. However, in context of thermal efficiency, the interactions between elements are week. Therefore, each element can be evaluated separately, and achieved individual benefits can be summed using an empirical generalised coefficient η.

The building-level indicators used in the methodology are available from energy certificates:

- heated area – A [m^2];
- heated indoor volume – V [m^3];
- indoor temperature – T_{ind} [°C];
- specific thermal energy consumption for heating before renovation – Q_{spec} [kWh/m^2/year].

If a building has several different wall constructions, windows, exterior doors, etc., the data input of each individual variant of these elements is provided. The reduction of heat loss for each corresponding element ΔQ_{elem} is calculated by summing up the savings of the specific constructive entities.

Renovation of windows and exterior doors involves replacing them with higher quality ones that have lower thermal transmittance U_{new} [W/(m^2*K)] compared to the initial ones (U_{ini}). Since the overall heat transfer variances due to different window frames and exterior door constructions are small, if the area of the elements S_{elem} [m^2] does not change during the renovation, then the reduction of transmission heat losses ΔQ_{trans} can be calculated as follows:

$$\Delta Qtrans = 24 * 10^{-6} * S_{elem} * (T_{ind} - T_{out}) * P_{heat} * (U_{ini} - U_{new}) \ \ [\text{MWh/year}]. \qquad (1)$$

The reduction of heat loss for replacing external doors:

$$\Delta Q_{door} = \Delta Q_{trans}.$$

Replacing windows automatically reduces air infiltration into the room and, therefore, heat loss, as gaps are reduced. Reduction of ventilation heat losses ΔQ_{wvent} can be calculated as follows:

$$\Delta Q_{wvent} = 0.34 * 0.6 * 24 * 10^{-6} * V * P_{heat} * (T_{ind} - T_{out}) * (1 - Kw) \ \ [\text{MWh/year}], \qquad (2)$$

where K_w, when replacing the old wooden windows, is set to 0.8, while for replacing old PVC windows, K_w is set to 0.9.

The total reduction of heat loss for replacing windows can be calculated as follows:

$$\Delta Q_{wind} = \Delta Q_{trans} + \Delta Q_{wvent} \ \ [\text{MWh/year}]. \qquad (3)$$

Renovation of external walls, roofs/ceilings and foundations/basements involves covering them with thermal insulation materials, which have much lower thermal conductivity than the constructive materials (concrete, bricks, etc.). The thermal conductivities of insulation materials (polystyrene foam, stone/mineral wool, wood fibre, etc.) differ only slightly, so an average value $\lambda = 0.04$ [W/(m*K)] is assumed in the computing. Consequently, only the thickness d [m] of the thermal insulation material is used as a driver. The reduction of heat loss ΔQ_{elem} (specif., ΔQ_{walls}, ΔQ_{roof}, ΔQ_{found}) due to insulation can be calculated as follows:

$$\Delta Q_{elem} = 24 * 10^{-6} * S_{elem} * (T_{ind} - T_{out}) * P_{heat} * (U_{constr} - U_{cins}) \ \ [\text{MWh/year}], \qquad (4)$$

where U_{constr} – thermal transmittance of the constructive material [W/(m^2*K)];
U_{cins} – thermal transmittance of the insulated element [W/(m^2*K)]:

$$U_{cins} = 1/((1/U_{constr}) + d/0.04). \tag{5}$$

Retrofitting ventilation system should be planned for buildings with only natural ventilation. The heat savings ΔQ_{vent} achieved by installing a mechanical ventilation system with recuperation can be calculated, assuming an air heat capacity of 0.34 [Wh/m^3/^{0}C] and an average air change rate before renovation of 0.6 [1/h]. The heat savings will be as follows:

$$\Delta Q_{vent} = 0.34 * 0.6 * 24 * 10^{-6} * V * P_{heat} * (T_{ind} - T_{out}) * (1 - K_f) \quad [\text{MWh/year}], \tag{6}$$

where: K_f – coefficient determined by the functionality of the building; in the case of multi-apartment building local wall-mounted heat recovery units are typically installed, resulting in $K_f = 0.5$, while for buildings with other functionalities, a centralised ventilation system is developed, leading to $K_f = 0.2$.

Improvements to the technical systems of buildings encompass various automation and control technologies that optimise heating and ventilation to increase smart readiness level of buildings [4]. Estimates of potential heat savings vary. Source [33] reports savings between 7 % and 34 % in energy for heating, ventilation, and air conditioning. Telia analysts estimate an average reducing of about 13 % in heat energy consumption for residential and office buildings, schools, and libraries in Northern Europe and the Baltic States, constructed before 1965 [34], through comprehensive system modernisation. Assuming that the modernisation of the technical systems of buildings in Latvia will not be carried out completely everywhere, and the indoor climate control settings may not be fully utilised, a conservative estimate predicts savings ΔQ_{tsyst} of 10 % in thermal energy consumption for renovated buildings.

Reduction in heat consumption ΔQ_{BC} obtained due to renovation of building constructive elements is as follows:

$$\Delta Q_{BC} = \delta * \sum \Delta Q_{elem}, \tag{7}$$

where

$$\sum \Delta Q_{elem} = \Delta Q_{walls} + \Delta Q_{wind} + \Delta Q_{doors} + \Delta Q_{roof} + \Delta Q_{found} + \Delta Q_{vent}, \tag{8}$$

δ – empirical factor of interactions of elements renovation:
in case of renovation of any one element $\delta = 1$;
in case of renovation of several elements and $\Delta Q_{vent} = 0$, $\delta = 0.85$;
in case of renovation of several elements and $\Delta Q_{vent} > 0$, $\delta = 0.75$.

If total building thermal energy consumption for heating before renovation is denoted as Q:

$$Q = 10^{-3} * Q_{spec} * A \; [\text{MWh/year}],$$

$$\text{then } \Delta Q_{tsyst} = 0.1 * (Q - \Delta Q_{BC}), \tag{9}$$

and total reduction in heat consumption ΔQ_{BE} obtained due to renovation of building elements is as follows:

$$\Delta Q_{BE} = \Delta Q_{BC} + \Delta Q_{tsyst}. \tag{10}$$

Accordingly, the maximum heat load of

the building at the minimum temperature of the heating period T_{min} decreases from the pre-renovation size Q_{hl} by ΔQ_{hl}; it will be:

$$Q_{hl} - \Delta Q_{hl} = (Q - \Delta Q_{BE}) * (T_{ind} - T_{min})/(24 * P_{heat} * (T_{ind} - T_{out}))\ [MW]. \tag{11}$$

The necessary investments C_{elem} for renovation of building elements are calculated as follows:

$$C_{elem} = N_{elem} * C_{spelem}\ [EUR], \tag{12}$$

where

N_{elem} – size of the element [m^2]; size of heated area A is used for ventilation and technical systems, size of area S – for other elements;

C_{spelem} – specific renovation costs [EUR/m^2]; a library of indicative data is added to the methodology for use by default; users can enter another value of C_{spelem}.

2.3. Reconstruction of District Heating Network

Implementing ambitious energy efficiency programmes significantly reduces heat consumption in renovated buildings, thereby decreasing the load on DH networks. This creates a potential opportunity for additional heat savings by reconstructing the network and reducing heat losses.

Developing a universal user-friendly model to simulate an entire DH network is practically impossible. Several drivers of the model, e.g., the locations of buildings and CHSs, as well as the network's topography, are too specific for each city. However, it is possible to create a simplified model for individual network sections that provide a heat carrier flow to the buildings being renovated. The general assumptions for such a model are as follows:

- flows in the network sections are assumed to be constant, corresponding to the thermal energy load of the respective consumers;
- the dimensions (internal nominal diameters D_{nom}) of the existing pipes are chosen adequately, ensuring that the overall maximum load for heating and hot water supply is greater than the maximum heat load of the next thinner standard pipes.

Heat loss from pipes is determined by the thermal insulation and its thickness, the outer surface area of the pipes, and the temperature difference between the heat carrier and the external environment (ground). A decrease in heat demand by ΔQ_{BE} results in a decrease in heat mass transfer and flow rate of the heat carrier, which affects hydraulic processes, but has a negligible effect on the thermal conductivity and heat loss.

However, in the event of a massive building renovation, the maximum required heat load of a network section ($\sum Q_{hl}$ of supplied buildings) may decrease to a level that can be provided by thinner pipes. Reducing the size of pipes during network reconstruction is the only viable activity for reducing heat loss in the section Q_{lsec} by the ΔQ_{lsec}.

Two complex indices have been developed to simulate the thermal regime in DH sections consisting of supply and return pipes; the D_{nom} is the key driver of both indices (see Table 1). One of these indices *Specific Heat Losses* from the pipes F_{loss} [W/m] is determined by the construction parameters of standardised pre-insulated pipes:

$$F_{loss} = f\{D_{nom}, C_s, A_{ins}, U_{ins}\}\ [W/m], \tag{13}$$

where
Cs – wall thickness of the metal pipes [mm];
A_{ins} – the thickness of the insulation layer [mm];
U_{ins} – thermal transmittance (U-value) of the insulation [W/(m²*K)].

An index *Maximum Heat Load* F_{hl} [MW] for a pipe of a nominal diameter D_{nom} is determined by the operating regime of the DH network. The latter is similar enough across all networks in the country, so the index can be equalised nationally. To have a reasonable reserve for the heat carrier flow, F_{hl} is set at 80 % of the theoretical maximum.

$$F_{hl} = f\{D_{nom}, T_{sup}, T_{ret}, V_{car}\} \text{ [MW]}, \quad (14)$$

where
T_{sup} – the average temperature of the heat carrier in the supply pipe (70 °C by default];
T_{ret} – the average temperature of the heat carrier in the return pipe (30 °C by default);
V_{car} – optimal flow rate of the heat carrier [m/sec].

Table 1. Complex Indices for Simulating Heat Transfer in DH Network Pipes

Internal nominal diameter Dnom [mm]	Maximum Heat Load Fhl [MW]	Specific Heat Losses Flos [W/m]
25	0.04	14.93
32	0.06	15.09
40	0.10	18.62
50	0.21	20.16
65	0.36	23.93
80	0.54	26.42
100	0.84	25.88
125	1.64	30.47
150	2.37	35.54
200	4.21	39.78
250	7.89	37.56
300	11.36	44.20
350	15.47	50.47
400	20.20	53.80
450	29.83	53.07
500	36.83	50.01
600	53.03	62.49
700	72.18	72.99
800	107.75	83.71
900	136.37	95.44
1000	168.36	107.48

The algorithm for calculating the potential ΔQ_{lsec} in the network section is as follows:

1. identify the sections, through which heat is supplied to buildings to be renovated;
2. determine the reduction in heat supply for each of these sections ΔQ_{supsec}:

$$\Delta Q_{supsec} = \sum \Delta Q_{BE}; \quad (15)$$

3. calculate the reduction in maximum heat load ΔQ_{hlsec} by transforming the expression (11):

$$\Delta Q_{hlsec} = Q_{supsec} * (T_{ind} - T_{min})/(24 * P_{heat} * (T_{ind} - T_{out})) \text{ [MW]}; \quad (16)$$

4. calculate the reduced maximum heat load F_{hlsec}, assuming that the initial maximum heat load before the reconstruction F_{hlini} is equal to maximum heat load for the used pipes (the worst case for transition to thinner pipes):

$$F_{hlsec} = F_{hlini} - \Delta Q_{hlsec} \quad [MW];$$

5. evaluate the possibility to choose thinner pipes, which maximum heat load is F_{hlthi}, if:

$$F_{hlsec} < F_{hlthi};$$

6. calculate the reduction of heat loss ΔQ_{lsec} obtained from the replacement of both supply and return pipes for the entire time P_{hc}, while there is a hot heat carrier in the pipes:

$$\Delta Q_{lsec} = 24 * 10^{-6} * L_{sec} * (F_{losini} - F_{losthi}) * P_{hc} \quad [MWh/year], \qquad (17)$$

where:
L_{sec} – section pipe length [m];
F_{losini} – initial specific heat losses from the section pipes [W/m];
F_{losthi} – specific heat losses from thinner section pipes [W/m];
$P_{hc} = \max \{P_{heat}, P_{hw}\}$.

The total heat energy saving in the DH network ΔQ_{lnet} is calculated by summing up the heat loss reductions in all sections:

$$\Delta Q_{lnet} = \sum \Delta Q_{lsec} \ [MWh/year]. \qquad (18)$$

The necessary investments C_{sec} for replacement of network sections are calculated as follows:

$$C_{sec} = L_{sec} * C_{sppipe} \ [EUR],$$

where
C_{sppipe} – specific replacement costs [EUR/m]; a library of indicative data is added to the methodology for use by default; users can enter another value of C_{sppipe}.

2.4. Reconstruction of Heat Sources

Renovating buildings and reconstructing DH network pipes reduce overall heat consumption by ΔQ_{proj}. However, the CO_2 emissions associated with heating are produced as a by-product when HSs convert primary energy into thermal energy.

The production and supply of required amount of heat Q_{sup} are the key functions of any HS, indicating its efficiency and suitability. For CHS, Q_{sup} is the amount of heat energy measured by the output gauge and transferred through the network for consumption by both renovated in the specific project and unrenovated buildings. In the case of LHS, there is usually no such meter, so the heat consumption recorded in the energy performance certificate of the relevant building is used as Q_{sup} for computing.

In each HS, the amount of produced and supplied heat is reduced by ΔQ_{sup} due to the renovation of buildings and the reconstruction of network sections. Consequently, the consumption of primary energy resource has decreased by ΔR, leading to a reduction in CO_2 emissions by ΔE:

$$\Delta R = \Delta Q_{sup}/\eta \quad [MWh/year]$$
$$\Delta Q_{proj} = \sum \Delta Q_{sup} = \sum \Delta Q_{BE} + \sum \Delta Q_{lnet} \ [MWh/year]$$
$$\Delta E = \alpha * \Delta R = \beta * \Delta Q_{sup} \quad [kg/year], \qquad (19)$$

where parameters, which are normatively determined [35] or technologically achievable (Table 2):
η – coefficient of performance of a typical HS using the relevant primary resource;
α – emission factor of the primary resource [kg/MWh];
$\beta = \alpha/\eta$ – emission indicator of the primary energy resource [kg/MWh].

If several primary energy resources R_p are used for heat production, β is combined considering the specific weight $¥_p$ of the reduction in each primary resource consumption ΔR_p in the total primary resource saving ΔR; in this case:

$$\beta = \sum \beta_p * ¥_p.$$

Table 2. Indicative Parameters of Primary Energy Resources

Primary energy resource	η	α [kg/MWh]	β [kg/MWh]
Natural gas	0.92	202	220
Wood chips	0.8	40	50
Diesel	0.9	267	296
Wood pellets	0.85	40	47
LPG	0.9	227	252
Solar energy	0.98	0	0
Electricity	0.98	109	111

Expression (19) shows that there is also another driver, which determines the reduction of emissions ΔE – the emission indicator of the primary energy resource β. To achieve maximum benefits, the heat demand, which is reduced by ΔQ_{sup} by retrofitting, could be produced utilising a higher quality (*greener*) primary resource with lower emission indicator β_q. Then the initial amount of CO_2 emissions decreases by ΔE:

$$\Delta E = (\beta - \beta_q) * Q_{sup} + \beta_q * \Delta Q_{sup} \text{ [kg/year]}. \quad (20)$$

As can be seen:

- if primary energy resource or its structure has not been changed: $\beta_q = \beta$;
- if only primary energy resource or its structure has been changed: $\Delta Q_{sup} = 0$.

The transition to a greener energy resource requires the replacement of heat source equipment; need investments depend on the type of primary resource to be used; a library of indicative data is added to the methodology for use by default; users can enter another value. The investment payback is included in the heat energy costs during the payback period.

3. RESULTS AND DISCUSSION

The total heat consumption savings due to building renovation ΔQ_B (fig. 1) is computed as follows:

$$\Delta Q_B = \Delta Q_{BE} + \Delta Q_{linsec} \text{ [MWh/year]}, \quad (21)$$

where ΔQ_{linsec} – reduction of heat loss obtained from the replacement of inlet supply and return pipes.

The specific energy consumption for heating after renovation $Q_{specren}$:

$$Q_{specren} = Q_{spec} - 10^3 * \Delta Q_{BE}/A \text{ [kWh/year]}. \quad (22)$$

Achieved primary energy saving ΔR_B:

$$\Delta R_B = \Delta Q_B/\eta_q \ [\text{MWh/year}], \qquad (23)$$

leading to a reduction in dominant CO_2 emissions by ΔE_B (see (20)).

The necessary investments C_B for retrofitting and changes in heating costs for the specific building are calculated as usual, necessary libraries of indicative data are added to the methodology for use by default. The retrofitting costs and prices of the primary energy resources and technologies are factors that will determine the economic basis of the project. The methodology foresees indicative costs available to the user by default. Since the costs are particularly volatile in large amplitudes, the user is invited to enter specific costs at a place and time.

The total benefits of the project and/or programme are calculated by summing up the benefits from buildings and/or projects. The investment payback period used for the calculation of the reduction in heating tariffs is assumed by default for expenses for renovation of buildings and reconstructed pipelines of the heat supply network – 20 years, for replacing the heat source – 10 years; periods are subject to change at the management's discretion.

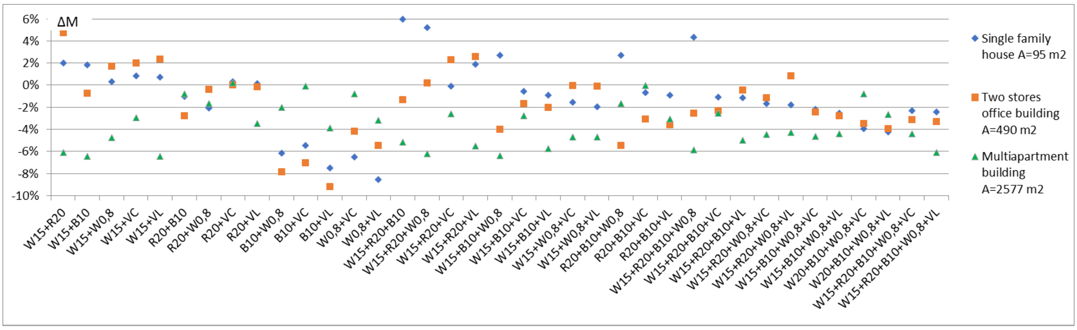

Fig. 2. Computational tests of the methodology. ΔM – the relative difference of the methodology calculation from the full calculation. Renovation scale:
W15 – 15 cm wall insulation, R20 – 20 cm roof insulation,
B10 – 10 cm basement insulation, W0.8 – double-paned windows (U=0.8),
VC – central mechanical ventilation, VL – local ventilation units. Developed by the authors.

The computational testing of the methodology confirms that calculation errors using the proposed methodology for buildings to be renovated typically do not exceed 10 % (Fig. 2). Differences of computed ΔQ_{lsec} values do not exceed 7–8 %; they are most affected by the use of default temperatures T_{sup} and T_{ret}. After the wider application of the methodology and data collection, the possibility of user determination should be re-examined.

The obtained benefits from building renovation are very individual, it is recommended to check the possible options for each building. Figure 3 illustrates the significant potential offered by the methodology in selection of the optimal renovation variants, acting as an innovation sandbox. By varying the renovation tactics, the user can find the most efficient project option to achieve the determining benefit – maximum reduction of CO_2 emissions, economic efficiency of the project, or another one.

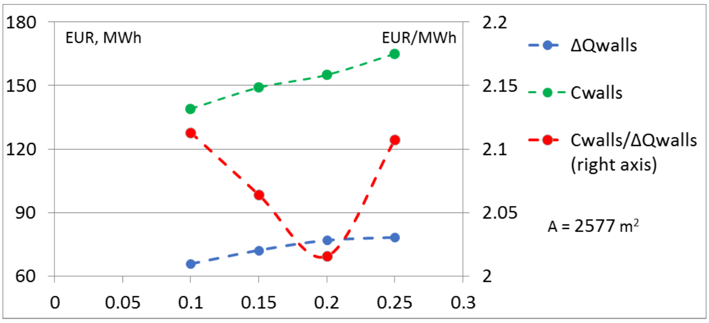

Fig. 3. Optimal price/performance ratio insulating walls.
Developed by the authors.

To reduce the diameter of the pipe D_{nom} by one standard size, the amount of transported heat must decrease by at least 40–60 % (see Fig. 4). It should be noted that, in a general case, not all buildings, to which the heat is supplied through this section, will be renovated. Moreover, the consumption of hot water in the buildings remains unchanged, which adds up to the heating consumption. Therefore, savings ΔQ_{BE} in the buildings under renovation must be increased even more. It means that the greatest chance of achieving a reduction of the maximum heat load, which allows transition to the thinner pipe, is in the building's inlet pipelines (D_B, L_B in Fig. 1), which connect the building under renovation to the DH trunk pipelines.

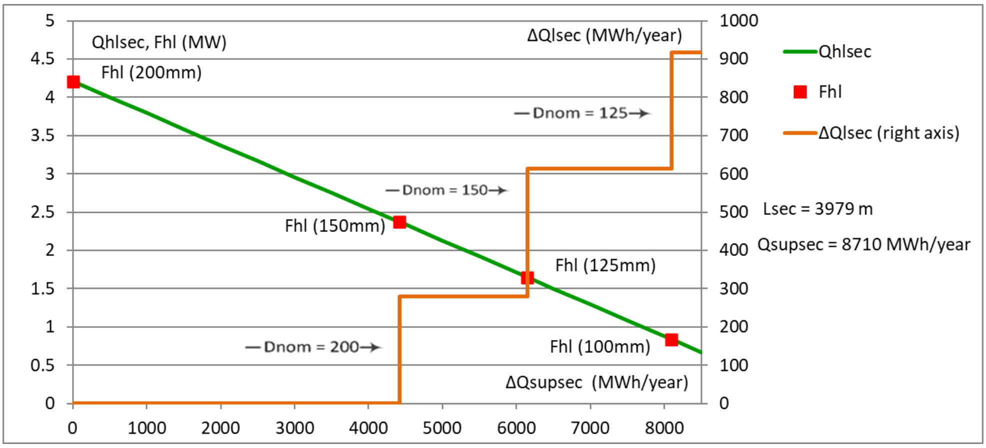

Fig. 4. The obtained loss reduction ΔQ_{lsec} in the DH section due to reduction in heat energy consumption $\sum \Delta Q_{BE}$.
Developed by the authors.

In fact, only the inlet pipelines or LHSs of the buildings to be renovated can be fully attributed to the building renovation project. Only reducing heat production in CHS would be possible in building renovation projects. The reconstruction of trunk sections of DH networks and transitioning to a greener primary energy resource in CHSs typically must be carried out within the framework of special projects. Naturally, the described methodology can be used for pre-design evaluations.

4. CONCLUSIONS

Balancing green initiatives and sustainable socio-economic development in the context of FT55 and other EU-wide policies is a challenge for EU national governments and municipalities, as well as for citizens and entrepreneurs. The described methodology for simulating urban heating system retrofitting projects aims to develop and implement projects that maximally balance the interests of all stakeholders. For this purpose, the methodology: (1) manages all components of the overall urban heating system, (2) is designed to meet the requirements of relevant projects and available funding options, (3) allows for the combination of multiple individual projects, (4) provides objective and sufficiently accurate results for the initial simulation and evaluation of project variants, (5) does not require specific knowledge in thermal physics, economics, or construction, ensuring user-friendliness, and (6) utilises a limited number of indicators to streamline the simulation process.

The major end users of the methodology would be: (1) municipalities and local public institutions to streamline the sustainable planning and management of urban heating systems and to facilitate interaction with owners of infrastructure and local heating systems enabling balanced actions and the identification of priorities, (2) national authorities for monitoring the national implementation of FF55, strategic planning and management of the energy efficiency, ensuring operation of one-stop shops and addressing climate and environmental challenges, and (3) citizens and businesses to make objective decisions for sustainable managing their properties.

ACKNOWLEDGEMENTS

The study has been supported by the Latvian Council of Science project lzp-2021/1-0108 “Sustainable Management of the Urban Heating System under EU Fit for 55 Package: Research and Development of the Methodology and Tool”.

REFERENCES

1. European Council. (2019). *European Council Meeting Conclusions (12 December 2019).* Available at https://www.consilium.europa.eu/media/41768/12-euco-final-conclusions-en.pdf
2. European Council. (2021). *Fit for 55*. Available at https://www.consilium.europa.eu/en/policies/green-deal/fit-for-55-the-eu-plan-for-a-green-transition/
3. EC. (2023). *Commission Welcomes Completion of Key ‘Fit for 55’ Legislation, Putting EU on Track to Exceed 2030 Targets*. Available at https://ec.europa.eu/commission/presscorner/detail/en/IP_23_4754
4. European Council. (2024). *Directive (EU) 2024/1275 of the European Parliament and of the Council of 24 April 2024 on the energy performance of buildings (recast)*. Available at https://eur-lex.europa.eu/legal-content/EN/TXT/?uri=OJ:L_202401275&pk_keyword=Energy&pk_content=Directive
5. EC. (2023). *Renewable Energy Directive*. Available at https://energy.ec.europa.eu/topics/renewable-energy/renewable-energy-directive-targets-and-rules/renewable-energy-directive_en

6. EC. (2020). *Renovation Wave.* Available at https://energy.ec.europa.eu/topics/energy-efficiency/energy-efficient-buildings/renovation-wave_en
7. Vandenbussche, T. (2021). *Is the EU's Building Renovation Wave 'Fit for 55'?* European Policy Centre Policy Brief. Available at https://www.epc.eu/content/PDF/2021/Renovation_wave_PB.pdf
8. Oxford Economics. (2023). *Renovation Wave is Coming in Europe, but not here yet*. Research Briefing. Available at https://www.oxfordeconomics.com/wp-content/uploads/2023/07/Renovation-wave-is-coming-but-not-here-yet.pdf?pi_content=77ee4a0cd14576ad581f7192a5cad163f39cd0a531806f851aad9637fa4e228b
9. Kinay, U., Laukkarinen, A., & Vinha, J. (2023). Renovation Wave of the Residential Building Stock Targets for the Carbon-Neutral: Evaluation by Finland and Türkiye Case Studies for Energy Demand. *Energy for Sustainable Development*, *75*, 1–24. doi.org/10.1016/j.esd.2023.04.014
10. Sweatman, P. (2020). Making the Renovation Wave Work: A Marshall Plan for EU Buildings in Three Simple Steps. *Energia, ambiente e innovazione*, *3*, 44–46. DOI 10.12910/EAI2020-067
11. Huang, J., Wang, S., Teng, F., & Feng, W. (2021). Thermal Performance Optimization of Envelope in the Energy-Saving Renovation of Existing Residential Buildings. *Energy and Buildings*, *247*, 111103. doi.org/10.1016/j.enbuild.2021.111103
12. Pombo, O., Rivela, B., & Neila, J. (2016). The Challenge of Sustainable Building Renovation: Assessment of Current Criteria and Future Outlook. *Journal of Cleaner Production*, *123*, 88–100. doi.org/10.1016/j.jclepro.2015.06.137
13. Jiang, S., Wang, M., & Ma, L. (2023). Gaps and Requirements for Applying Automatic Architectural Design to Building Renovation. *Automation in Construction*, *147*, 104742. doi.org/10.1016/j.autcon.2023.104742
14. Huedo, P., Lopez-Mesa, B., & Mulet, E. (2018). Development of an assessment tool for building envelope retrofit based on environmental indicator. In P. Mercader-Moyano (ed.), *The Sustainable Renovation of Buildings and Neighbourhoods* (pp. 81–102). Bentham Books, Sharjah, U.A.E. DOI: 10.2174/9781681080642115010007
15. Liu, T., Ma, G., Wang, D., & Pan, X. (2024). Intelligent Green Retrofitting of Existing Buildings Based on Case-Based Reasoning and Random Forest. *Automation in Construction*, *162*, 105377. doi.org/10.1016/j.autcon.2024.105377
16. Husiev, O., Campos-Celador, A., Alvarez-Sanz, M., & Teres-Zubiaga, J. (2023). Why District Renovation is not Leading the Race? Critical Assessment of Building Renovation Potential under Different Intervention Levels. *Energy and Buildings*, *295*, 113288. doi.org/10.1016/j.enbuild.2023.113288
17. Teres-Zubiaga, J., Bolliger, R., Almeida, M.G., Barbosa, R., Rose, J., Thomsen, K. E., ... & Briones-Llorente, R. (2020). Cost-Effective Building Renovation at District Level Combining Energy Efficiency & Renewables – Methodology Assessment Proposed in IEA EBC Annex 75 and a Demonstration Case Study. *Energy and Buildings*, *224*, 110280. 9
18. Weinberger, G., Amiri, S., & Moshfegh, B. (2021). Investigating Techno-Economic Effects and Environmental Impacts of Energy Renovation of Residential Building Clusters on a District Heating System. *Energy and Buildings*, *251*, 111327. doi.org/10.1016/j.enbuild.2021.111327
19. Kingspan Group. (2022). *LOGSTOR Calculator*. Available at: https://www.logstor.com/service-support/tools/logstor-calculator
20. Wahi, P., Konstantinou, T., Tenpierik, M.J., & Visscher, H.J. (2023). Lower-Temperature-Ready Renovation: An Approach to Identify the Extent of Renovation Interventions for Lower-Temperature District Heating in Existing Dutch Homes. *Buildings*, *13* (10), 2524. doi.org/10.3390/buildings13102524
21. Ziemele, J., Gendelis, S., & Dace, E. (2023). Impact of Global Warming and Building Renovation on the Heat Demand and District Heating Capacity: Case of the City of Riga. *Energy*, *276*, 127567. doi.org/10.1016/j.energy.2023.127567

22. Bruck, A., Ruano, S.D., & Auer, H. (2022). Values and Implications of Building Envelope Retrofitting for Residential Positive Energy Districts. *Energy and Buildings*, *275*, 112493. doi.org/10.1016/j.enbuild.2022.112493
23. Lihtmaa, L., & Kalamees, T. (2024). Emerging Renovation Strategies and Technical Solutions for Mass-Construction of Residential Districts Built after World War II in Europe. *Energy Strategy Reviews*, *51*, 101282. doi.org/10.1016/j.esr.2023.101282
24. Pūķis, M., Bičevskis, J., Gendelis, S., Karnītis, E., Karnītis, Ģ.,Eihmanis, A., & Sarma, U. (2023). Role of Local Governments for the Green Deal Multilevel Governance: Energy Context. *Energies*, *16* (12), 4759. doi.org/10.3390/en16124759
25. Pozzi, M., Spirito, G., Fattori, F., Dénarié, A., Famiglietti, J., & Motta, M. (2021). Synergies between Buildings Retrofit and District Heating. The Role of DH in a Decarbonized Scenario for the City of Milano. *Energy Reports*, *7* (supl. 4), 449–457. doi.org/10.1016/j.egyr.2021.08.083
26. Pelda, J., Holler, S., & Persson, U. (2021). District Heating Atlas – Analysis of the German District Heating Sector. *Energy*, *233*, 121018. doi.org/10.1016/j.energy.2021.121018
27. BPIE. (2021). *Technical Assistance: Local Authorities Needs and Upcoming Policy*. Available at https://www.bpie.eu/wp-content/uploads/2021/12/BU_TA_0112.pdf
28. Sarma, U., Karnitis, G., Karnitis, E., & Bazbauers, G. (2020). Toward solutions for energy efficiency: Modeling of district heating costs. In M. Tvaronaviciene, & B. Slusarczyk (eds.), *Energy Transformation towards Sustainability*, vol. 1, (pp. 219–237). Elsevier, Amsterdam. doi.org/10.1016/B978-0-12-817688-7.00011-2
29. Karnitis, G., Bicevskis, J., Pukis, M., Sarma, U., Gendelis, S., Eihmanis, A., … & Karnitis, E. (2023). Methodology for Mathemetical Determining Key Performance Indicators of Socioeconomic Processes. *Baltic Journal of Modern Computing*, *11* (1), 114–133. doi.org/10.22364/bjmc.2023.11.1.07
30. Gendelis, S., Bicevskis, J., Eihmanis, A., Karnitis, E., Karnitis, G., Pukis, M., & Sarma, U. (2023). Methodology of sustainable management of the urban heating system in case of massive building renovation. In O. Trofymchuk, & B. Rivza (eds.), *Proceedings of 23rd International Multidisciplinary Scientific GeoConference SGEM 2023*, vol. 23, issue 6.1, (pp. 391–398). Doi.org/10.5593/sgem2023/6.1/s27.49
31. Karnitis, G., Gendelis, S., Pukis, M., et.al. (2023). Simulation of urban heating systems' retrofitting projects: from concept to instrument. In *Proceedings of 24th International Multidisciplinary Scientific GeoConference SGEM 2024* (in print).
32. Cabinet of Ministers Republic of Latvia. (2016). *Regulations Regarding the Energy Efficiency Requirements for Centralized Heating Supply Systems in the Possession of a Licensed or Registered Energy Supply Merchant and the Procedures for Conformity Examination Thereof.* Regulation No. 243, adopted 19 April 2016. Available at: https://faolex.fao.org/docs/pdf/lat172843.pdf
33. Vandenbogaerde, L., Verbeke, S., & Audenaert, A. (2023). Optimizing Building Energy Consumption in Office Buildings: A Review of Building Automation and Control Systems and Factors Influencing Energy Savings. *Journal of Building Engineering*, *76*, 107233. doi.org/10.1016/j.jobe.2023.107233
34. Telia. (2022). *Real Estate Industry Challenges and Digital Solutions*. Available at: https://business.teliacompany.com/internet-of-things/smart-buildings/nordic-and-baltic-real-estate-industry-report
35. Cabinet of Ministers Republic of Latvia (2016). *Building Energy Efficiency Calculation Methods and Building Energy Certification Rules* (in Latvian). Regulation No. 222, adopted 8 April 2021. Available at https://likumi.lv/ta/id/322436-eku-energoefektivitates-aprekina-metodes-un-eku-energosertifikacijas-noteikumi

LATVIAN JOURNAL OF PHYSICS
AND TECHNICAL SCIENCES
2024, N 6

DOI: 10.2478/lpts-2024-0042

SELECTIVE LASER-ASSISTED PATTERNING OF ZNO: EFFECTS OF SYNTHESIS PARAMETERS ON NANOSTRUCTURE MORPHOLOGY

V. Gerbreders*, M. Krasovska, I. Mihailova,
V. Mizers, E. Sledevskis, A. Bulanovs

Daugavpils University,
Institute of Life Sciences and Technology,
1a Parades Str., Daugavpils, LV-5401, LATVIA
*e-mail: vjaceslavs.gerbreders@du.lv

This study explores the laser-induced hydrothermal synthesis of ZnO nanostructures, focusing on the influence of various growth parameters. Using a laser to locally heat the synthesis solution, we achieved controlled growth of ZnO nanostructures. We examined the effects of laser power, exposure time, reagent concentration, and the addition of polyethyleneimine (PEI) on the morphology and distribution of the nanostructures. Results indicate that higher laser powers and extended exposure times lead to increased nanostructure diameters and heights, though they also introduce growth instability. Lower reagent concentrations produce needle-like structures, while higher concentrations yield larger but irregular formations. The addition of PEI accelerates growth, resulting in longer nanorods with reduced height variation but causes a chaotic structural arrangement and the formation of parasitic nanostructures. These findings underscore the critical role of growth parameters in tailoring the properties of ZnO nanostructures for potential applications.

Keywords: *Nanorods, nanostructures, zinc oxide.*

1. INTRODUCTION

Zinc oxide (ZnO) nanostructures are used in a variety of applications due to their unique properties, such as high electron mobility, wide bandgap, and strong room-temperature luminescence [1]. They are extensively used in electronics [2] as transparent conductive oxides for touchscreens [3], LCDs, and thin-film transistors [4]. In photovoltaics, ZnO nanostructures serve as a transparent electrode and active layer in dye-sensitized solar cells [5]–[7]. They are also critical in sensors [8], [9], detecting gases, UV light, and biological substances due to their high sensitivity and fast response. In the biomedical field, ZnO nanostructures are employed for their antibacterial and anticancer properties [10], [11], enabling drug delivery and bioimaging applications. Additionally, they are used in photocatalysis [12] for environmental remediation and in cosmetics for UV protection due to their effective UV absorption capabilities. The key properties of ZnO include a high binding energy of 60 meV, a wide bandgap of about 3.37 eV, excellent thermal and chemical stability, and piezoelectric characteristics, making them versatile for various technological applications [13].

The use of ZnO nanostructures instead of thin films is very popular: nanostructuring of the electrode surface makes it possible to increase the sensitivity of the sensor by increasing the surface area, as well as to chemically activate and functionalize the electrode [14].

Various methods are used to obtain ZnO nanostructures, such as the sol-gel method [15], where a solution system transitions from a liquid “sol” to a solid “gel” phase, forming nanoparticles, nanorods, or nanofibers. Chemical vapour deposition (CVD) [16] involves gaseous precursors reacting on a substrate to deposit ZnO as thin films, nanowires, and nanotubes. The precipitation method [17] entails a chemical reaction in solution that results in ZnO precipitates, which can be collected as nanoparticles. Electrochemical deposition [18], [19] uses an electric field to deposit ZnO onto a substrate, forming nanorods and nanowires. Additionally, microwave-assisted synthesis [20], [21] employs microwave radiation to rapidly produce ZnO nanostructures, and thermal evaporation involves vaporizing ZnO and condensing it to form nanostructures like nanowires and nanobelts.

The hydrothermal method [22], [23] is a widely used technique for synthesizing ZnO nanostructures with diverse morphologies, including nanoparticles, nanorods, nanowires, nanotubes, nanosheets/nanoplates, nanoflowers, nanocubes, and nanostars. The morphology obtained depends on the specific conditions and parameters used in the synthesis process. The key principles of the hydrothermal method involve crystallizing substances from high-temperature aqueous solutions at high vapour pressures.

In the hydrothermal method, precursor materials are first dissolved in water or an appropriate solvent to form a homogeneous solution. This solution is then transferred to an autoclave, a sealed high-pressure vessel, which is heated to a temperature above the boiling point of the solvent, typically ranging from 100 °C to 300 °C or higher. The heating increases the vapour pressure inside the autoclave, creating a high-pressure environment crucial for crystallization.

As the temperature and pressure rise, the solution becomes supersaturated, leading to the nucleation of nanocrystals. The high temperature accelerates reaction kinetics, promoting the growth of nanostructures. Various parameters, such as temperature, pressure, reaction time, concentration of precursors, and the presence of surfactants or additives, can be controlled to tune the morphology of the nanostructures. Surfactants or capping agents can direct the growth into specific shapes.

After the reaction time is completed, the autoclave is cooled to room temperature, and the resulting nanostructures are collected by centrifugation or filtration and washed to remove any unreacted precursors or by-products.

The hydrothermal method offers several advantages, including high purity due to the closed system, which minimises environmental contamination, and the formation of highly crystalline materials. It is versatile, allowing for the synthesis of a wide range of materials, including oxides and sulfides, with precise control over the shape and size of the nanostructures.

Overall, the hydrothermal method is a powerful technique for producing a diverse array of nanostructures with controlled morphologies and desirable properties for various technological applications.

Hydrothermal synthesis is most often used to obtain ZnO nanostructures, but in the general case, using this method, nanostructures grow on the entire surface of the sample. Selective nanostructure patterning is employed in a wide range of advanced technological applications where precise control over material placement and organisation is critical [24], [25]. In electronics, it is used to fabricate high-performance transistors [26], [27], sensors [28], and memory devices, where patterned nanostructures enhance device efficiency and miniaturisation. In photonics, selective patterning enables the creation of photonic crystals and waveguides that manipulate light for applications in optical communication and sensing [29]. In biomedical fields, patterned nanostructures are used to develop biosensors [30], [31] and diagnostic devices [32], [33] with high sensitivity and specificity, as well as in tissue engineering to create scaffolds that mimic the extracellular matrix for improved cell growth and differentiation. Additionally, selective patterning is crucial in energy applications, such as fabricating patterned electrodes [34] for batteries and supercapacitors to improve charge storage and transfer, and in solar cells to enhance light absorption and conversion efficiency [35]. The ability to precisely pattern nanostructures also finds use in environmental monitoring [36], where it aids in the development of highly responsive and selective chemical and gas sensors.

In order to simultaneously obtain coatings of different materials and/or morphologies on the same electrode, methods are needed to synthesize zinc oxide locally and in a controlled manner. Selective patterning of ZnO nanostructures can be achieved through several methods, enabling precise placement and organisation of these nanomaterials on substrates. Photolithography is a common technique where a photoresist is patterned using UV light through a mask, followed by selective growth [37] or deposition of ZnO in the exposed areas. Electron beam lithography [38] offers higher resolution by using focused electron beams to create patterns on an electron-sensitive resist, allowing for fine-scale ZnO nanostructure placement. Soft lithography [39], [40], involving elastomeric stamps, can transfer ZnO patterns onto substrates through microcontact printing or moulding techniques. Another method is inkjet printing [41], [42], which deposits ZnO nanoparticle inks directly onto substrates in defined patterns, providing flexibility and scalability. Additionally, self-assembly techniques [43], [44], such as using block copolymers or templates, can guide the organisation of ZnO nanostructures into specific patterns without the need for external lithographic methods. Each of these techniques offers distinct advantages in terms of resolution, scalability, and complexity of patterns achievable, facilitating the integration of ZnO nanostructures into various electronic, photonic, and sensing applications.

Laser-induced hydrothermal synthesis [45], [46] is an innovative technique that utilises laser irradiation to facilitate the hydrothermal synthesis process, offering advantages such as precise control over nanostructure morphology, reduced reaction times, and improved crystallinity. In this method, a laser beam is focused onto a precursor solution contained in a high-pressure reaction vessel, inducing localised heating and accelerating the hydrothermal reaction. The laser's energy is absorbed by the solution, increasing its temperature and pressure in the irradiated region, leading to nucleation and growth of nanostructures. By controlling parameters such as laser power, irradiation time, and focal spot size, researchers can tailor the size, shape, and distribution of the synthesised nanostructures with high precision. This technique is particularly beneficial for synthesising complex nanostructures such as nanowires, nanorods, and hierarchical architectures. Moreover, the localised heating provided by the laser enables rapid heating and cooling cycles, resulting in shorter reaction times compared to conventional hydrothermal methods. The enhanced crystallinity of the synthesised nanostructures is attributed to the uniform heating and rapid nucleation achieved through laser irradiation. Laser-induced hydrothermal synthesis holds great promise for various applications including catalysis, sensing, energy storage, and biomedical devices, where precise control over nanostructure morphology and properties is crucial for optimising performance.

This publication is devoted to studying the influence of laser-induced synthesis parameters on the morphology of ZnO nanostructures and exploring the possibility of using the resulting coating to create complex-shaped sensors with a selective nanostructured coating.

2. MATERIALS AND METHODS

2.1. Materials

For the synthesis of nanostructures, the following reagents were utilised: zinc nitrate hexahydrate $Zn(NO_3)_2 \cdot 6H_2O$ (CAS#10196-18-6), hexamethylenetetramine (HMTA) $C_6H_{12}N_4$ (CAS# 100-97-0) and branched PEI (CAS#25987-06-8) with purity up to 99 % where purchased from Merck . All morphological samples were prepared on pre-cleaned 76 × 26 mm glass plates and coated with Cr thin layer.

2.2. Process of Synthesis

The fundamental principles underlying the synthesis of ZnO nanostructures rely on chemical reactions occurring in an aqueous solution at elevated temperatures, typically reaching up to 90 °C. Nanostructure growth is facilitated by equimolar solutions of $Zn(NO_3)_2$ and HMTA (hexamethylenetetramine). In this process, zinc nitrate acts as the source of Zn ions, while HMTA creates a mildly alkaline environment. The reactions during this process are represented by the following equations [47], [48]:

$$C_6H_{12}N_4 + 10H_2O \rightleftharpoons 6CH_2O + 4NH_4^+ + 4OH^-; \quad (1)$$

$$Zn^{2+} + 2OH^- \rightleftharpoons Zn(OH)_2 \rightleftharpoons ZnO + H_2O. \quad (2)$$

ZnO nanostructures exhibit distinct anisotropic growth rates across different crystallographic planes (v(0001) > v($10\bar{1}0$) > v($10\bar{1}\bar{1}$) > v($10\bar{1}1$) > v($000\bar{1}$)). Following the principle of energy minimisation, predominant growth occurs along the vertical axis perpendicular to the (0001) plane, resulting in vertically aligned hexagonal nanorods. To achieve hydrothermal synthesis, maintaining a sufficiently high temperature is crucial. Localised hydrothermal synthesis can be achieved by selectively heating the substrate at specific points while keeping the rest of the sample at temperatures insufficient for synthesis. Laser beams are effectively employed for localised heating. When a laser beam is directed onto the sample surface, the material absorbs the energy, converting it into heat. This localised heating raises the temperature of the substrate, transferring stored energy to the surrounding solution volume, creating the necessary temperature for hydrothermal synthesis in that area. The dimensions of the heated point are dictated by the thermal conductivity of the substrate material.

Since the laser beam is localised on a small area, the heating of the substrate occurs at one point, the dimensions of which are determined by the thermal conductivity of the base material.

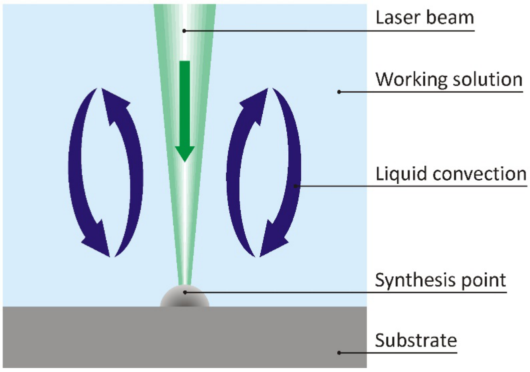

Fig. 1. Schematic illustration of laser-assisted hydrothermal synthesis of nanostructures.

Figure 1 illustrates the process of laser-stimulated hydrothermal synthesis. In this method, a laser heats the synthesis point. As the primary component of the working solution is water, the synthesis medium exhibits favourable thermal conductivity and heat capacity. A focused laser beam with high energy density (up to 10^4 W/cm^2) facilitates vigorous heat exchange among the laser beam, the energy-absorbing substrate, and the surrounding liquid. Consequently, the working solution at the synthesis point reaches the temperature necessary for hydrothermal synthesis. Liquid convection initiates within the heated volume, facilitating both the transport of growth particles and the cooling of the substrate simultaneously, thereby constraining the size of the synthesized spot.

The parameters of the resulting zinc oxide nano/microstructures can be modulated by adjusting various factors such as laser beam exposure time, laser beam power, liquid composition, and reagent concentration. When the laser is integrated into a computer-controlled mechanical system, complex patterns of nanostructures can be created. In this scenario, individual points form lines, and the formation of the pattern is orchestrated by moving the substrate using a mechanised table. The morphology of the resulting nanostructures can also be altered by adding various capping agents. For example, the addition of polyethyleneimine (PEI) promotes an increase in the length of nanorods while decreasing their diameter [49]. PEI is a polar polymer with a large number of pendant ($-NH_2$) amino groups; it protonates in a wide pH range, usually carrying a positive charge, and tends to precipitate on nonpolar, negatively charged ZnO planes. The presence of PEI molecules blocks the growth of ZnO nanostructures along certain planes, contributing to an increase in the length of the nanostructures. In this paper, four different synthesis solutions were investigated, which were given names for convenience. The names and compositions of the solutions are summarised in Table 1.

Table 1. The Employed Solutions and Concentrations of Substances Utilised in the Experiments

Sample name	25 %	100 %	400 %	PEI
Environment	Distilled water			
Zn(CH$_3$CO$_2$)$_2$·2H$_2$O	0.0125 M	0.05 M	0.20 M	0.05 M
(CH$_2$)$_6$N$_4$	0.0125 M	0.05 M	0.20 M	0.05 M
(C$_2$H$_5$N)n	-	-	-	0.20 M

The chosen solutions enable the assessment of the impact of synthesis reagent concentration and the presence of polyethyleneimine on the outcome of laser-stimulated hydrothermal synthesis. Additionally, the influence of zinc oxide seeds on the synthesis of nanostructures was investigated. The seed layer consisted of a 10 nm thick ZnO layer deposited via magnetron sputtering using Kurt J. Lesker equipment. At such thicknesses, magnetron sputtering yields agglomerates of the substance uniformly distributed over the surface, serving as crystallization centres rather than a smooth, homogeneous coating. A specialised apparatus was engineered for laser-stimulated hydrothermal synthesis, providing versatility in irradiating the substrate with a laser beam. The schematic of the equipment is illustrated in Fig. 2.

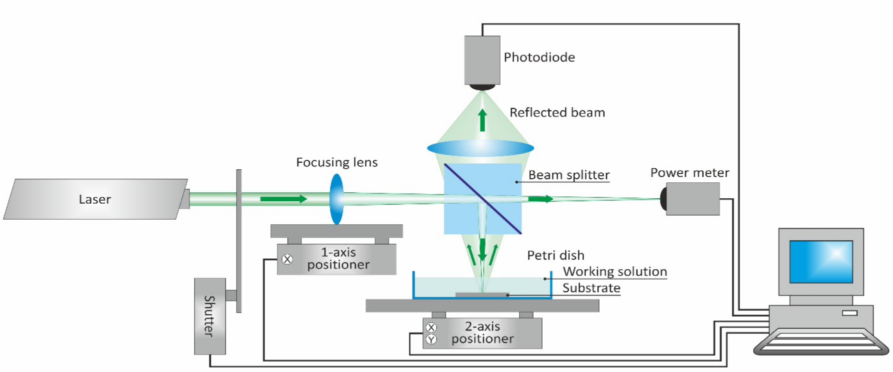

Fig. 2. Schematic representation of the setup for laser-induced hydrothermal synthesis.

The device includes the following components: a Coherent laser Verdi V-6 laser with a 532 nm wavelength and power adjustable from 0 to 3 W, a Standa 8MT177-100XY mechanical platform, an Owis PS35 mechanical platform controller, a Thorlabs SC10 shutter, Ophir optical power meter, a photodiode, a photodiode controller (ST Microelectronics STM32F103C8T6), lenses, and mirrors. The substrate is placed in a working synthesis solution contained in a Petri dish, which is positioned on the mechanical platform to allow for precise movement positioning under the laser beam. The laser beam is modulated by a shutter and focused onto the substrate with a lens. An additional focusing lens on a second mechanical platform allows for adjustment along the beam axis. Lenses with a long focal length (15 cm) are used to ensure the focused beam is nearly plane-parallel, minimising the impact of the transition from air to the solution on focus focal plane. A beam splitter divides the focused beam into two parts: one part goes to a power meter to measure irradiation power, while the other part reflects off the substrate and is focused onto a photodiode. This setup allows for real-time monitoring of the synthesis process and visualisation of the substrate surface, enabling precise selection of the synthesis site – critical for manufacturing multisensors and selectively coating electrode sections with nanostructures. The entire apparatus is controlled by a computer, which manages the mechanical platform's position (and thus the sample synthesis coordinates), modulates the laser beam via the shutter, and measures the reflected light intensity with the photodiode. Adjustments to laser beam power and incident power measurement are were performed manually based on incident power measurement.

The laser-stimulated hydrothermal synthesis process involves a glass substrate with a 160 nm magnetron-sputtered chromium layer in a Petri dish filled with the working synthesis solution (as detailed in Table 1). The bottom of the dish is irradiated with a laser beam. Although the exact diameter of the beam's focal point is not measured, it is assumed to be comparable to the diameter of the synthesised zinc oxide spot. Experiments were conducted by varying the laser beam power, exposure time, and solution composition. The results were analysed using SEM images of the samples (obtained with a Tescan Maya).

3. RESULTS AND DISCUSSION

Figure 3 shows the point and line image obtained at the following parameters: 100 % solution, time – 40 s, incident beam power of 50mW.

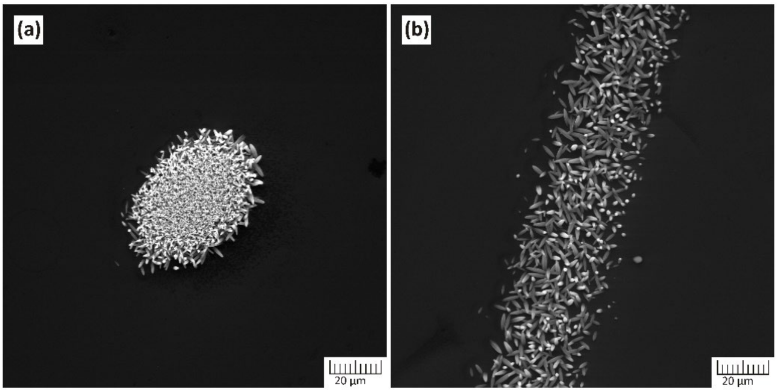

Fig. 3. Example of point and line obtained by laser-induced hydrothermal synthesis.

Since the process of synthesising a line differs from synthesising a point only in how the laser beam moves over the sample during synthesis, this paper focuses on the influence of various growth parameters using point growth as an example. As shown in Fig. 3, both the dot and the line exhibit clear boundaries that distinguish the nanostructured coating from the rest of the sample surface. No growth of zinc oxide structures is observed beyond these boundaries, indicating as a result of a temperature threshold below which synthesis does not occur. The resulting nanostructures are well-ordered and vertically oriented. It is apparent that nanostructures closer to the edge have a significantly larger base diameter. In most cases, structures near the boundary have a larger diameter compared to those at the centre. This can be attributed to the temperature gradient formed during base heating and the uneven supply of reagents, likely due to convection currents. The impact of synthesis time on the resulting nanostructures is illustrated in Fig. 4.

It is evident that a 10-second duration is sufficient for synthesising zinc oxide nano/microstructures. Extending the duration further increases the diameter of the resulting nanostructures. Regardless of the synthesis duration, the nanostructures exhibit excellent vertical alignment perpendicular to the substrate, a behaviour attributed to competitive growth among the nanostructures. The growth process unfolds in distinct stages. Initially, the seeds within the seed layer are densely packed and randomly oriented. Growth along the (0001) plane direction is energetically favoured, and this can be most effectively implemented when the nucleus is initially oriented parallel to this plane on the surface, promoting perpendicular growth. Nanostructures oriented at different angles to the substrate surface inevitably encounter other structures during growth, halting their progress. Consequently, only vertically oriented nanostructures, which are able to grow unhindered, are observed on the sample surface at the conclusion of growth. This process is typical with a dense seed layer. However, in cases where nuclei are less densely distributed or at the edge of a spot where nanostructures do not have neighbouring structures limiting growth and sufficient space allows for lateral growth, the formation of urchin-like structures may occur. This phenomenon is evident in point growth scenarios (Fig. 5), where a vertical array of nanorods is observed at the spot's centre, but a chaotic arrangement is seen at the spot's boundaries, with nanorods positioned at various angles to the seed layer and even structures nearly parallel to the substrate.

Analysis of Fig. 4e reveals that the diameters of the nano/microstructures increase linearly with time, a trend mirrored in the maximum heights of the structures. Additionally, it is apparent that at longer synthesis times, the distribution limits expand, indicating non-uniformity in the synthesis process. Small differences in nanostructure parameters that emerge at the synthesis outset become more pronounced with extended synthesis times.

In Fig. 5, we see a side view of a cluster of nanostructures produced through laser synthesis with an extended irradiation time exceeding 5 minutes. The top row provides a broad view of the islets, while the bottom row offers a more detailed close-up. The illustration shows that over time, the diameter of the island remains almost unchanged, primarily determined by the thermal conductivity of the substrate and the size of the laser irradiation spot. However, a significant change occurs as the duration increases: both the height and diameter of the nanostructures grow substantially. By the 10-minute mark, the outermost nanostructures reach a size of 5 microns, which increases the visual diameter of the island. Interestingly, despite this growth, the nanostructures at the centre of the island maintain their vertical orientation and have a much smaller diameter compared to those at the edges.

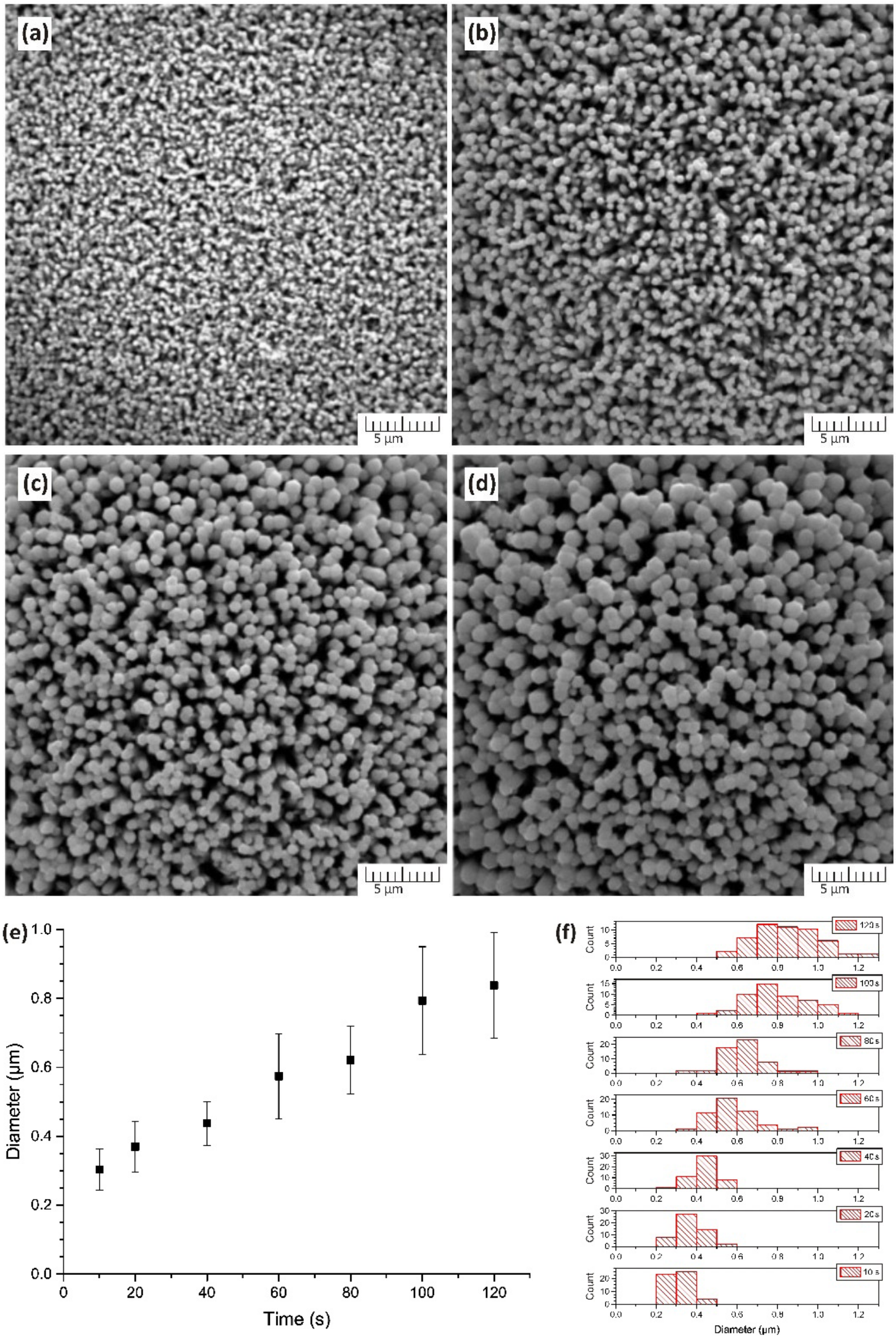

Fig. 4. The effect of synthesis time on the resulting nanostructures. Synthesis was performed in 100 % solution with 50 mW incident laser beam power. Time of synthesis is 10 s (a), 40 s (b), 80 s (c), 120 s (d). The diameters of the synthesised rods depending on the synthesis time. The median of the distribution is marked with a dot on the graph, and the range of the distribution from minimum to maximum diameter is marked with lines (e).

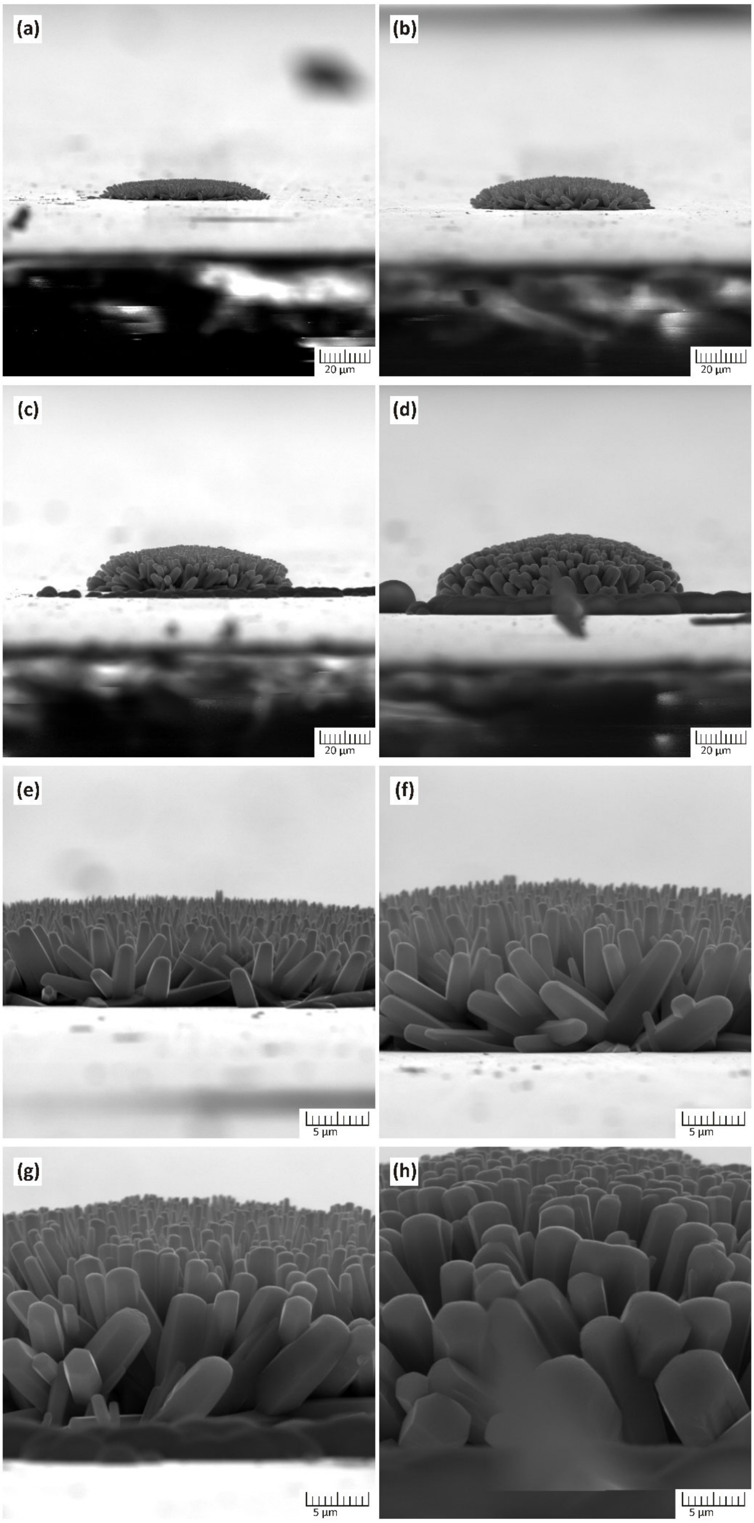

Fig. 5. Influence of long growth times on the synthesis of nanostructures. General view of the island (a–d) and higher magnification (e–h). Synthesis time 5 min (a, e), 10 min (b, f), 20 min (c, g), 60 min (d, h), growth occurred at 50 incident mW laser radiation in 100 % solution.

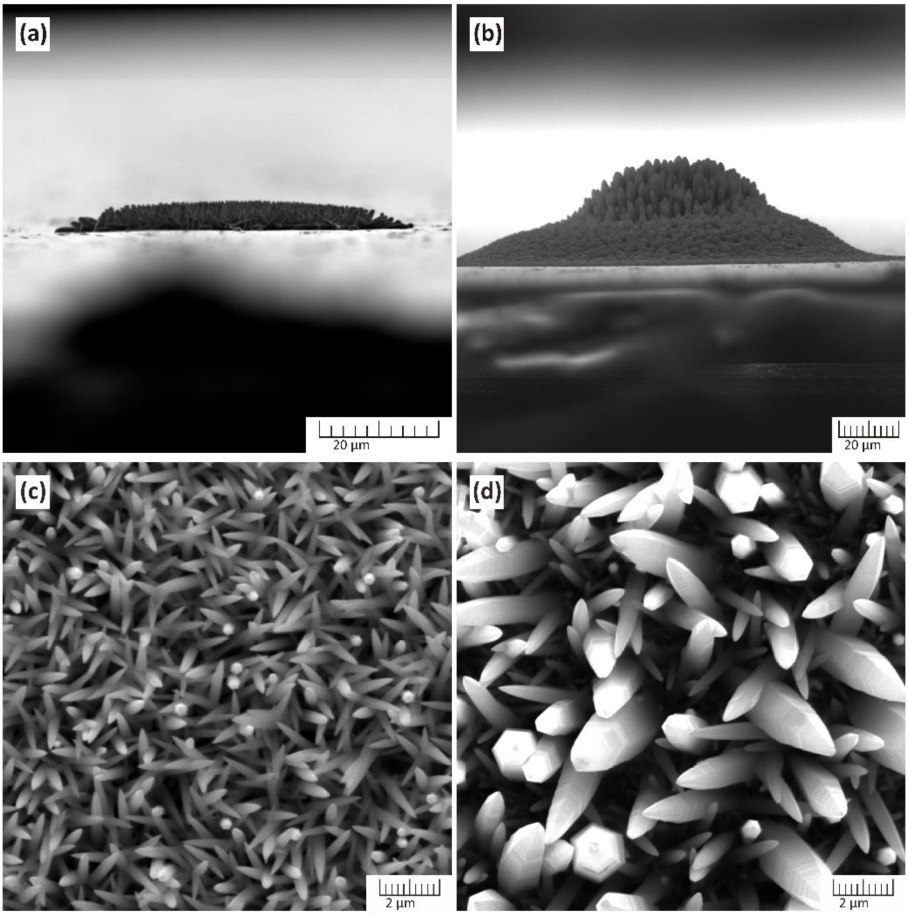

Fig. 6. Dependence of nanostructure parameters on decreased and increased reagent concentration. a) 25 % b) 400 % solution. Growth occurred at 50 mW incident laser radiation in 100 % solution 120 s.

Figure 6 illustrates the relationship between the shape of nanostructures and the concentration of reagents. When the concentration is reduced to one-fourth of the standard (100 % sample), the island's size and the height of the nanostructures remain similar to those observed with the full concentration. However, instead of the characteristic hexagonal prisms of ZnO, needle-like nanostructures form. This deviation is due to the depletion of reagents in the final growth stage, which becomes insufficient to sustain the growth of fully developed nanostructures. As a result, areas of incomplete shape emerge, with diameters decreasing over time due to increasing reagent deficiency, leading to the formation of nanostructures with a pyramidal (or needle-shaped) apex.

Conversely, when the reagent concentration is increased fourfold compared to the standard, an irregularly shaped island forms, consisting of a distinct centre with a diameter identical to that observed with the 100 % concentration and a surrounding halo. As shown in Fig. 6b, the nanostructures in the island's centre exhibit significantly greater height and diameter compared to those in the halo. Furthermore, the nanostructures in the centre are vertically aligned. However, despite this alignment, the nanostructures do not exhibit the characteristic hexagonal prism shape but instead retain the needle-shaped morphology observed with the 25 % solution.

The formation of the island's shape can be explained as follows: at very high reagent concentrations, an intense and simultaneous generation of numerous ZnO nuclei occurs rapidly within the solution. Their rapid deposition at nucleation sites enables the rapid growth of nanostructures several times larger in diameter and height than those obtained from a standard 100 % solution. However, this accelerated deposition of precursor particles impedes the formation of a fully developed hexagonal shape due to insufficient time for surface diffusion, limited by the presence of numerous neighbouring nanoparticles. The precursor particles agglomerate upon contact with the formed nanorod from the solution (a process known as "hit and stick"). The diameter of the region with large-diameter nanostructures is determined by substrate characteristics and the laser beam's diameter. Nonetheless, due to the substrate's thermal conductivity, heating also occurs outside the laser spot. Under normal reagent concentrations, this heat is insufficient to initiate crystallization processes, which are more likely to occur at hotter points. However, if there is a significant surplus of seed particles in the solution, the temperature at the edges becomes adequate to initiate nanostructure formation. Nevertheless, due to the lower temperature compared to the spot's centre, the resulting nanostructures exhibit smaller height and diameter, with height increasing as the distance to the centre decreases.

Figures 7a–c demonstrate that laser-stimulated hydrothermal synthesis at lower powers results in uniform growth over the entire synthesis area, with all structures exhibiting the same height regardless of the synthesis time. In contrast, at higher laser beam powers (Figs. 7d, e), there is a pronounced height variation in the nanostructures: the structures in the middle of the synthesis point are significantly taller than those at the edges. This creates two distinct regions: a central hemispherical area and a surrounding flat ring. The height differences can be attributed to variations in synthesis conditions caused by heat transfer processes. In the central hemisphere, direct laser irradiation ensures a higher temperature. Heat from the base of the laser-irradiated point spreads outward due to thermal conductivity, forming a secondary ring-shaped zone where the temperature is lower, resulting in smaller structures compared to the central area. Although thermal conductivity also occurs at lower powers, it is not as pronounced and does not provide the necessary temperature for synthesis in the secondary zone.

Figure 7g illustrates that increasing the laser beam power can enhance the diameters of the resulting nano/microstructures. However, the increased deviation in the distribution indicates that the synthesis process becomes less stable at higher powers. High incident laser beam powers increase both the synthesis point temperature and the synthesis rate, contributing to the increased deviation.

Interestingly, at 50 mW, the structure diameters are smaller than at lower powers. Below 40 mW, smooth, rounded microstructures with larger base diameters than heights appear instead of the characteristic hexagonal prisms of ZnO nanostructures, indicating lateral growth dominance. Thus, 50 mW can be considered the threshold beyond which the correct shape of nanostructures is possible, with all lower power values being insufficient. Further increasing the power promotes larger diameters of the nanostructures.

Finally, Fig. 8 shows the impact of adding PEI to the synthesis solution on the morphology of the nanostructures.

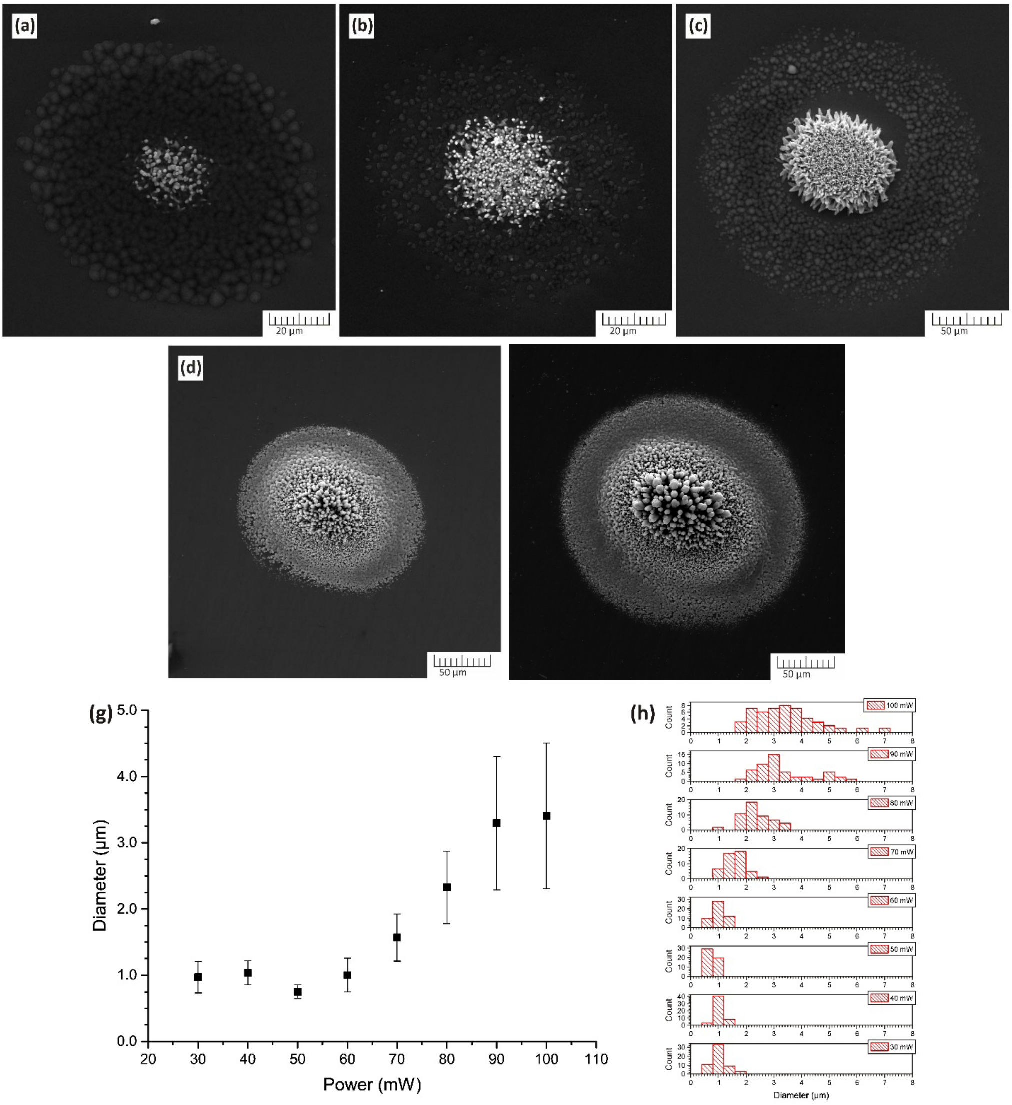

Fig. 7. The effect of incident beam power on the resulting nanostructures. Synthesis was performed in regular solution over 10 min. The incident power is 20 mW (a), 40 mW (b), 60 mW (c), 80 mW (d), 100 mW (e). (f): The diameters of the synthesised rods depending on the incident beam power. The median of the distribution is marked with a dot on the graph, and the range of the distribution from minimum to maximum diameter is marked with lines.

Figure 8a clearly shows that the addition of PEI stimulates the growth rate, resulting in nanorods that are longer than those obtained under similar conditions without PEI. Furthermore, the height difference between nanostructures at the centre of the spot and those in the surrounding area is much smaller with PEI, indicating that its addition reduces the synthesis sensitivity to temperature. Rapid growth also inhibits competitive growth, leading to a chaotic arrangement of nanoneedles in all directions instead of the vertical ordering seen without PEI (Fig. 8b). However, the accelerated synthesis due to PEI also introduces several negative effects. As shown in Fig. 8a, numerous parasitic nanostructures appear outside the main island, blurring the clear boundary of the spot and potentially hindering the formation of well-defined patterns.

Additionally, the rapid growth suppresses competitive growth, resulting in a chaotic rather than vertically ordered arrangement of nanostructures.

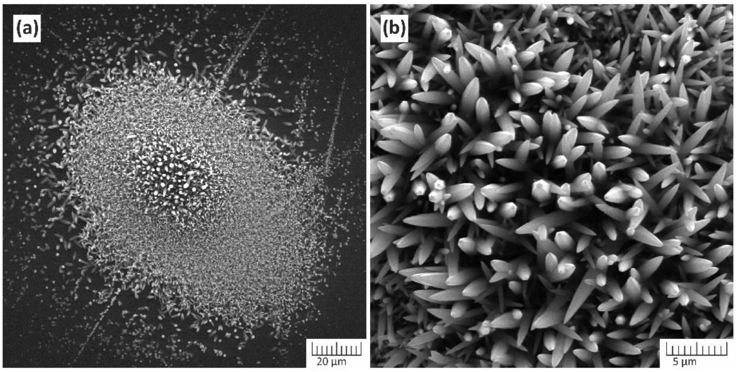

Fig. 8. Effect of PEI on nanostructure morphology. Growth occurred at 50 mW incident laser radiation in 100 % solution 120 s.

4. CONCLUSIONS

The laser-induced hydrothermal synthesis of zinc ZnO nanostructures represents a versatile approach influenced by several critical growth parameters. Experimentally, we observed that adjusting laser power and exposure time significantly impacts the dimensions and stability of the synthesised nanostructures. Higher laser powers and longer exposure times tend to increase both the diameter and height of ZnO nanostructures, albeit with a trade-off of introducing growth instability and uneven height distribution across the synthesis area. Similarly, variations in reagent concentration play a pivotal role in shaping nanostructures, with lower concentrations favouring the formation of needle-like structures and higher concentrations leading to larger but irregularly shaped formations. Polyethyleneimine, when introduced into the synthesis solution, accelerates the growth rate, resulting in longer nanorods and reduced height variations. However, this enhancement comes at the expense of disrupting the vertical alignment of nanostructures, causing them to arrange chaotically and leading to the formation of parasitic nanostructures beyond the intended growth area. Moreover, the substrate's thermal conductivity and the laser beam's focal point critically influence synthesis outcomes, affecting heat distribution and thereby influencing uniform growth. Optimising these parameters is crucial for precisely tailoring the properties of ZnO nanostructures to meet specific application requirements, thereby enhancing their functionality in various technological and biomedical applications.

ACKNOWLEDGEMENTS

This study was supported by DU internal research grant No. 14-95/2024/24 "Development of a Portable Multisensor for the Determination of Polluting Elements in Water".

REFERENCES

1. Agarwal, S., Jangir, L. K., Rathore, K. S., Kumar, M., & Awasthi, K. (2019). Morphology-Dependent Structural and Optical Properties of ZnO Nanostructures. *Applied Physics A, 125* (8)*,* 553. DOI:10.1007/s00339-019-2852-x
2. Zahoor, R., Jalil, A., Ilyas, S. Z., Ahmed, S., & Hassan, A. (2021). Optoelectronic and Solar Cell Applications of ZnO Nanostructures. *Results in Surfaces and Interfaces*, *2*, 100003. DOI:10.1016/j.rsurfi.2021.100003
3. Lin, C. C. (2018). Li-doped ZnO Piezoelectric Sensor for Touchscreen Applications. *International Journal of Electronics and Electrical Engineering*, *6* (4), 53–56. DOI:10.18178/ijeee.6.4.53-56
4. Dahiya, A. S., Sporea, R. A., Poulin-Vittrant, G., & Alquier, D. (2019). Stability Evaluation of ZnO Nanosheet Based Source-Gated Transistors. *Scientific Reports, 9* (1), 2979. DOI:10.1038/s41598-019-39833-8
5. Wibowo, A., Marsudi, M. A., Amal, M. I., Ananda, M. B., Stephanie, R., Ardy, H., & Diguna, L. J. (2020). ZnO Nanostructured Materials for Emerging Solar Cell Applications. *RSC Advances, 10* (70), 42838–42859. DOI:10.1039/d0ra07689a
6. Han, Y., Guo, J., Luo, Q., & Ma, C. (2023). Solution-Processable Zinc Oxide for Printed Photovoltaics: Progress, Challenges, and Prospect. *Advanced Energy & Sustainability Research*, *4*, 2200179. DOI:10.1002/aesr.202200179
7. Manabeng, M., Mwankemwa, B. S., Ocaya, R. O., Motaung, T. E., & Malevu, T. D. (2022). A Review of the Impact of Zinc Oxide Nanostructure Morphology on Perovskite Solar Cell Performance. *Processes*, *10*, 1803. DOI:10.3390/pr10091803
8. Que, M., Lin, C., Sun, J., Chen, L., Sun, X., & Sun, Y. (2021). Progress in ZnO Nanosensors. *Sensors*, *21*, 5502. DOI:10.3390/s21165502
9. Krishna, K. G., Umadevi, G., Parne, S., & Nagaraju Pothukanuri, N. (2023). Zinc Oxide Based Gas Sensors And Their Derivatives: A Critical Review. *Journal of Materials Chemistry C, 11*, 3906–3925. DOI:10.1039/D4SC01030B
10. Mendes, C. R., Dilarri, G., Forsan, C. F., Sapata, V. D. R., Lopes, P. R. M., Bueno de Moraes, P., … & Bidoia, E. D. (2023). Antibacterial Action and Target Mechanisms of Zinc Oxide Nanoparticles against Bacterial Pathogens. *Scientific Reports, 12*, 2658. DOI:10.1038/s41598-022-06657-y
11. Sirelkhatim, A., Mahmud, S., Seeni, A., Kaus, N. H. M., Ann, L. C., Bakhori, S. K. M., … & Mohamad, D. (2015). Review on Zinc Oxide Nanoparticles: Antibacterial Activity and Toxicity Mechanism. *Nano-micro letters*, *7* (3), 219–242. DOI:10.1007/s40820-015-0040-x
12. Sun, Y., Zhang, W., Li, Q., Liu, H., & Wang, X. (2023). Preparations and Applications of Zinc Oxide Based Photocatalytic Materials. *Advanced Sensor and Energy Materials, 2* (3), 100069. DOI:10.1016/j.asems.2023.100069
13. Sharma, D. K., Shukla, S., Sharma, K. K., & Kumar, V. (2020). A Review on ZnO: Fundamental Properties and Applications. *Materials Today: Proceedings*, *49*. 3028–3035. DOI:10.1016/j.matpr.2020.10.238
14. Sauvik Raha, S., & Ahmaruzzaman, Md. (2022). ZnO Nanostructured Materials and their Potential Applications: Progress, Challenges and Perspectives. *Nanoscale Advances, 4*, 1868–1925. DOI:10.1039/D1NA00880C
15. Hasnidawani, J. N., Azlina, H. N., Norita, H., Bonnia, N. N., Ratim, S., & Ali, E. S. (2016). Synthesis of ZnO Nanostructures Using Sol-Gel Method. *Procedia Chemistry, 19,* 211–216. DOI:10.1016/j.proche.2016.03.095
16. Kim, S.-W., Fujita, S., Park, H.-K., Yang, B., Kim, H.-K., & Yoon, D. H. (2006). Growth of ZnO Nanostructures in a Chemical Vapor Deposition Process. *Journal of Crystal Growth, 292* (2), 306–310. DOI:10.1016/j.jcrysgro.2006.04.026

17. Bagheri, S., Chandrappa, K. G., & Hamid, S. B. A. (2013). Facile Synthesis of Nano-Sized ZnO by Direct Precipitation Method. *Der Pharma Chemica, 5* (3), 265–270.
18. Patella, B., Moukri, N., Regalbuto, G., Cipollina, C.,Pace, E., Di Vincenzo, S. … & Inguanta, R. (2022). Electrochemical Synthesis of Zinc Oxide Nanostructures on Flexible Substrate and Application as an Electrochemical Immunoglobulin-G Immunosensor. *Materials*, *15*, 713. DOI:10.3390/ma15030713
19. Manzano, C. V., Philippe, L., & Serrà, A. (2022). Recent Progress in the Electrochemical Deposition of ZnO Nanowires: Synthesis Approaches and Applications. *Critical Reviews in Solid State and Materials Sciences*, *47*(5), p. 772–805. DOI:10.1080/10408436.2021.1989663
20. Wojnarowicz, J., Chudoba, T., & Lojkowski, W. (2020). A Review of Microwave Synthesis of Zinc Oxide Nanomaterials: Reactants, Process Parameters and Morphologies. *Nanomaterials (Basel, Switzerland)*, *10*(6), 1086. DOI:10.3390/nano10061086
21. Ahammed, K. R., Ashaduzzaman, M., Paul, S. C., Nath, M. R., Bhowmik, S., Saha, O., … & Aka, T. D. (2020). Microwave Assisted Synthesis of Zinc Oxide (ZnO) Nanoparticles in a Noble Approach: Utilization for Antibacterial and Photocatalytic Activity. *SN Applied Sciences, 2*(5), 955. DOI:10.1007/s42452-020-2762-8
22. Ejsmont, A., & Goscianska, J. (2023). Hydrothermal Synthesis of ZnO Superstructures with Controlled Morphology via Temperature and pH Optimization. *Materials*, *16 (4)*, 1641. DOI:10.3390/ma16041641
23. Mohan, S., Vellakkat, M., Aravind, A., & U, R. (2020). Hydrothermal Synthesis and Characterization of Zinc Oxide Nanoparticles of Various Shapes under Different Reaction Conditions. *Nano Express, 1* (3), 030028. DOI:10.1088/2632-959X/abc813
24. Barad, H.-N., Kwon, H., Alarcón-Correa, M., & Fischer, P. (2021). Large Area Patterning of Nanoparticles and Nanostructures: Current Status and Future Prospects. *ACS Nano, 15* (4)*,* 5861–5875. DOI:10.1021/acsnano.0c09999
25. Mihailova, I., Krasovska, M., Sledevskis, E., Gerbreders, V., Mizers, V, … & Ogurcovs, A.(2023). Selective Patterned Growth of ZnO Nanoneedle Arrays. *Latvian Journal of Physics and Technical Sciences, 60* (6), 35–53. DOI:10.2478/lpts-2023-0035
26. Shaw, J. E., Stavrinou, P. N., & Anthopoulos, T. D. (2012). On-Demand Patterning of Nanostructured Pentacene Transistors by Scanning Thermal Lithography. *Advanced Materials, 25* (4), 552–558. DOI:10.1002/adma.201202877
27. Demontis, V., Zannier, V., Sorba, L., & Rossella, F. (2021). Surface Nano-Patterning for the Bottom-Up Growth of III-V Semiconductor Nanowire Ordered Arrays. *Nanomaterials, 11*, 2079. DOI:10.3390/nano11082079
28. Wang, H., Jiménez-Calvo, P., Hepp, M., Isaacs, M. A., Ogolla, C. O., Below-Lutz, I., … & Strauss, V. (2023). Laser-Patterned Porous Carbon/ZnO Nanostructure Composites for Selective Room-Temperature Sensing of Volatile Organic Compounds. *ACS Applied Nano Materials, 6* (2), 966–975. DOI:10.1021/acsanm.2c04348
29. Chen, K., Thang, D. D., Ishii, S., Sugavaneshwa, R. P., & Nagao, T. (2015). Selective Patterned Growth of ZnO Nanowires/Nanosheets and their Photoluminescence Properties. *Optical Materials Express, 5* (2)*,* 353. doi:10.1364/ome.5.000353
30. Tereshchenko, A., Bechelany, M., Viter, R., Khranovskyy, V., Smyntyna, V., Starodub, N., & Yakimova, R. (2016). Optical Biosensors Based on ZnO Nanostructures: Advantages and Perspectives. A review. *Sensors and Actuators B: Chemical, 229,* 664–677. doi:10.1016/j.snb.2016.01.099
31. Sharma, A., Agrawal, A., Kumar, S., Awasthi, K. K., Awasthi , K., & Awasthi, A. (2021). Zinc Oxide Nanostructures–Based Biosensors. *Nanostructured Zinc Oxide, Elsevier,* 665–695. DOI:10.1016/B978-0-12-818900-9

32. Kim, S., Kim, G. H., Woo, H., An, T., & Lim, G. (2019). Fabrication of a Novel Nanofluidic Device Featuring ZnO Nanochannels. *ACS Omega, 5* (7), 3144–3150. DOI:10.1021/acsomega.9b02524
33. Krishna, S. B. N., Jakmunee, J., Mishra, Y. K., & Jai Prakash, J. (2024). ZnO Based 0–3D Diverse Nano-Architectures, Films and Coatings for Biomedical Applications. *Journal of Materials Chemistry B, 12,* 2950–2984. DOI:10.1039/D4TB00184B
34. Anang, F. E. B., Wei, X., Xu, J., Cain, M., Li, Z., Brand, U., & Peiner, E. (2024). Area-Selective Growth of Zinc Oxide Nanowire Arrays for Piezoelectric Energy Harvesting. *Micromachines*, *15*, 261. DOI:10.3390/mi15020261
35. Zheng, Z., Lim, Z., Peng, Y., You, L., Chen, L., & Wanf, J. (2013). General Route to ZnO Nanorod Arrays on Conducting Substrates via Galvanic-Cell-Based Approach. *Scientific Reports, 3*, 2434 DOI:10.1038/srep02434
36. Gerbreders, V., Krasovska, M., Mihailova, I., Ogurcovs, A., Sledevskis, E., Gerbreders, A., … & Plaksenkova, I. (2021). Nanostructure-Based Electrochemical Sensor: Glyphosate Detection and the Analysis of Genetic Changes in Rye DNA. *Surfaces and Interfaces, 26,* 101332. DOI:10.1016/j.surfin.2021.101332
37. Ferreira, S. H., Cunha, I., Pinto, J. V., Neto, J. P., Pereira, L., Fortunato, E., & Martins, R. (2021). UV-Responsive Screen-Printed Porous ZnO Nanostructures on Office Paper for Sustainable and Foldable Electronics. *Chemosensors*, *9*, 192. DOI:10.3390/chemosensors9080192
38. Papageorgiou, G. P., Karydas, A. G., Papageorgiou, G., Kantarelou, V., & Makarona, E. (2020). Controlled Synthesis of Periodic Arrays of ZnO Nanostructures Combining E-Beam Lithography and Solution-Based Processes Leveraged by Micro X-ray Fluorescence Spectroscopy. *Micro and Nano Engineering, 8,* 100063. DOI:10.1016/j.mne.2020.100063
39. Chen, B., Lu, K., & Ramsburg, K. (2012). ZnO Submicrometer Rod Array by Soft Lithographic Micromolding with High Solid Loading Nanoparticle Suspension. *Journal of the American Ceramic Society, 96* (1), 73–79. DOI:10.1111/jace.12069
40. Tredici, I. G., Resmini, A., Yaghmaie, F., Irving, M., Maglia, F., & Anselmi-Tamburini, U. (2012). A Simple Two-Step Solution Chemistry Method for Synthesis of Micropatterned ZnO Nanorods Based on Metal-Loaded Hydrogels. *Thin Solid Films, 526,* 22–27. DOI:10.1016/j.tsf.2012.10.052
41. Lee, H., Harden-Chaters, W., Han, S. D., Zhan, S., Li, B., Bang, S. Y., … & Kim, J. M. (2020). Nano-to-Micro porous Networks via Inkjet Printing of ZnO Nanoparticles / Graphene hybrid for Ultraviolet Photodetectors. *ACS Applied Nano Materials, 3,* 4454–4464. DOI:10.1021/acsanm.0c00558
42. Fajardo, J., Garduno, S. I., & Estrada, M. (2020). Analysis of inkjet printing conditions for ZnO nanoparticles patterns towards the fabrication of fully printed thin film devices. In *2020 IEEE Latin America Electron Devices Conference (LAEDC)*, 25–28 February 2020*,* San José, Costa Rica. DOI:10.1109/laedc49063.2020.9073472
43. López-Miranda, J. L., Sánchez B. L. E., Esparza, R., & Estévez, M. (2022). Self-Assembly of ZnO Nanoflowers Synthesized by a Green Approach with Enhanced Catalytic, and Antibacterial Properties. *Materials Chemistry and Physics, 289*, 126453. DOI:10.1016/j.matchemphys.2022.126453
44. Chiu, W. S., Yaghoubi, A., Chia, M. Y., Khanis, N. H., Rahman, S. A., Khiew, P. S., & Chueh, Y.-L. (2014). Self-Assembly And Secondary Nucleation in ZnO Nanostructures Derived from a Lipophilic Precursor. *CrystEngComm, 16* (27), 6003–6009. DOI:10.1039/c4ce00442f
45. Fujiwara, H., Suzuki, T., Niyuki, R., & Sasaki, K. (2016). ZnO Nanorod Array Random Lasers Fabricated by a Laser-Induced Hydrothermal Synthesis. *New Journal of Physics, 18* (10), 103046. DOI:10.1088/1367-2630/18/10/103046

46. Rajab, F. H., Taha, R. M., Hadi, A. A., Khashan, K. S., & Mahdi, R. O. (2023). Laser Induced Hydrothermal Growth of ZnO Rods for UV Detector Application. *Optical and Quantum Electronics, 55,* 208. https://doi.org/10.1007/s11082-022-04473-2
47. Georgiou, P., Kolokotronis, K., & Simitzis, J. (2009). Synthesis of ZnO Nanostructures by Hydrothermal Method. *Journal of Nano Research, 6,* 157–168. DOI:10.4028/www.scientific.net/jnanor.6.157
48. Krasovska, M., Gerbreders, V., Sledevskis, E., Gerbreders, A., Mihailova, I., Tamanis, E., & Ogurcovs, A. (2020). Hydrothermal Synthesis of ZnO Nanostructures with Controllable Morphology Change. *CrystEngComm., 22* (8), 1346–1358. DOI:10.1039/c9ce01556f
49. Alavi, S. J., Khalili, N., Kazemi Oskuee, R., Verma, K. D., & Darroudi, M. (2015). Role of Polyethyleneimine (PEI) in Synthesis of Zinc Oxide Nanoparticles and their Cytotoxicity Effects. *Ceramics International, 41* (8), 10222–10226. DOI:10.1016/j.ceramint.2015.04.129

LATVIAN JOURNAL OF PHYSICS
AND TECHNICAL SCIENCES
2024, N 6

DOI: 10.2478/lpts-2024-0043

NOVEL APPROACH TO MAKING ENVIRONMENTALLY FRIENDLY PLASTER: A MOISTURE BUFFER VALUE OF PLASTER MADE OF WASTEPAPER AND DIFFERENT GLUES

N. Nutt, L. Nei*, H. Muoni, A. Kubjas and J. Raamets

Tallinn University of Technology,
School of Engineering, Tartu College,
Puistee 78, 51007 Tartu, ESTONIA
*e-mail: lembit.nei@taltech.ee

This article deals with the reuse of wastepaper. Three components were used to make traditional paper plaster: wastepaper, glue, and water. Whether the glues used to make paper plaster and the quantities of those glues have an impact on the moisture buffering value (MBV) of paper plaster was studied. The scope of the Nordtest method is to evaluate the MBV for materials exposed to indoor air. The test intended to simulate daily variations with relative humidity between 75 % during 8 hours and 33 % during 16 hours.

The test specimen was made according to the recipe which contained the following: wastepaper (newspaper paper), three different types of glue (potato starch (*Amylum Solani*) $C_6H_{10}O_5$, wallpaper glue Metylan Universal Premium (produced by Henkel), and methylcellulose $C_6H_7O_2(OH)_x(OCH_3)_y$, and water. Different percentages of glue were used in the specimens. Potato starch (*Amylum Solani*) $C_6H_{10}O_5$ clearly increased the moisture buffering ability.

The tests performed showed that the composition and quantity of glue affected the MBV of paper plaster. The MBV of all the specimens remained in the range of 2.08–2.48 [g/(m^2·%RH)@8/16h]. The largest MBV was 2.48[g/(m^2·%RH)@8/16h], and it was registered in the case of a mixture that had a glue made from 100 g of potato starch (*Amylum Solani*) $C_6H_{10}O_5$ per litre of water and the smallest MBV was 2.08[g/(m^2·%RH)@8/16h], and it contained glue mixture made of 20 g methylcellulose per litre of water. As a result of the current study, an environmentally friendly plaster with high moisture buffer value using wastepaper as a component of this material was developed.

Keywords: *Buffer property, circular economy, MBV, mould, Nordtest, plaster material, recycle.*

1. INTRODUCTION

Moisture buffering materials for indoors finishing are receiving increasing attention for their ability to regulate room humidity passively. It is important to study the ability of their moisture-buffering performance because this indicator is highly material dependent [1]. The application of moisture-buffering materials in the room reduces the amplitude of indoor relative humidity [2]. The fluctuation of relative humidity could be minimised noticeably when utilising hygroscopic materials and it is realistic to lower the total energy consumption by up to 25 % [3]. The moisture buffering value (MBV) can be further improved by increasing the moisture capacity of the material. It has been shown that the nature of the clay minerals has a great influence on the moisture capacity [4]. Still, lime-cement plasters, which are widely utilised as indoor finishing materials, perform "good" but still do not demonstrate "excellent" moisture buffering abilities [5].

The building industry is among the biggest consumers of natural resources, and this sector is considered to cause a great environmental impact [6]. The growing demand for natural resources and intensive industrial production is catalysing the construction sector to search for novel environmentally friendly materials [7]. The circular economy has been successfully applied for manufacturing several paper products such as profile rails and packaging accessories (boxes, slats, corners, and grates) [8]. Paper has been used for a long time in the decoration of interiors, for example, wallpaper. Previous laboratory studies confirm that paper plaster made of wastepaper has an MBV classified as "excellent" [9], [10]. The impact of adding paper to clay plaster mixtures [11], [12] and the effect of different technologies on the MBV used to make paper plaster [13], [14] have also been studied. Making paper plaster creates a large quantity of wastewater, whose components and environmental hazards have been studied by Allikvee [15]. Using paper waste in making plaster mortar is not only useful for the environment by helping to reduce the pollution but is also cost-effective [16].

This paper focuses on wastepaper as a resource that enables the decrease of greenhouse gas emissions in the manufacturing sector when reused, and the reuse of waste, in turn, helps lower the costs of waste management. Applying paper plaster does not require specific skills unlike the application of clay plaster, making it executable by anyone [11]. The aim of the research presented in this article was to develop an environmentally friendly plaster with a high moisture buffer value, using wastepaper as a component of this material.

2. MATERIALS AND METHODS

2.1. Method

The Nordtest method, which enables the determination of the MBV of composite systems (plaster mixtures) exposed to indoor climate, was used to study plaster mixtures. The method suggests that the study material is placed in a closed system where round-the-clock changes in the relative humidity of the living space are simulated.

The method used in this study has been detailed by Rode [17]. A partly sealed sample was exposed to repetitive changes in ambient relative humidity (RH), with the temperature held constant at 23 °C. The change in RH resulted in the specimen gaining or losing weight, and this change was determined through continuous monitoring or frequent weighting. The change in weight over a specific time could be considered an indication of the MBV of the test specimen.

A climate chamber was included in the experiment. In this chamber, the temperature and RH could be maintained at a constant level, and the required RH could be achieved. Additionally, suitable sensors and a logging system were used to continuously record the temperature and relative humidity within the test chamber. An analytical balance, capable of weighing the test specimens with the repeatability of 1 %, was also employed. The air in the test chamber circulated and the air velocity, typical of an indoor environment, was 0.10±0.05 m s^{-1}.

The rest specimen shape and size were not fixed. The recommended minimum side length or diameter of the exposed area of the specimen was 100 mm, and the minimum exposed face area was 0.01 m^2. The area was set within an accuracy of 1 %. If the total surface area was homogeneous and at least 0.03 m^2, then representative smaller test specimens were allowed. The test specimens were sealed on n-1 out of n. The materials used for sealing did not absorb moisture.

The thickness of the samples was the same as their intended use or as the depth of moisture penetration (1 % definition) for daily variations in moisture. Official guidelines for typical construction of the material determined the maximum thickness of the material. At least three test specimens were tested.

At first (before testing) the specimens were stored and kept in equilibrium with air at 23±5 °C and RH at 50 ± 5 %. The criterion for the equilibrium was defined as a period that was long enough for the weight of the specimen to stabilise to a state where two successive daily determinations (24 h in between) of the weight stayed within 0.1 % of the sample mass.

Test conditions: the temperature at 23 °C, low RH of 33 %, high RH of 75 %. The high level of RH lasted for 8 hours (±10 min) and the low RH level for 16 hours (±10 min). If the RH changes were not achieved instantaneously, then they were measured to an accuracy of ±3 % RH within a maximum of 30 min after the intended change. The temperature was within ± 0.5 °C.

The cyclic exposure was carried out until the mass changes. During the last three cycles (days) the change in mass, Δm [g], was less than 5 %. Δm was determined in each cycle as the average between the weight gain during the moisture uptake branch of the cycle and the weight loss during drying. Also, the difference between weight gain and weight loss within each cycle was less than 5 % of Δm.

The weight gains and losses were continuously monitored, and a minimum of one weighting was completed by the turn of each exposure in the cycle. During an 8-hour absorption period of the final three days, the sample was weighed a minimum of five times. The preparation of the specimen and the test facility: the test samples were prepared, their thickness and the exposed area were measured before and after sealing. The procedure was tested, and then the weighing was performed. The weighing was performed in an environment, set to a temperature within ±2 °C of the test condition, anywhere within the test chamber. The result was not influenced by the movement to scale by more than 1 % of the amplitude. A curve of the mass in time was plotted.

2.2. Material

The components of the paper plaster mixture and their ratio in the mixture were crucial when making paper plaster. These conditions restricted putting together the recipe necessary for the experiment. All the specimens were made of the same type of waste paper, which was newspaper paper. Adhesives were chosen based on the glues recommended in the paper plaster literature [18], [19]. They included potato starch (*Amylum Solani*) $C_6H_{10}O_5$, methylcellulose $C_6H_7O_2(OH)_x(OCH_3)_y$, and industrially made wallpaper glue based on methylcellulose (Metylan Universal Premium, produced by Henkel). Firstly, when choosing the concentration of the adhesive for the paper plaster, it was kept in mind that the consistency of the plaster had to be suitable for applying to the wall. The consistency could not be too runny (indicating too much glue) or too dry (indicating not enough glue). When the amount of glue is too high, the plaster becomes a slippery liquid mass, which is difficult to apply, and when the amount of glue is too small, the plaster is brittle and does not stick to the wall. Secondly, when making the glue mixtures, the consistency of the final mixture needed to be kept in mind. The thickness of the paste boiled with potato starch (*Amylum Solani*) $C_6H_{10}O_5$ determined the upper limit of the potato starch concentration. A paste made with too much glue becomes lumpy and cannot be evenly mixed into the paper plaster mixture, affecting the texture of plaster's surface. The surface is uniform and smooth when the amount of glue is small. As the quantity of glue increases, the surface becomes more and more uneven.

The lower concentration limit for the potato starch (*Amylum Solani*) $C_6H_{10}O_5$ was 20 g of dry matter per litre of water, and the upper concentration limit was 100 g of dry matter per litre of water. For methylcellulose ($C_6H_7O_2(OH)_x(OCH_3)_y$) the limits were accordingly 5 g and 20 g of dry matter per litre of water, and for wallpaper glue Metylan Universal Premium, they were 20 g and 30 g of dry matter per litre of water.

The specimens were made according to the recipe that contained the following: waste paper (newspaper paper), glue (two different, methylcellulose or starch), and water. The total number of specimens was 24. Different percentages of glue and three types of glue (potato starch (*Amylum Solani*) $C_6H_{10}O_5$, methylcellulose (by Henkel), and methylcellulose $C_6H_7O_2(OH)_x(OCH_3)_y$) were used in the specimens, with a diameter of approx. 90 mm and a thickness of 25 mm. The amount of glue was as follows: 20 g, 50 g, 100 g of potato starch $C_6H_{10}O_5$ (Amylum Solani) glue per litre of water, and 20 g, 30 g of methylcellulose glue with antifungal additives (Metylan Universal Premium)) per litre of water^{-1}, and 5 g, 10 g, 20 g of methylcellulose glue per litre of water^{-1} and 500 g paper (soaked in water) (Table 1).

To calculate the MBV, it was necessary to know the area of one side of the specimen. An important parameter that characterises paper plaster is the loss of volume during the drying process. As a result, the specimens made of paper plaster deform when they dry, and, therefore, traditional measuring tools (ruler, calliper) were not used. Scanning was used to measure the areas of the specimens with irregular shapes. The specimens were prepared for the experiment, which entailed placing them at first in a nitrile pouch in a way that left their top surface open. The specimens were numbered and placed in the scanner. The number of pixels from scanned image files (.jpg) of specimens areas was measured with the help of Adobe Photoshop Measurement features and converted into area units (cm^2), which were used for calculating the MBV.

A digital scale Kern PLT 1200-3A (accuracy of 0.001 g) was used to weigh the specimens. After autosave, the data was converted and imported into a data collection system, which checked if the prerequisites necessary to calculate the MBV had been fulfilled. When the requirements were met, the data collection system calculated the MBV, and the experiment was finished.

In order to analyse the data, statistical programme languages Python and R, and the database system PostgreSQL were used.

The climate chamber method was used with the environmental temperature set at 23±0.5 °C with three specimens of each type. The equipment included the RUMED 4101 climate chamber, which provided RH 20...95 % with an accuracy of ±2-3 % and a temperature range of 0±60 °C with an accuracy of ±0.5 °C.

Table 1. Composition of the Mixture: Paper Type – Newspaper; Paper Weight – 500 g

Mixture code	Glue water (g l^{-1})	Glue type	Notes
A-T100	100	potato starch	*Amylum Solani* $C_6H_{10}O_5$
A-T50	50	potato starch	*Amylum Solani* $C_6H_{10}O_5$
A-T20	20	potato starch	*Amylum Solani* $C_6H_{10}O_5$
A-H30	30	Metylan Universal Premium	modified starch
A-H20	20	Metylan Universal Premium	chemically introduced antifungal additives
A-M20	20	methylcellulose	$C_6H_7O_2(OH)_x(OCH_3)_y$
A-M10	10	methylcellulose	$C_6H_7O_2(OH)_x(OCH_3)_y$
A-M5	5	methylcellulose	$C_6H_7O_2(OH)_x(OCH_3)_y$
A	-	-	-

3. RESULTS AND DISCUSSION

To compare the moisture absorption and desorption of plaster mixtures studied in the test, an index for MBV was used. $MBV_{practical}$ describes the changes in the moisture of materials in real situations in spaces related to people [20].

In the Nordtest experiment carried out to determine the MBV, the relative humidity was cyclically changed (8 h with RH=75 % and 16 h with RH=33 %). As a result of cyclical changes in relative humidity of the climate chamber, the specimens' weight also changed in cycles.

The results were calculated as changes in mass: Δm per m^2 and ΔRH. For each cycle, two results of mass change were calculated: one for the weight gain during absorption (m8 hours – m0) and one for the weight loss during drying (m24 hours – m8 hours). In each cycle, the average between the absorption and desorption weight changes was calculated. Based on the average of at least three, the MBV was calculated.

The Nordtest protocol formula for $MBV_{practical}$ [g $(m^2\cdot\%RH)^{-1}$] calculations (Equation 1):

$$MVB_{8h} = \frac{m_{max} - m_{min}}{A\cdot(\varphi_{high} - \varphi_{low})}, \quad (1)$$

where $m_{min/max}$ is moisture mass (min and max) in the final sample (g or kg); A – exposed area m^2; $\varphi_{high/low}$ – high/low RH (-) levels applied in the measurement.

When using the moisture buffer values [g $(m^2\cdot\%RH)^{-1}$@8 $16h^{-1}$], materials can be classified as follows: negligible (0–0.2), limited (0.2–0.5), moderate (0.5–1.0), good (1.0–2.0), and excellent (2.0 and more). To determine the MBV, the Nordtest experiment was conducted. Changes in specimens' moisture (g) were measured when specimens were kept at RH=75 % for 8 hours and at RH=33 % for 16 hours. During one cycle, at least five weightings were carried out following the Nordtest method. However, the climate chamber RUMED 4101 was used for the experiment, which did not enable the weighing of the specimens inside the chamber, and they had to be taken out for each weighing. Consequently, the original method was altered, reducing the number of weightings to two. The specimens were weighed before changing the humidity in the chamber, which was carried out every 8 and 16 hours. This minimised the loss of moisture when removing the specimens from the chamber (humidity in the weighing room was lower than in the climate chamber). To validate the results, the same experiment with five weightings was also conducted to observe the change effects on the MBV. The control test showed that the MBV was consistent in both experiments. However, the experiment with five weightings extended the length of the experiment from 72 hours to 127 hours due to a prolonged stabilisation period.

The results of the study demonstrate that specimens with the same components responded similarly to the cyclic changes in the humidity of the environments (see Fig. 1). Table 2 displays the mean H_2O weight changes (%) of paper plaster mixture A-T20 (potato starch (*Amylum Solani*) $C_6H_{10}O_5$ in 1 l of water) specimens during the final three cycles of Nordtest. Based on this data, the moisture buffering ability of the material was calculated.

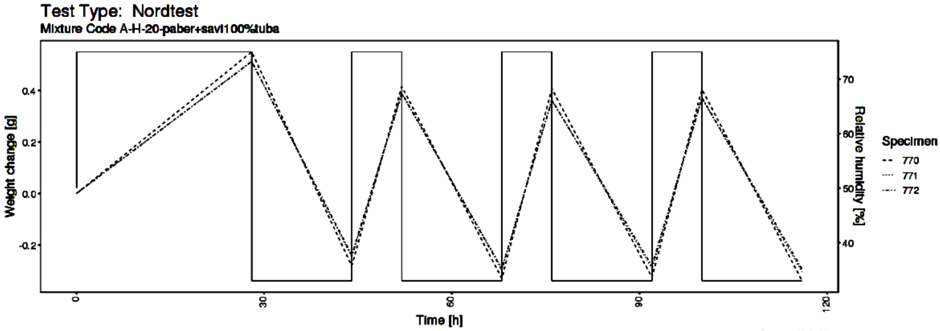

Source: Nele Nutt

Fig. 1. Paper plaster mixture A-T20. 20 g of glue (potato starch (*Amylum Solani*) $C_6H_{10}O_5$) per litre of water. Changes in specimens' weight (only weight change) in the final three cycles of Nordtest. A continuous line portrays the change in moisture cycles (RH 33 % and RH 75 %) in the climate chamber.

All the paper plaster mixtures tested in the experiment had MBV > 2.0 [g $(m^2 \cdot \%RH)^{-1}$@8 16h^{-1}], which signifies that all the tested mixtures can be classified as "excellent" (Table 3). The test results showed that the amount of glue used in the mixture affected the MBV. The results indicate that a larger quantity of glue decreased only the MBV of the specimens made of wallpaper glue. However, for other glues, the change was the opposite. A higher amount of glue increased the MBV of both potato starch and methylcellulose paper plasters. If compared with the results for lime-cement and clay-based plasters, presented in [5] and in [21], which correspond to "good", the MBV values given in Table 3 clearly correspond better to the desired properties – "excellent" – set for plasters used indoors.

Table 2. Paper Plaster Mixture A-T20 (20 g of glue (potato starch (*Amylum Solani*) $C_6H_{10}O_5$ per litre of water^{-1}) (Changes in specimens' mean H_2O weight and weight change (%) in the final three cycles of Nordtest.)

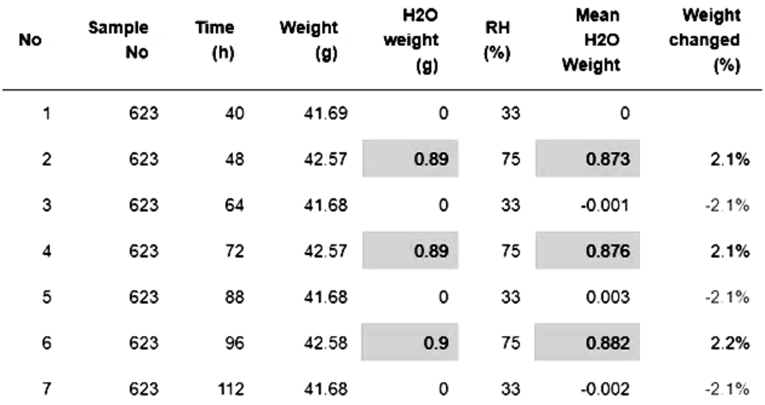

No	Sample No	Time (h)	Weight (g)	H2O weight (g)	RH (%)	Mean H2O Weight	Weight changed (%)
1	623	40	41.69	0	33	0	
2	623	48	42.57	0.89	75	0.873	2.1%
3	623	64	41.68	0	33	-0.001	-2.1%
4	623	72	42.57	0.89	75	0.876	2.1%
5	623	88	41.68	0	33	0.003	-2.1%
6	623	96	42.58	0.9	75	0.882	2.2%
7	623	112	41.68	0	33	-0.002	-2.1%

Table 3. MBVs of Paper Plaster Mixtures

Mixture code	MBV [g $(m^2\cdot\%RH)^{-1}$@8 16h^{-1}]	MBV classification
A-T100	2.48	excellent*
A-T50	2.35	excellent*
A-T20	2.31	excellent*
A-H30	2.36	excellent*
A-H20	2.33	excellent*
A-M20	2.08	excellent*
A-M10	2.15	excellent*
A-M5	2.39	excellent*

*negligible (0–0.2), limited (0.2–0.5), moderate (0.5–1.0), good (1.0–2.0), excellent (2.0–).

Previous experiments have shown that in order to dissolve 500 g of waste paper, it is necessary to add 5 l of water and, after soaking, drain 3 l of water. This way, 500 g of paper turn into 2500 g mixture, which has a suitable consistency for applying on the wall. The glue mixture needs to be added before use. Literary sources [18]–[22] recommend adding glue during the soaking process. However, it is most reliable to add the adhesive after draining as the final component because then the amount of glue used is the smallest (adding glue to soaking water means that part of the glue mixture is also drained as wastewater). The adhesive is the most expensive component of paper plaster and affects the price of paper plaster the most. The most expensive glue used in the experiment was methylcellulose ($C_6H_7O_2(OH)_x(OCH_3)_y$), which costs 40.00 EUR kg^{-1}. The wallpaper glue Metylan Universal Premium is more than half the price. Potato starch (*Amylum Solani*) $C_6H_{10}O_5$, in turn, is *ca* twenty times cheaper.

1. The specimens reacted to the change in humidity (RH of 33 %–RH of 75 %) very similarly.
2. Paper plaster is a material with excellent moisture buffering ability. All the mixtures' moisture buffering abilities used in the experiment remained in a specific range (2.08–2.48 [g $(m^2\cdot\%RH)^{-1}$ @8 16h^{-1}]) and belonged to the highest-rated group – "excellent" (MBV > 2.0 [g $(m^2\cdot\%RH)^{-1}$@8 16h^{-1}]).

3. The moisture buffering ability is affected by the composition and amount of glue used in the mixture.
4. The **MBV increased** when the amount of glue, such as potato starch (*Amylum Solani*) $C_6H_{10}O_5$ and the product Metylan Universal Premium by Henkel, was increased in the mixture. When the amount of potato starch (*Amylum Solani*) $C_6H_{10}O_5$ was increased from 20 g to 100 g, the MBV rose from 2.31 to 2.48 [g $(m^2 \cdot \%RH)^{-1}$@8 16h^{-1}], and the Henkel product Metylan Universal Premium from 20 g to 30 g made the MBV rise from 2.33 to 2.36 [g $(m^2 \cdot \%RH)^{-1}$ @8 16h^{-1}].
5. Increasing the quantity of methylcellulose ($C_6H_7O_2(OH)_x(OCH_3)_y$) from 5 g to 20 g **decreased the MBV** from 2.39 to 2.08 [g $(m^2 \cdot \%RH)^{-1}$@8 16h^{-1}].
6. Out of all the three adhesives, the potato starch (*Amylum Solani*) $C_6H_{10}O_5$ increased the moisture buffering ability the most when it had the largest quantity of dry matter in the mixture (100 g per litre of water^{-1}). Paper plaster that had the most substantial quantity of methylcellulose ($C_6H_7O_2(OH)_x(OCH_3)_y$) (20 g per litre of water^{-1}) had the lowest moisture buffering ability.

4. CONCLUSIONS

Our experiments showed that the composition of the adhesive affects the MBV of paper plaster. Adding the glue mixtures of potato starch (*Amylum Solani*) $C_6H_{10}O_5$ and product Metylan Universal Premium by Henkel increased the moisture buffering abilities to 2.31–2.48 and 2.33–2.35 [g $(m^2 \cdot \%RH)^{-1}$@8 16h^{-1}], respectively. However, for the methylcellulose glue mixture, the moisture buffering ability decreased from 2.39 to 2.08 [g $(m^2 \cdot \%RH)^{-1}$@8 16h^{-1}] with an increase in the amount of glue in the mixture. When some of the hydrogen (H) in cellulose is replaced by methyl radicals (CH_3*), the possibility of hydrogen bonding decreases and affects the properties of paper plaster.

While adding an adhesive to the paper plaster mass is necessary, the glue mixture is its most expensive component. The most expensive glue used for the experiment was methylcellulose, which costs 40 EUR kg^{-1}. Metylan Universal Premium costing 13 EUR kg^{-1} accounted for more than half the price of methylcellulose. In contrast, potato starch $C_6H_{10}O_5$ (*Amylum Solani*) was twenty times cheaper priced at 1.7 EUR kg^{-1}.

Further studies on paper plaster are recommended due to its potential as a favourable environment for microbial growth, attributed to its natural adhesive composition. As the drying period of plaster is a minimum of two weeks, the wet environment might also be a suitable for microbial growth. Additionally, an important aspect that needs further research is the impact of exposing the paper plaster surface to humidity.

ACKNOWLEDGEMENTS

This study has been supported by Tartu College, Tallinn University of Technology.

REFERENCES

1. Fang, J., Zhang, H., Ren, P., He1, B.-J., Tang, M., & Feng, C. (2022). Influence of Climates and Materials on the Moisture Buffering in Office Buildings: A Comprehensive Numerical Study in China. *Environmental Science and Pollution Research, 29*, 14158–14175. https://doi.org/10.1007/s11356-021-16684-3
2. Kaczorek, D., Basińska, M., & Koczyk, H. (2023). Hygrothermal Behaviour of a Room with Different Occupancy Scenarios. *Journal of Building Engineering, 66*, 105928. https://doi.org/10.1016/j.jobe.2023.105928
3. Zhang, M., Qin, M., & Chen, Z. (2017) Moisture Buffer Effect and its Impact on Indoor Environment. *Procedia Engineering, 205*, 1123–1129. https://doi.org/10.1016/j.proeng.2017.10.417
4. McGregor, F., Heath, A., Shea, A., & Lawrence, M. (2014). The Moisture Buffering Capacity of Unfired Clay Masonry. *Building and Environment, 82*, 599–607. https://doi.org/10.1016/j.buildenv.2014.09.027
5. Pavlík, Z., Fořt, J., Pavlíková, M., Pokorný, J., Anton Trníka, A., & Cerný, R. (2016). Modified Lime-Cement Plasters with Enhanced Thermal and Hygric Storage Capacity for Moderation of Interior Climate. *Energy and Buildings, 126,* 113–127. https://doi.org/10.1016/j.enbuild.2016.05.004
6. Acevedo-Sánchez, C.D., Villaquirán-Caicedo, M.A., & Marmolejo-Rebellón, L.F. (2023). Recycling of EPS Foam and Demolition Wastes in the Preparation of Ecofriendly Render Mortars with Thermal-Acoustic Insulation Properties. *Materiales de Construcción, 73* (351), e317. https://doi.org/10.3989/mc.2023.342422
7. Ferrández, D., Álvarez, M., Saiz, P., & Zaragoza, A. (2022). Experimental Study with Plaster Mortars Made with Recycled Aggregate and Thermal Insulation Residues for Application in Building. *Sustainability, 14,* 2386. https://doi.org/10.3390/su14042386
8. Kirwan, M.J. (2013). *Handbook of Paper and Paperboard Packaging Technology*. Wiley-Blackwell.
9. Teearu, M-L. (2018). *Determinantion of Hygrothermal Performance of Paper Clay: Sorption, Water Vapour Permeability and Moisture Buffering*. Master's Thesis. Tallinn University of Technology, Tartu, Estonia. (in Estonian).
10. Vares, M.-L., Ruus, A., Nutt, N., Kubjas, A., & Raamets, J. (2021). Determination of Paper Plaster Hygrothermal Performance: Influence of Different Types of Paper on Sorption and Moisture Buffering. *Journal of Building Engineering, 33*, 101830. https://doi.org/10.1016/j.jobe.2020.101830
11. Nutt, N., Kubjas, A., Nei, L., & Ruus, A. (2020). The Effects of Natural Paint on the Moisture Buffering Ability of Paper Plaster. *Latvian Journal of Physics and Technical Sciences, 57* (5), 51−60. https://doi.org/10.2478/lpts-2020-0027
12. Nutt, N., & Kubjas, A. (2020). Moisture Buffer Value of Composite Material Made of Clay-Sand Plaster and Wastepaper. *Journal of Sustainable Architecture and Civil Engineering, 27* (2), 108−115. https://doi.org/10.5755/j01.sace.27.2.25391.
13. Soolepp, M. (2019). *The Effects of Different Production Methods on Hygrothermal Properties of Paper Plaster.* Master's Thesis. Tallinn University of Technology, Tartu, Estonia. (in Estonian).
14. Soolepp, M., Ruus, A., Nutt, N., Kubjas, A., & Raamets, J. (2020). Hygrothermal performance of paper plaster: Influence of different types of paper and production methods on moisture buffering. In *NSB 2020 – 12th Nordic Symposium on Building Physics*, 6 – 9 September 2020. Tallinn, Estonia.
15. Allikvee, K. (2019). *Analysis of Paper Plaster Wastewater.* Bachelor Thesis. Tallinn University of Technology, Tartu, Estonia. (in Estonian).

16. Fatima, M., Ejaz, A., Sikandar, G., & Abbas, B. (2022). Recycling paper waste into plaster composite mixture. In *1st International Conference on Advances in Civil & Environmental Engineering*, University of Engineering & Technology Taxila, Pakistan, 129.
17. Rode, C. (2005). *Moisture Buffering of Building Materials*. Report BYG·DTU R-126. Available at: http://orbit.dtu.dk/fedora/objects/orbit:75984/datastreams/file_2415500/content
18. Metslang, J. (2012). Vana maamaja käsiraamat. [Old Country House: Handbook]. Tallinn: Tammeraamat (in Estonian).
19. Pere, R. (2008). *Looduslikud ehitusmaterjalid. Seinad, põrand, katused ja siseviimistlus. [Natural Building Materials: Walls, Floor, Roofs and Interior Decorations]*. Tallinn: AS Ajakirjade Kirjastus (in Estonian).
20. Janssen, H., & Roels, A. (2009). Qualitative and Quantitative Assessment of Interior Moisture Buffering by Enclosures. *Energy and Buildings, 41* (4), 382–394. https://doi.org/10.1016/j.enbuild.2008.11.007
21. Phelipot-Mardelé, A., Collet, F., Jiang, Y., Lanos, C., Lawrence, M., Lemke, M. (2019). Moisture Buffering Capacity of Clay Based Plasters. *Academic Journal of Civil Engineering, 37* (2), 363−370. https://doi.org/10.26168/icbbm2019.52
22. Nutt, N., Kubjas, A., & Nei, L. (2020). Adding Waste Paper to Clay Plaster to Raise its Ability to Buffer Moisture. *Proceedings of the Estonian Academy of Sciences, 69* (3), 179−185. https://doi.org/10.3176/proc.2020.3.01

LATVIAN JOURNAL OF PHYSICS
AND TECHNICAL SCIENCES
2024, N 6

DOI: 10.2478/lpts-2024-0044

THE PRACTICAL IMPLEMENTATION OF HYDROGEN-BASED SUSTAINABLE POWER GENERATION BACKUP

A. Backurs[1,3]*, L. Jansons[1,4], L. Zemite[1,2], A. Laizans[3]

[1]Latvian Hydrogen Association,
1 Akademijas Square, Riga, LV-1050, LATVIA
[2]Riga Technical University,
Faculty of Computer Science, Information Technology and Energy,
12-1 Azenes Str., Riga, LV-1048, LATVIA
[3]Latvia University of Life Sciences and Technologies,
Faculty of Engineering,
5 J. Cakstes Blvd., Jelgava, LV-3001, LATVIA
[4]Riga Technical University,
Faculty of Engineering Economics and Management,
6 Kalnciema Str. 210, Riga, LV-1048, LATVIA
*e-mail: andris.backurs@gmail.com

Hydrogen fuel cell backup power is a modern way to ensure an uninterrupted and decentralised supply of electricity. A stationary and mobile fuel cell, commonly referred to as a hydrogen generator, is used to produce electricity during power outages or other emergency situations. These fuel cell backups are designed to provide a reliable and efficient source of electricity for critical loads, such as hospitals, data centres, and other critical infrastructures. Hydrogen generators are typically used in situations where a reliable and efficient source of electricity is needed, and in cases when conventional diesel generators are not the priority. These generators can also be used in remote locations where access to the grid is limited or unavailable, or in applications where the use of fossil fuels is not practical or desirable. The article covers the thematic related to comparison of diesel and hydrogen generators, with regards to advantages and shortcomings of the latter, as well as provides an insight into possible use of hydrogen generators in Latvia.

Keywords: *Areas of use, generation backup, hydrogen, hydrogen generators.*

1. INTRODUCTION

The energy sector, including power generation, transportation, heating and industry – is responsible for more than 70 % of the global greenhouse gas (GHG) emissions [1]. Achieving climate neutrality would require a substantial restriction on the use of fossil fuels in the energy sector, replacing them with renewable energy sources (RES) and other climate neutral or low carbon fuels. As a direct consequence, the share of the European Union (EU) renewable electricity production and other decarbonised energy carriers are set to gradually replace all current fossil uses. Such an accomplishment would largely decarbonise electricity from the grid in 2030 and turn it climate neutral by 2050 [2]. This would also present a significant opportunity to make the demand sectors of the economy climate neutral (buildings, transport, and industry). Nevertheless, energy transformation comes with several challenges that need to be addressed. The significant deployment of RES will require the deployment of energy storage and smart grid solutions capable of addressing its variable generation profile [3]. At the same time, electrification based on today's technology perspectives seems to be seen as an increasingly cost-efficient solution for some sectors, but not for all.

Across different examined alternatives complementing electrification, almost all recent economic analyses indicate that hydrogen is an energy carrier that can play a critical role in filling the gap and addressing challenges of future green energy landscape formation. Hydrogen can be used as a feedstock, a fuel, an energy carrier and an energy storage medium, and, thus, has many possible applications across industry, transport, power and buildings sectors [4]. Most importantly, when produced sustainably, it does not emit carbon dioxide (CO_2) and does not pollute the atmosphere when used. It is, therefore. an important part of the overall solution to meet the 2050 climate neutrality goal of the European Green Deal [5].

Low-carbon and green hydrogen can be used to replace fossil fuels in hard to abate sectors and complement RES in the effort to transform the European economy. Furthermore, there is also considerable potential to repurpose the current gas infrastructure to carry and store the hydrogen, helping achieve EU's climate goals much faster and more economically using existing infrastructure [6]–[8]. In its strategic vision for a climate-neutral EU presented by the European Commission on 28 November 2018, the share of hydrogen in Europe's energy mix is projected to grow from the current less than 2 % to 13–14% by 2050. The projections were confirmed in the recent impact assessment for the 2030 Climate Target Plan [9], as well as the impact assessments supporting the various policy proposals of the "Fit for 55" package, where the policy scenarios considered project a ramp up of the installed electrolyser capacity between 37–66 gigawatt (GW) by 2035, while for 2050 all policy scenarios project the share for hydrogen in final energy consumption to be at least 9 % across policy scenarios.

Blending hydrogen with natural gas in the pipelines is facilitated in the gas and hydrogen markets package, by allowing blends of up to 5 % hydrogen volume into natural gas flows to be accepted and facilitated at cross-border points from October 2025, while voluntary agreements for higher blends at interconnection points between Member States remain possible [10], [11].

In 2020, the European Commission adopted the hydrogen strategy for a climate-neutral Europe [12], which identifies as the priority for the EU to develop renewable hydrogen, produced using mainly wind, hydro and solar energy. This should be the main form of hydrogen in the long-term, towards 2050, supported by the very high shares of renewable electricity. In the mid-term, other forms of low-carbon hydrogen will also be needed, both to support the uptake of hydrogen as energy carrier and feedstock, and to replace most polluting forms of producing hydrogen.

Multiple industries are facing the fact that there is a range of power needs that cannot be based on the energy grid alone. From construction to building and manufacturing, many sectors of the global economy need reliable alternatives. These sectors also require independent energy storage to provide resilience, for example, if the grid is unstable or unreliable. Some consumers have power requirements that must be faster than a grid connection. Others need control over their power contracts to sustain company growth. There are countless diverse use cases for off-grid energy generation and storage depending on location and industry, but all consumers share three common requirements: reliability, flexibility, and practicality. These industries are currently still being served by diesel generators, but now being urged and legislated to decarbonise. Unfortunately, diesel generators produce too high levels of GHG, including SO_x, NO_x and particulate matter, so their longevity in the EU is quite doubtful.

It is obvious that diesel generators will be completely phased out with time, but their place will be taken by other, more sustainable and green technologies, such as hydrogen generators, which have a great market potential not only in the EU, but also locally. There are currently approximately 5000 generators with a capacity of 100 kilowatt (kW) in Latvia alone, which could be subject to gradual replacement with hydrogen powered analogues [13].

As governments EU-wide are introducing policies to encourage the adoption of green hydrogen-based energy solutions, subsidies and incentives for hydrogen technology research and infrastructure development are becoming more common, aiming to reduce costs and broaden adoption. Looking ahead, as technology advances and costs decrease, hydrogen generators are poised to become a significant part of the EU's energy landscape. Industry decision-makers should focus closely on these developments as hydrogen technology continues to evolve and potentially take over from fossil-fuel-based generators.

2. DIESEL AND HYDROGEN GENERATORS

Diesel generators originated in the early 20th century, with significant adoption during World War II. Advances over the decades have made them quieter, more efficient, and more durable, leading to their widespread use in various sectors today [14]. At the same time, the concept of hydrogen fuel cells dates to the 19th century, but major developments occurred in the latter half of the last century [15]. Initially used in aerospace, fuel cell technology has expanded to commercial and industrial applications, offering sustainable energy solutions. The evolution of these technologies reflects ongoing efforts to improve efficiency, durability, and environmental impact, driving current interest in alternative energy sources such as hydrogen generators.

Diesel generators use internal combustion engines powered by diesel fuel to produce electrical power. They are used as standalone or backup power units for various industrial applications. Noted for their quick startup times, fuel efficiency, and high-power output, diesel generators have become a staple in the energy sector. In contrast, hydrogen generators utilise fuel cell technology, converting hydrogen gas into electricity through a chemical reaction with oxygen, with water as the only by-product. This relatively new technology promises higher efficiency and cleaner energy than traditional fossil fuel-based generators.

2.1. Types of Hydrogen Generators

The most compelling advantage of hydrogen generators is their environmental impact. Unlike diesel generators, hydrogen generators produce only water vapour as a by-product, making them an ultra-low emissions option. This aligns perfectly with global efforts to reduce GHG emissions and combat climate change.

Hydrogen generators can use two very different technologies to turn hydrogen into electricity:

- internal combustion engine – like the combustion engine used in current diesel generators. Here, a hydrogen-air mixture is burned inside a combustion chamber. Just like diesel, this miniature explosion produces force to turn a crankshaft, and an electrical current is generated via the attached alternator;
- a cell technology – it generates electricity by chemically reacting hydrogen with oxygen (usually from the air) to create water. Hydrogen is put into close contact with oxygen inside the fuel cell, separated only by a membrane – for instance, a proton-exchange membrane (PEM). The hydrogen's proton moves through this membrane to react with the oxygen, which forces the hydrogen's electron along a circuit to re-join, creating an electric current. Water is then evacuated from the fuel cell as the only by-product. There are many different types of fuel cells, but their working principle is very similar [16].

In most cases, a hydrogen generator will be connected to external hydrogen sources – bottled hydrogen. This hydrogen is typically produced somewhere else and brought in gas bottles to the location of the hydrogen generator. Internally hydrogen generators will contain fuel cells, power electronics, control systems for electronics.

2.2. Efficiency of Hydrogen Generators

If judged by key parameters, hydrogen generators are more efficient than diesel generators. Fuel cells can convert up to 60 % of the fuel's energy directly into electricity, whereas diesel engines typically operate at around 30–40 % efficiency. This higher efficiency translates to less fuel consumption and lower operational costs over time. Table 1 lists the difference in key parameters of hydrogen and diesel generators.

Table 1. The Difference in Key Parameters of Hydrogen and Diesel Generators

Parameter	**Hydrogen generator**	**Diesel generator**
Efficiency (%)	>60	30–40
Emissions (g CO_2/kWh)	0	2.7
Noise Level (dB)	40–60	70–90
Fuel Availability	Moderate	High
Maintenance Frequency	Low	High

Additionally, hydrogen generators are quieter, generating minimal noise during operation. This is particularly advantageous in environments where noise pollution is a concern, such as residential areas or wildlife conservation zones [17].

2.3. Challenges of Hydrogen Generator Use

At the same time, there are also the challenges to overcome: storing hydrogen is more complex and demanding task than diesel, and while the cost per unit of a PEM fuel cell is broadly equivalent to the same capacity diesel generator, hydrogen is around three times more expensive as a fuel when all costs are factored in. However, in some countries hydrogen production costs can already be close to some conventional fuels [18].

One method of offsetting the hydrogen costs is to simply use a small solar array to fill larger hydrogen storage tanks when the sun shines – especially relevant for backup scenarios, where running the cells for more than a few hours is unlikely. However, even this ingenuity raises questions around the carbon debt of the solar panels, and that is before getting into the ethics of platinum mining, given platinum is a key component of PEM cells.

While the diesel generator era is far from over, in some areas of commercial and industrial activities hydrogen generators are clearly aimed to catch up. In the data centre context, both batteries and fuel cells offer strong potential alternatives to diesel. Also delivering backup power in a cleaner and more sustainable way, the ability to load balance the electricity grid adds an additional layer of value for data centre operators and utility companies alike.

3. POSSIBLE IMPLEMENTATION IN LATVIA

3.1. The Generator Type

5 kW electric power generator from one of the leading manufacturers of hydrogen equipment that uses hydrogen as fuel and fuel cell technology to provide up to 5 kW of reliable backup DC power on demand was chosen for installation in Latvia's pilot (demonstration project). The intended application of this system is backup power for some critical power applications, telecommunication equipment, households and small businesses.

Fig. 1. 5 kW hydrogen generator unit.
Source: Ballard.com

The chosen system continuously monitors the DC bus voltage in a standby mode and operates during power outages when the DC bus voltage drops to a customer defined set point. It is designed for a 19” rack installation (see Fig. 2). The system can be delivered in two configurations: either as a standard solution with an UltraCap module add-on for battery free backup (see Fig. 3), or with customer supplied batteries. Multiple systems also can be coupled in parallel for higher loads than 5 kW (with maximum 12 systems in parallel for up to 60 kW output). The chosen system can be used both indoors and outdoors (see Fig. 2). The multiple system coupling principle is shown in Fig. 4.

Fig. 2. Chosen system’s indoor and outdoor variations with different load capacities.
Source: Ballard.com

Fig. 3. The chosen system’s indoor and outdoor variations with
UltraCap module highlight.
Source: Ballard.com

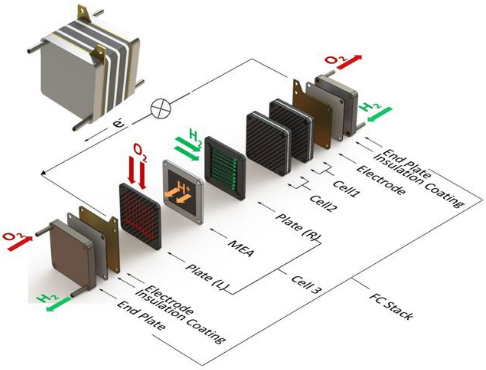

Fig. 4. Principal scheme of fuel cell stack operation and components.

It may be used in many applications/ industries such as:

- structural and civil engineering;
- emergency power supply for critical infrastructures;
- road construction and maintenance;
- emergency services;
- technical relief organisations;
- events and film industry;
- forestry;
- military;
- telecommunication industries;
- emergency power supply in buildings.

In Latvia, potential use of the chosen system could include all above-mentioned applications/industries, and particular activities that relate to backpacking elements of critical infrastructure, tier standard-compliant data centres and telecommunication equipment.

3.2. Critical Infrastructure

Critical infrastructures depend on a reliable power supply. A reliable emergency power system is of critical importance especially when using modern information and communication technology, like one for authorities and organisations with security tasks. Effective, broadband communication between the scene and situation centres is necessary for an optimised and realistic assessment of the situation. Conventional battery solutions make it very difficult to ensure long operational reliability, which can last several days. It means that hydrogen generation backups could help compensate for lost capacities and load more effectively. The chosen system's potential integration in a grid backup scheme is depicted in Fig. 5.

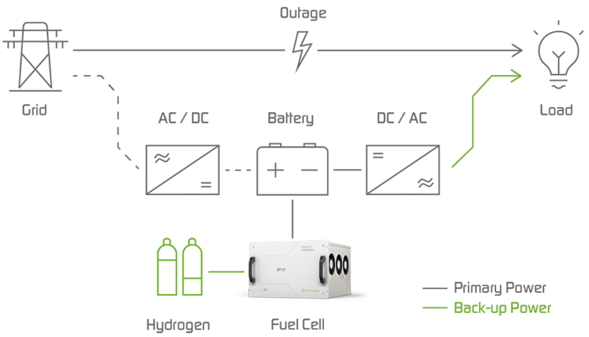

Fig. 5. Chosen system's potential integration in a grid backup scheme.
Source: efoy-pro.com

Hydrogen generators are already in use in many locations to provide backup power. The fuel cell modules switch on completely automatically and take over the load no later than 20 seconds after the power fails. Compared to solutions with diesel generators, no CO_2 emissions are generated here. Another advantage of the hydrogen generators is the low maintenance effort as well as the low ageing tendency in standby mode. This ensures system availability for long periods of time.

Keeping in mind its limited power, the chosen system's hydrogen backups will be useful in future when extensive development of microgrids and local smart grids will become more developed than today [19].

3.3. Emergency Power for Data Centres and Telecommunication Equipment

Reliable power is a requirement for all tier standard-compliant data centres and telecommunication equipment. If even in Latvia data centres of large data/processing storage capacity are not very numerous yet (there are 22 data centres of different scale in Riga [20]), the possibility of their emergence in future opens up an avenue for choosing sustainable hydrogen generator backups as primary means for securing their flawless functioning.

The chosen system with the same technical parameters is already in operation in several EU countries, including Sweden, approving that extreme temperature fluctuations and other negative factors does not impact it operation to the point when its safety and reliability would be questioned. Figure 6 shows the chosen system's 5 kW outdoor installation with external hydrogen bottles in the right-hand side compartment of an installation cabinet [21]. The same system could be installed in the Latvian telecommunication tower and other equipment to ensure flawless operation of the systems in case of prolonged power outages.

Fig. 6. The chosen system's 5 kW outdoor installation with external hydrogen bottles.
Source: Wattenfall.com

Regarding data centres, in recent years, their owners have made strides to reduce power-related outages, though they are still a major pain point. According to a 2022 survey from the Uptime Institute, power-related problems accounted for 43 % of significant outages at data centres (outages that caused downtime and financial loss).

Moreover, the cost of downtime is increasing. In the same Uptime survey, it was reported that 60 % of failures resulted in at least $ 100,000 in total losses, up from

39 % in 2019. The share of outages that resulted in > $ 1 million of losses increased from 11 % to 15 % over the same period [22]. Given the importance of uptime on profitability, it is no surprise that data centre owners continue to rely on tried-and-true technologies like diesel generators as a source of backup power.

Today, clean alternatives to backup diesel generators are limited. While some developers have turned to natural gas-fired generators to reduce their carbon footprint, they are still incompatible with net-zero ambitions. Furthermore, NO_x and SO_x emissions are not eliminated, and noise levels are like that of diesel generators.

There is a notion that batteries are critical for delivering instantaneous power provided by uninterruptable power systems. However, batteries are typically not a viable option for handling the sustained power loads that many data centres require for backup (continuous power for hours or possibly days). Power demand of large data centres can range from 100 to 1000 megawatts (MW). A battery system capable of handling the facility's entire load for an extended period would be highly prohibitive from both a footprint and CAPEX perspective [23].

Google estimates that there are a total of around 20 GW of backup diesel generators worldwide [24], so to decarbonise its own backup, the internet search giant tested the 3 MW battery backup solution at its St. Ghislain data centre in Belgium [25], with an eye to providing load-balancing services to the grid as a potentially valuable side benefit [26].

4. CONCLUSIONS

- With increasing concerns about climate change and the need to reduce GHG emissions, hydrogen has emerged as a viable alternative to fossil fuels. Hydrogen generators offer a pathway to decarbonise sectors that are challenging to electrify, such as heavy industry, long-haul transportation, data centres and telecommunication systems.
- Hydrogen can serve as a valuable energy storage medium, allowing excess renewable energy to be stored as hydrogen and utilised when needed. It can help address the intermittent of renewable energy sources like solar and wind power, supporting grid stability and reliability.
- Hydrogen generators can be deployed across various applications, including transportation, power generation, industrial processes, and energy storage. The versatility of hydrogen as an energy carrier makes it suitable for a wide range of sectors, offering scalability and flexibility in meeting energy demand.
- Ongoing advancements in hydrogen production, storage, and utilisation technologies are driving down costs and improving efficiency. Innovations such as electrolysers, fuel cells, and hydrogen storage materials are making hydrogen generators more competitive with traditional energy sources.

ACKNOWLEDGEMENTS

The research has been funded by project No. 5.1.1.2.0/1/22/A/CFLA/001 "Design and Development of a Hydrogen Back-up Power Supply System".

REFERENCES

1. C2ES. (n.a.). Global Emissions. Available at: https://www.c2es.org/content/international-emissions/
2. EC. (2014). *Commission Communication on a Policy Framework for Climate and Energy from 2020 to 2030 - COM(2014) 0015.* Available at: https://eur-lex.europa.eu/legal-content/EN/ALL/?uri=celex%3A52014DC0015
3. Tan, K. M., Babu, T. S., Ramachandaramurthy, V. K., Kasinathan, P., Solanki, S. G., & Raveendran, S. K. (2021). Empowering Smart Grid: A Comprehensive Review of Energy Storage Technology and Application with Renewable Energy Integration. *Journal of Energy Storage, 39*. https://doi.org/10.1016/j.est.2021.102591
4. Muhammed, N.S., Gbadamosi, A. O., Epelle, E. I., Abdulrasheed, A. A., Haq, B., Patil, S., … & Kamal, M. S. (2023). Hydrogen Production, Transportation, Utilization, and Storage: Recent Advances towards Sustainable Energy. *Journal of Energy Storage, 73* (D). https://doi.org/10.1016/j.est.2023.109207
5. Worldfavor. (n.a.). *What is the EU Green Deal? A Breakdown of the Essentials.* Available at: https://blog.worldfavor.com/what-is-the-eu-green-deal
6. Jansons, L., Zemīte, L., Zeltiņš, N., Geipele, I., & Bačkurs, A. (2023). Green and Sustainable Hydrogen in Emerging European Smart Energy Framework. *Latvian Journal of Physics and Technical Sciences*, *60* (1), 24–38. http://doi:10.2478/lpts-2023-0003
7. Zemite, L., Backurs, A., Starikovs, A., Laizāns, A., Jansons, L., Vempere, L., …& Broks, A. A. (2023). Comprehensive Overview of the European and Baltic Landscape for Hydrogen Applications and Innovations. *Latvian Journal of Physics and Technical Sciences*, 60 (3), 33–53. http://doi:10.2478/lpts-2023-0016
8. Jansons, L., Zemīte, L., Zeltiņš, N., Bode, I., Geipele, I., & Kiesners, K. (2022). The Green Hydrogen and the EU Gaseous Fuel Diversification Risks. *Latvian Journal of Physics and Technical Sciences*, *59* (4), 53–70. http://doi:10.2478/lpts-2022-0033
9. EC. (2020). *Commission Staff Working Document Impact Assessment Accompanying the Communication Stepping up Europe's 2030 Climate Ambition.* SWD(2020) 176 final. Available at: https://eur-lex.europa.eu/legal-content/EN/TXT/?uri=CELEX%3A52020SC0176
10. EC. (2021). *Proposal for Regulation "Internal Markets for Renewable and Natural Gases and for Hydrogen (Recast)". COM(2021) 804 final.* Available at: https://eur-lex.europa.eu/legal-content/EN/TXT/?uri=COM%3A2021%3A804%3AFIN
11. Zemite, L. Jansons, L., Zeltins, N., Lapuke, S., & Bode, I. (2023). Blending Hydrogen with Natural Gas/Biomethane and Transportation in Existing Gas Networks. *Latvian Journal of Physics and Technical Sciences, 60* (5), 43–55. https://doi.org/10.2478/lpts-2023-00380
12. EC. (2020). *Communication from the Commission to the European Parliament, the Council, the European Economic and Social Committee And The Committee of the Regions. A Hydrogen Strategy for a Climate-Neutral Europe.* Available at: https://eur-lex.europa.eu/legal-content/EN/TXT/?uri=CELEX:52020DC0301
13. Backurs, A., Zemite, L., & Jansons, L. A Technical and Economic Study of Sustainable Power Generation Backup. *Latvian Journal of Physics and Technical Sciences, 60* (4), 75–88. https://doi.org/10.2478/lpts-2024-0029
14. Power Electrics. (2024). *The History of the Diesel Generator.* Available at: https://powerelectrics.com/blog/the-history-of-the-diesel-generator
15. Andújar, M., & Segura, F. (2009). Fuel Cells: History and Updating. A Walk along Two Centuries. *Renewable and Sustainable Energy Reviews, 13* (9). https://doi.org/10.1016/j.rser.2009.03.015

16. Cummins. (2022). *Hydrogen Internal Combustion Engines and Hydrogen Fuel Cells*. Available at: https://www.cummins.com/news/2022/01/27/hydrogen-internal-combustion-engines-and-hydrogen-fuel-cells
17. Skoon. (n.a.). *Hydrogen Generators and Fuel Cells Demystified – Why and When to Use Them*. Available at: https://www.skoon.world/blog/hydrogen-generators-and-fuel-cells-demystified-why-and-when-to-use-them/
18. Michaelsenergy. (n.a.). *Colors and Costs of Hydrogen vs. Natural Gas*. Available at: https://michaelsenergy.com/colors-and-costs-of-hydrogen-vs-natural-gas/
19. Jiayi, H., Jianxiao, W., Zhihao, H., Qi, A., Yiyang, S., Asad, M., … & Feng, G. (2023). Hydrogen-Powered Smart Grid Resilience. *Energy Conversion and Economics, 4* (2), 89–104. https://doi.org/10.1049/enc2.12083
20. Data Center Map. (n.a.). *Riga Data Centers*. Available at: https://www.datacentermap.com/latvia/riga/
21. Vattenfall. (2022). *Vattenfall Commissions Hydrogen Gas-Driven Backup Power for Telecoms Networks*. Available at: https://group.vattenfall.com/press-and-media/newsroom/2022/vattenfall-commissions-hydrogen-gas-driven-backup-power-for-telecoms-networks
22. Uptime Institute. (2022). *Uptime Institute's 2022 Outage Analysis Finds Downtime Costs and Consequences Worsening as Industry Efforts to Curb Outage Frequency Fall Short.* Available at: https://uptimeinstitute.com/about-ui/press-releases/2022-outage-analysis-finds-downtime-costs-and-consequences-worsening
23. IEA. (n.a.). *Data Centres and Data Transmission Networks.* Available at: https://www.iea.org/energy-system/buildings/data-centres-and-data-transmission-networks
24. Arcadis. (2024). *Replacing Diesel Generators with Battery Energy Storage Systems.* Available at: https://www.arcadis.com/en/knowledge-hub/blog/global/jeff-gyzen/2024/replacing-diesel-generators-with-battery-energy-storage
25. Data Center Knowledge. (2020). *Google Thinks Data Centers, Armed with Batteries, Should 'Anchor' a Carbon-Free Grid.* Available at: https://www.datacenterknowledge.com/hyperscalers/google-thinks-data-centers-armed-with-batteries-should-anchor-a-carbon-free-grid
26. PoweCell Group. (n.a.). *Is it Time to Replace Diesel Gensets with Hydrogen Fuel Cells?* Available at: https://powercellgroup.com/is-it-time-to-replace-diesel-gensets-with-hydrogen-fuel-cells/

LATVIAN JOURNAL OF PHYSICS
AND TECHNICAL SCIENCES
2024, N 6

DOI: 10.2478/lpts-2024-0045

AIR FLOW ANALYSIS FOR TRIPLY PERIODIC MINIMAL SURFACE HEAT EXCHANGERS

A. Kancs

WEMPS SIA,
3 Straupes Str., Riga, LV-1073, LATVIA
E-mail: arturs.k@wemps.eu

Due to the increasing popularity of additive manufacturing technologies, more varied and complex shapes of heat exchangers can be produced that can be optimised to be more compact and efficient. In this paper, a triply minimal periodic surface – gyroid structure – is designed to study the applicability of such structures in compact air-to-air heat exchangers used in residential ventilation recuperation systems. Gyroid surface structures could potentially decrease overall heat exchanger size, pressure and increase heat transfer. Several geometry variations with different flow rate values were analysed to compare the efficiency of heat exchanger designs. Additionally, a literature review was conducted to identify more adaptable geometric parameters of the gyroid structure. To calculate the pressure difference, temperature and heat transfer in each variation, SolidWorks Flow Simulation was used. The results showed that by using gyroid structures, heat exchanger energy transfer can be optimised for required back pressure and heat transfer, while reducing the overall dimensions, compared to conventional heat exchangers. By incorporating low cost, printed thermal recuperators, thermal efficiency of residential buildings can be improved. Suitable materials, manufacturing methods and application limitations are discussed.

Keywords: *Additive manufacturing, CFD, gyroid, heat transfer, thermal recuperator.*

1. INTRODUCTION

Household energy efficiency is becoming more and more important, as it is one of the options to improve sustainability. At the same time, 3D printing technologies are becoming more advanced, allowing higher complexity and larger models to be printed, as well as increasing the available material list for this process. This results in almost any geometry being physically producible, such as TPMS (triply periodic minimal surfaces). Surfaces like these are found in nature, and lately have been studied for use in engineering applications, such as heat exchangers for residential heat recovery. By using these novel methods, more compact size devices with lower pressure loss, noise and higher thermal efficiency could be implemented. Nearly limitless possibilities in design using 3D printing methods give way for numerous options for research and development of such structures.

During the analysis of publications, the results of research and experiments of TPMS structure use in heat transfer applications, such as heat exchangers and cooling ribs, were collected and analysed. The most studied and practically used types of these surfaces are Schwarz-diamond and gyroid, and this study will focus mostly on gyroid structure. Below, the equation of the single-cell approximations of gyroid surface by the spatial coordinates of x, y, z is provided [1]:

$$\sin(x)\cos(y) + \sin(y)\cos(z) + \sin(z)\cos(x) = 0. \tag{1}$$

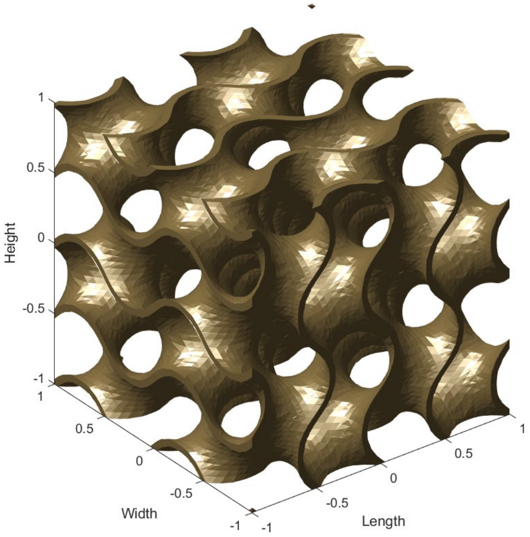

Fig. 1. Gyroid TPMS model.

There are different ways to manipulate the geometry of TPMS in heat exchangers – to change the porosity, wall thickness, cell sizes, as well as to make gradually changing porosity structures. To improve heat transfer, studies have investigated the degree of porosity of TPMS-based structures. For gradual TPMS, the porosity can be varied along the length, width or height of the channel while keeping the overall porosity of the structure the same.

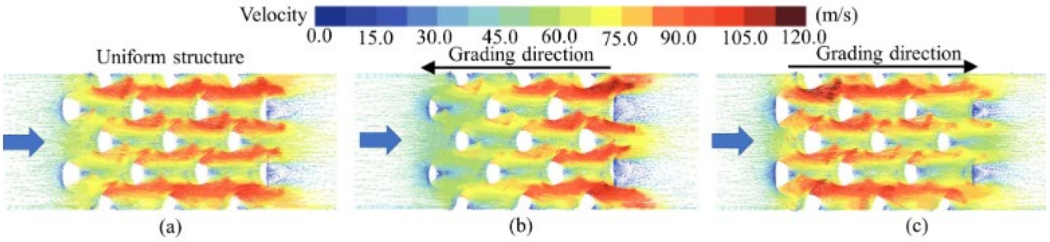

Fig. 2. Velocity vectors in proportional and gradient TPMS structure at high Re flow [2].

Gradually increasing the porosity in the flow direction can show better results than uniform porosity or gradually decreasing porosity sheet TPMS models (see Fig. 2). For example, at high Reynolds number flow and Schwarz-d structure, by increasing the porosity by 2.5 %, pressure loss in channels was reduced by 27.6 %, while reducing the heat transfer coefficient only by 15.7 % [2]. This implies that by reducing the overall porosity of the structure and using gradually increasing porosity channels, it is possible to increase the heat transfer at the same pressure loss, compared to a uniform model. Such manipulations with TPMS geometry could create an opportunity to improve the flow parameters without changing the overall size of the heat exchanger.

By reducing the overall uniform porosity, channel dimensions are decreased, which increases the flow speed. That increases the convective heat transfer coefficient in the channels (see Fig. 3), while also increasing the pressure loss significantly. The heat transfer coefficient is also affected by the surface area changes in the same volume, which increases by reducing the porosity [3].

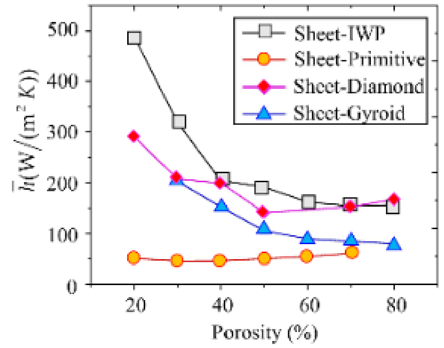

Fig. 3. Effect of porosity on convective heat transfer coefficient at Re = 40 [3].

There are studies performed on various gyroid wall thicknesses at constant cell sizes and porosity, which conclude, that increasing the wall thickness in TPMS structures, there can be an increase in a convective heat transfer coefficient. Although the convective heat transfer coefficient increases, thick walls can interfere with flow, creating regions of backflow (Fig. 4), which reduces the thermal efficiency of the system. Because of both good thermal efficiency and low-pressure loss, thin walled TPMS heat exchangers show better results [4].

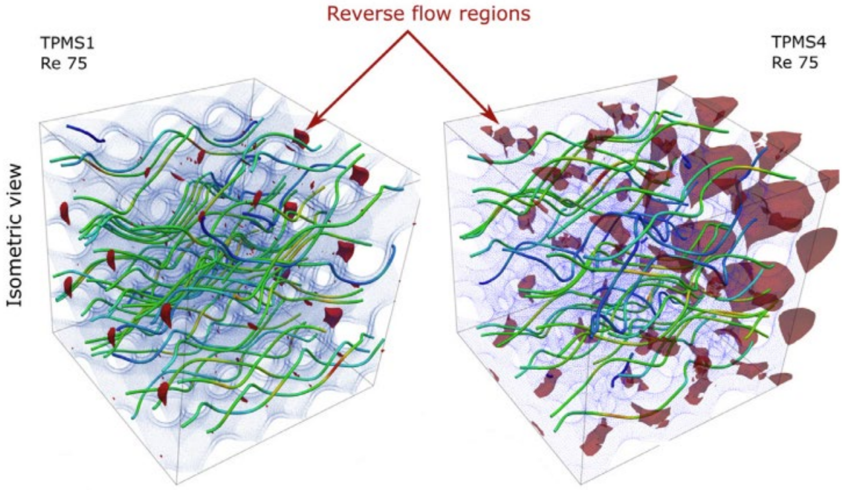

Fig. 4. Backflow regions in thin walled and thick walled Schwarz-d model [4].

Results from cell size studies imply that TPMS with larger cell sizes produce lower pressure loss in the system, while smaller cell sizes significantly increase the pressure loss, especially at higher Reynolds number flow. It can be concluded that gyroid and primitive strictures with smaller cell sizes produce the largest pressure losses compared to other types of TPMS, which can be explained by their relatively complex geometry and lower porosity (see Fig. 5) [5].

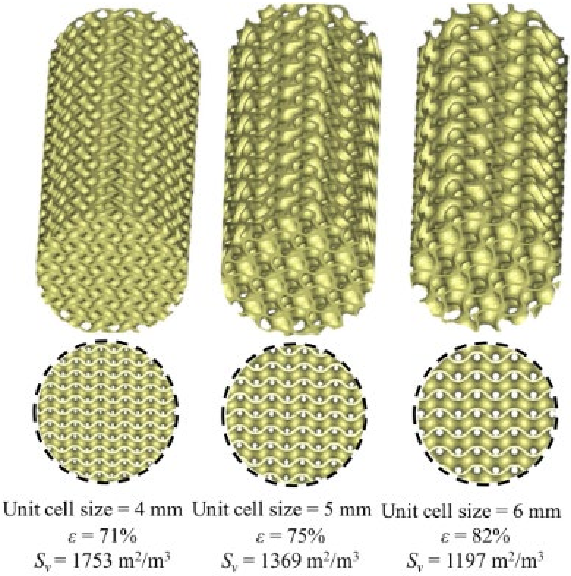

Fig. 5. Gyroid structure cell size, porosity and specific surface area [5].

Comparing the flow regimes in the previously mentioned TPMS heat exchangers, it can be concluded that in the lowest pressure systems Schwarz-d structure has the better thermal performance [6], while at turbulent flows and high flow speeds, gyroid can perform better [7].

Using the information collected from previous studies, gyroid heat exchanger was modelled, test printed for numerical flow simulations, in order to review the effect of cell sizes and cell proportions on thermal efficiency as well as pressure loss.

2. MODEL DESIGN AND BOUNDARY CONDITIONS

Using previously mentioned Eq. (1), base model of gyroid structure was modelled in SolidWorks 2020 CAD software. The base surface model, used for all following numerical simulations, was a gyroid cell surface (Fig. 6) with dimensions of 20x20x20 mm. Using this model, the geometry could be patterned as required, as the structure is periodic in any given direction.

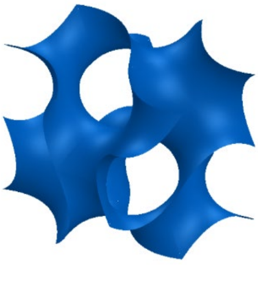

Fig. 6. Gyroid surface model cell.

To better observe flow parameters similarly to a cell of a real life-sized air-to-air heat exchanger, numerical model geometry size of 40x40x180 mm was chosen. This way a full-length counter flow channels can be simulated, while not using excessive computational capacity. Enlarging the TPMS structure models significantly increases the computational resources needed to perform flow calculations, so it is necessary to create geometric models of the smallest possible size.

By applying a thickness to the surface model, a solid model of structure was acquired. To create flow channels for SolidWorks Flow Simulation 2020, a heat exchanger body was created (Fig. 7). The model consists of a body with two inlet and two outlet channels and gyroid surface core. Both cold air (blue) and hot air (red) inlets and outlets were placed in 40 mm distance from the gyroid structure to help with flow steadiness before entering the structure, as well as decreasing the possibility of flow vortexes across pressure boundaries. In order to avoid the influence of the auxiliary geometry on the results, the body and lids in the model were defined as ideal walls with a friction coefficient = 0, as well as a heat transfer coefficient of 0 W/m*K.

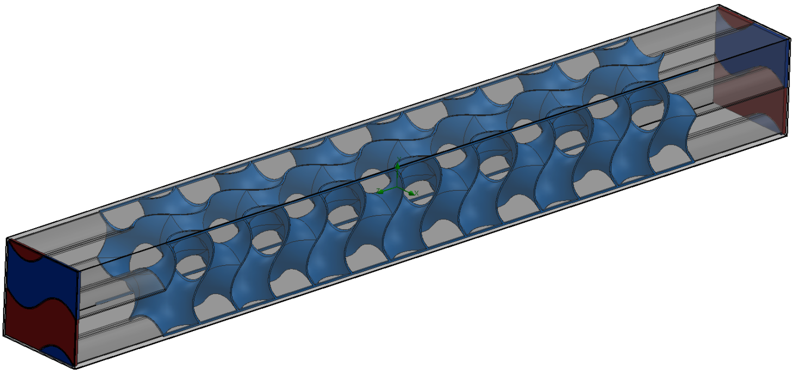

Fig. 7. Simulation model.

In order to study different geometric parameters, it was necessary to completely remodel each heat exchanger, since triply periodic surface modelling is not a built-in feature in the SolidWorks environment. Given the time consumption of modelling computationally complex structures, it was not possible to perform a large number of calculations. Since these patterns and flow channels are repeated periodically in all 3 axis directions, it is not possible to create a 2D model to simplify the CFD calculation.

Plastic with a heat exchange coefficient of 0.2 W/m*K was defined as heat exchanger material, and the chosen wall thickness of 0.6 mm was chosen. To choose a wall thickness several test prints were made, using a Prusa MK3S FFM/FDM 3D printer, 0.4 mm nozzle, and Prusament PETG filament. While trying to reach the smallest wall thickness (around 0.6 mm), stringing, holes in walls and rough surface texture were observed. While these deformations could be eradicated by fine tuning the print settings, such as temperature of the nozzle, print speed, retraction of the nozzle, ambient temperature, very small wall thicknesses were not likely to be reached. As the material heat transfer coefficient is very low, bigger wall thickness for TPMS heat exchangers can significantly decrease the heat transfer between channels.

While larger scale heat exchanger printing using a FFM printer could be feasible, especially if specific thermally conductive plastic filaments were used, an UV LCD resin 3D printer Creality Halot Mage Pro was tested for thin wall gyroid structure printing. Resulting prints (Fig. 8) had much better surface quality, no stringing and completely intact walls. Even lower wall thicknesses could be printed with good results; however, finalized prints always had slightly bigger wall thickness than modelled, so 0.6 mm was chosen as more realistic dimension for large scale printing.

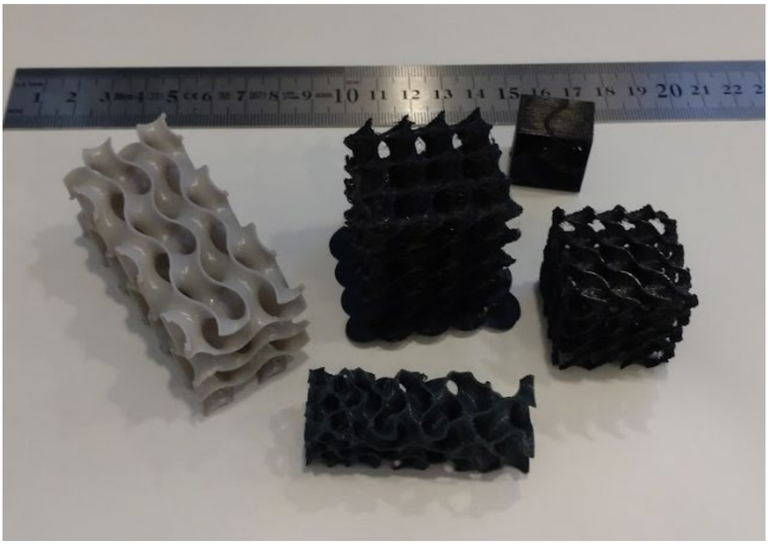

Fig. 8. Gyroid structure samples printed with FFM 3D printer (black) and UV LCD printer (white).

After the initial CAD geometry development, modelling of different cell size structures was carried out.

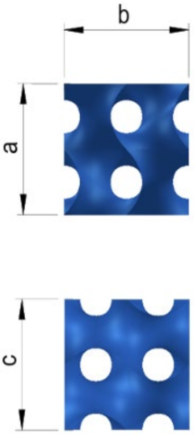

Fig. 9. Gyroid cell.

To compare gyroid cell size effect on heat transfer and pressure drop, three different gyroid structure variants were created, changing the size of the cell (Fig. 9) in each iteration, but keeping the overall model dimensions and wall thickness (0.6 mm). Specific surface area and porosity were determined by SolidWorks mass properties tool, but the hydraulic diameter for porous structures was calculated using the following formula [8]:

$$D_h = \frac{4\varepsilon}{S_s}, \tag{2}$$

where ε is the porosity (a ratio of volume of flow channels for fluid flow to total volume of structure), S_s is the specific surface area (a ratio of gyroid surface area to the total volume of structure). Resulting hydraulic diameter for each cell size study is shown in Table 1.

Table 1. Cell Size Study Geometric Parameters

Cell size, [mm]	Specific surface area, S_s [m^2/m^3]	Porosity, ε	Hydraulic diameter D_h [m]
20x20x20	314.9	90.6 %	0.0115
30x30x30	213.7	95.1 %	0.0178
40x40x40	155.7	95.5 %	0.0245

Similarly, more studies were conducted on disproportionate gyroid cells, with different cell dimension in flow direction (Table 2). The obtained porosity values are over 90 % for all studies, which results from thin gyroid walls used – the cell length has little to no impact on structure porosity.

Table 2. Cell Length in Flow Direction Study Geometric Parameters

Cell size, [mm]	Specific surface area, S_s [m^2/m^3]	Porosity, ε	Hydraulic diameter, D_h [m]
20x20x20	314.9	90.6	0.0115
20x20x25	295.7	90.8	0.0123
20x20x30	283.8	90.8	0.0128
20x20x40	271.0	90.8	0.0134
20x20x50	264.4	90.8	0.0137

The gyroid solid model was assigned properties presented below.

Table 3. Material Properties Assigned

Material properties	Value
Average density [$kg.m^{-3}$]	1270
Specific heat [$J.kg^{-1}$ K^{-1}]	1000
Thermal conductivity [$W.m^{-1}.K^{-1}$]	0.2

The defined flow medium is air, with inlet volume flow values of 0.5, 1.875. 3.25, 4.625. 6 m^3/s. In all simulations, the temperature at the hot inlet is 20.05 °C, the temperature at the cold inlet is 0 °C, and the atmospheric pressure is set to 101325 Pa. The value of the inlet volume flow in the channels is variable to evaluate the influence of different flow parameters on the results. To solve K-ε transport equations for the turbulent kinetic energy, its dissipation rate was used, as it is the only turbulence model available by SolidWorks Flow simulation solver. Solving of 3-dimensional flow – pressure, velocity and other values – was done using Navier-Stokes equation system. Detailed mathematical model is defined in SolidWorks Flow Simulation 2020 Technical Reference [9].

To describe the effect of cell sizes on flow characteristics, temperature difference in cold and hot channels, and pressure drop in cold and hot channels were collected. The temperature difference was obtained by subtracting the average calculated outlet temperature from the inlet temperature in one channel. Pressure drop values were obtained analogously.

3. RESULTS AND DISCUSSION

The results provided in this study are pressure loss of air flowing through heat exchanger channels and temperature difference between each channels inlet and outlet. A total of 15 simulations were performed to study the effects of cell sizes on heat exchange and pressure drop, as well as 25 simulations on cell length effects.

In order to determine the flow characteristics in porous channels in each study case, Reynolds number was calculated [8]:

$$Re = \frac{D_h v \rho}{\mu \varepsilon}, \tag{3}$$

where D_h is the hydraulic diameter, v is the flow velocity, μ is the viscosity and ρ is the density of the flowing fluid. Density and viscosity were chosen as an average of inlet and outlet values. Calculation of hydraulic diameter for porous structures was discussed in the previous paragraph.

The obtained Reynolds number values from hydraulic diameter and flow parameters (Table 4) indicate flow being in transition region (10–200) and fully turbulent flow region (Re > 200), given that the Reynolds number values are reviewed as for flow through porous media [10]. Only the lowest volume flow rate value used in simulation covers a transitional flow, where there is either not fully developed turbulent flow or a combination of laminar and turbulent flow. The highest volume flow rate studies reach highly turbulent flow values.

Table 4. Reynolds Number Values for Each Numerical Study

Gyroid cell size	Volume flow rate, [m3/h]	Re	Gyroid cell size	Volume flow rate, [m3/h]	Re
20x20x20	0.5	77.26	50x20x20	0.5	92.03
	1.875	289.74		1.875	345.10
	3.25	502.22		3.25	598.18
	4.625	714.69		4.625	851.25
	6	927.17		6	1104.32
30x20x20	0.5	85.75	40x40x40	0.5	156.25
	1.875	321.58		1.875	585.94
	3.25	557.41		3.25	1015.63
	4.625	793.23		4.625	1445.33
	6	1029.06		6	1875.02
40x20x20	0.5	89.78	25x20x20	0.5	82.28
	1.875	336.69		1.875	308.55
	3.25	583.59		3.25	534.81
	4.625	830.49		4.625	761.08
	6	1077.40		6	987.35
30x30x30	0.5	113.84			
	1.875	426.90			
	3.25	739.96			
	4.625	1053.02			
	6	1366.08			

Figure 10 presents the obtained pressure loss and temperature difference between channels results of cell size study.

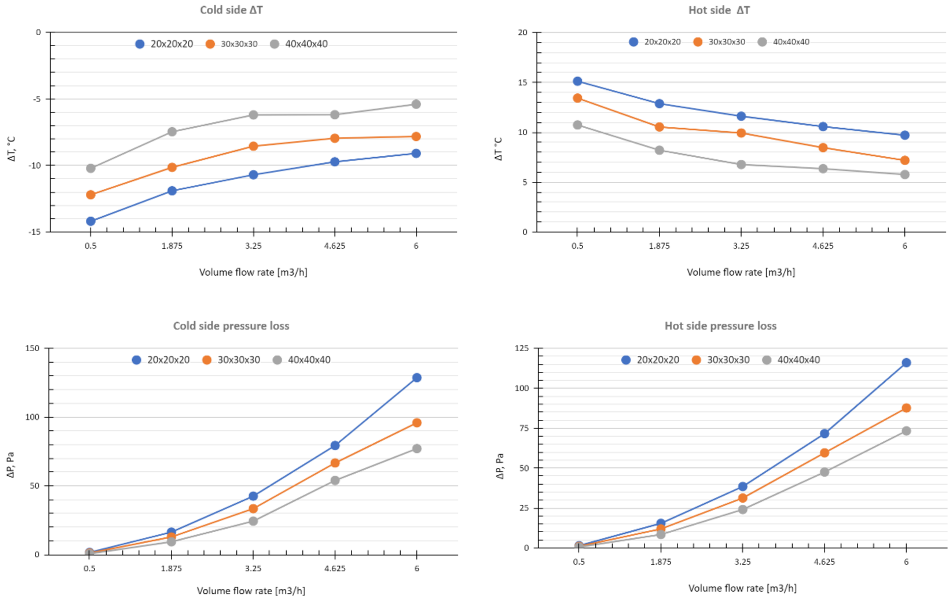

Fig. 10. Cell size study ΔT and pressure loss.

The obtained data indicate that by increasing the cell size the temperature difference between both hot and cold side channel inlets and outlets decreases similarly in the entire range of flow rates, being around 30–40 % lower when increasing cell size from 20x20x20 to 40x40x40. It can be concluded that the relationship between temperature difference and flow rate is consistent across all three studies. However, pressure loss values are close within lower flow rates of each study, but indicate a more rapid rise in pressure loss with a flow rate for each respective study. Thus, it can be concluded that the heat exchanger structure is the most efficient at low flow rates, with less internal friction in the flow, and by increasing the flow rate exponentially the pressure loss increases in the flow channels. Decreasing the cell size has a bigger effect on pressure loss in high volume flow regimes.

The obtained results of cell length in flow direction study are presented in Fig. 11. Cell length in flow direction is defined in the legend in mm. Cell width and height are 20 mm in all studies.

By increasing the length of the gyroid cells in the flow direction, it could be possible to significantly reduce the pressure loss in flow channels, while having a minimal effect on heat transfer. This could imply that gyroid structure can be improved for heat exchanger use, by increasing the length proportion of cells. In this study, by increasing the cell length two times (from 20 to 40 mm), pressure loss in each channel can be reduced from 71 % to 76 % in most of the volume flow rate range. At the same time, ΔT and, subsequently, the heat transfer between opposite flow channels is reduced by 6.6 % to 9.4 % in low volume flow rates, while achieving around 21.5 % reduction in higher flow rate ranges. Relations of graph lines of each study are similar to cell size study, but the results show bigger disproportionality between temperature difference and pressure loss results. Results show that proportional cells (20 mm in length) produce the steepest pressure loss curve while increasing the flow rate. By slightly increasing cell length, all further curves have a slower exponential increase, indicating a less pronounced rate of growth in pressure loss as the flow rate increases.

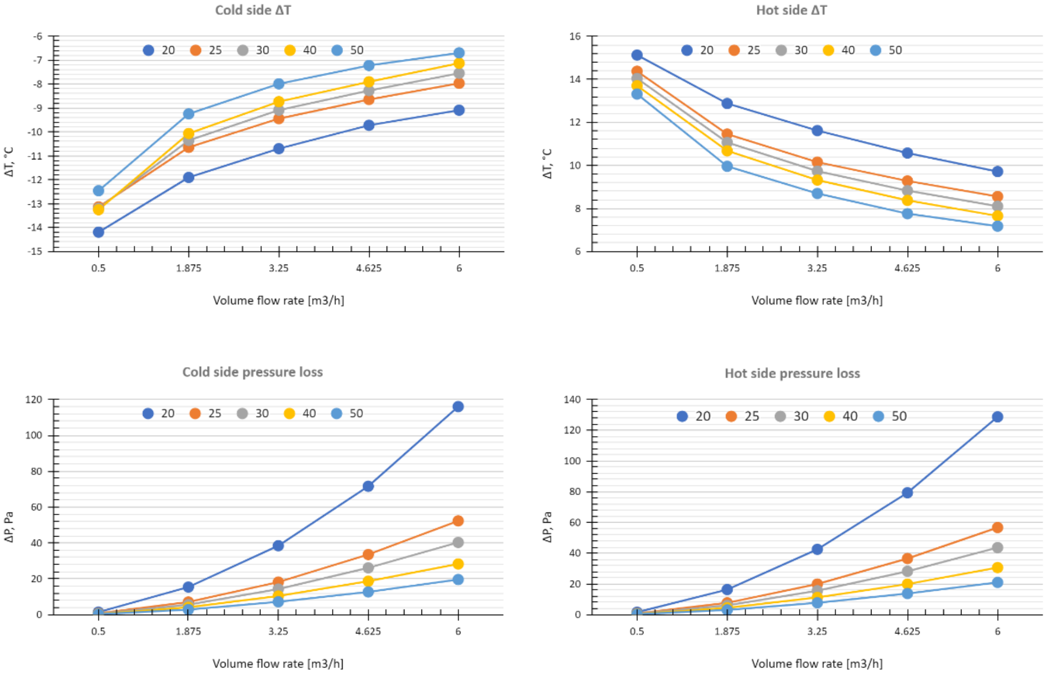

Fig. 11. Cell length in flow direction study ΔT and pressure loss.

4. CONCLUSIONS

TPMS air-to-air heat exchangers provide high design freedom for reaching compact sizes with a high surface area, low back pressure and high heat transfer. One of the main advantages is the production method used – 3D printing. While gyroid structure can be impossible to produce by traditional methods, printing can be used to manufacture even adjusted geometries, such as disproportionate cells, gradient TPMS structures and more. The main limitation is material used, as cheaper technologies can only use low heat transfer coefficient plastics, while metal printing can be too expensive to justify the cost. However, given that flow pressure for air-to-air heat exchangers in residential recuperators is relatively low, it can be bypassed by producing thin-walled heat exchangers, where the material conductive heat transfer coefficient does not play a huge role in heat transfer between the flow channel.

As discussed before, some cell sizes work well at low air flows, but can decrease the heat transfer efficiency at higher flow rates. Each of the studies had pressure loss rising exponentially by increasing the air flow rate and Re number, which means that the gyroid cell sizes must be carefully chosen for each heat exchanger application. The structure of flow channels creates transitional or turbulent flow regimes even with relatively low air flow speeds, which increases the heat transfer as well as pressure loss.

It can be concluded that disproportional gyroid heat exchanger, with cells longer in the flow direction, could achieve significantly lower pressure loss values, without losing much of the heat transfer characteristics. This can be very important for compact size air-to-air heat exchanger design for residential ventilation, as lower pressure loss means smaller and slower fans, which uses less power and produces less noise.

Although the manufacturability for complex TPMS structured heat exchangers is achievable by SLA, SLS, UV LCD printing or similar technologies, mass production of such parts can have its own problems. Printing one whole heat exchanger for a compact air recuperator with UV LCD printer requires multiple hours of printing, whereas traditional plate heat exchangers can be manufactured much faster. This would require large print farms for increasing the production output, which might hinder the ability to scale the manufacturing.

ACKNOWLEDGEMENTS

The present reasearch has been conducted by WeMPS Ltd. with the financial support from the Recovery and Resilience Facility (Project No. 5.1.1.2.i.0/1/22/A/CFLA/006), within the framowork of the project of Competence center for mechanical engineering (Mašīnbūves Kompetences centrs).

REFERENCES

1. von Schnering, H.G., & Nesper, R. (1991). Nodal Surfaces of Fourier Series: Fundamental Invariants of Structured Matter. *Zeitschrift* für *Physik B – Condensed Matter., 83* (3), 407–412.
2. Al-Ketan, O., Ali, M., Khalil, M., Rowshan, R., Khan, K. A., & Abu Al-Rub, R. K. (2021). Forced Convection Computational Fluid Dynamics Analysis of Architected and Three-Dimensional Printable Heat Sinks Based on Triply Periodic Minimal Surfaces. *Journal of Thermal Science and Engineering Applications, 13*, 1–14. DOI:10.1115/1.4047385
3. Cheng, Z., Li, X., Xu, R., & Jiang, P. (2021). Investigations on Porous Media Customized by Triply Periodic Minimal Surface: Heat Transfer Correlations and Strength Performance. *International Communications in Heat and Mass Transfer, 129*, 11–12. DOI:10.1016/j.icheatmasstransfer.2021.105713
4. Attarzadeh, R., Rovira, M., & Duwig, C. (2021). Design analysis of the “Schwartz D” Based Heat Exchanger: A Numerical Study. *International Journal of Heat and Mass Transfer, 177,* 6–7. DOI:10.1016/j.ijheatmasstransfer.2021.121415
5. Al-Ketan, O., Pelanconi, M., Ortona, A., & Abu Al-Rub, R. K. (2019). Additive Manufacturing of Architected Catalytic Ceramic Substrates Based on Triply Periodic Minimal Surfaces. *Journal of the American Ceramic Society, 102*, 6176–6193. DOI:10.1111/jace.16474
6. Femmer, T., Kuehne, A. J. C., & Wessling, M. (2015). Estimation of the Structure Dependent Performance of 3-D Rapid Prototyped Membranes. *Chemical Engineering Journal, 273,* 438–445. DOI:10.1016/j.cej.2015.03.029

7. Li, W., Yu, G., & Yu, Z. (2020). Bioinspired Heat Exchangers Based on Triply Periodic Minimal Surfaces for Supercritical CO2 Cycles. *Applied Thermal Engineering, 179*, 9–10. DOI:10.1016/j.applthermaleng.2020.115686.
8. Reynolds, B.W., Fee, C.J., Morison, K.R., & Holland, D.J. (2023). Characterisation of Heat Transfer within 3D Printed TPMS Heat Exchangers. *International Journal of Heat and Mass Transfer, 212*, 2–3.
9. Flow Simulation. (2020). *SolidWorks Flow Simulation 2020 Technical Reference.* Available at: https://www.cati.com/wp-content/uploads/2021/04/swflow2021-technical-reference.pdf
10. Rhodes, M. (2017). *Introduction to Particle Technology* (2nd ed.). Chichester, UK, John Wiley & Sons, Ltd. 30–42.

LATVIAN JOURNAL OF PHYSICS
AND TECHNICAL SCIENCES
2024, N 6

DOI: 10.2478/lpts-2024-0046

MECHANICAL AND THERMAL PROPERTIES OF NANOCOMPOSITES REINFORCED WITH PAN NANOFIBRE MATS

J. V. Sanchaniya*, S. P. Dobariya, I. Lasenko

Riga Technical University,
Faculty of Civil and Mechanical Engineering,
Institute of Mechanical and Biomedical Engineering,
6B Kipsala Str., Riga, LV-1048, LATVIA
*e-mail: jaymin.sanchaniya@rtu.lv

The integration of electrospun nanofibres into composite materials such as carbon fibre reinforced polymers (CFRP) and glass fibre reinforced polymers (GFRPs) has gained significant attention for enhancing their mechanical and thermal properties. This study focuses on the impact of incorporating polyacrylonitrile (PAN)-based nanofibres into an epoxy matrix to form multi-layered laminate composites. Our approach involved interleaving these orientated nanofibres within CFRP/GFRP matrices to investigate improvements in bulk material characteristics. The tensile and thermal properties of the resulting nanocomposites were thoroughly analysed. Thermogravimetric analysis (TGA) was employed to evaluate the thermal stability and degradation behaviour. In particular, nanocomposites exhibited an increase of 5–24 % in elastic modulus, aligning with predictions from analytical models. This research underscores the potential of PAN nanofibre mats for the development of lightweight, high-performance nanocomposites, offering a novel methodology for the enhancement of composite materials.

Keywords: *Mechanical properties, nanocomposite, PAN nanofibre mat, thermogravimetry (TGA).*

1. INTRODUCTION

The advent of electrospinning as a cost-effective method for producing nanofibres has ushered in a paradigm shift in material science research, particularly in the realm of carbon fibre reinforced polymers (CFRP) and Glass Fibre Reinforced Polymers (GFRP). Over the past decade, research has increasingly gravitated towards the integration of nanofibre mats into these composite materials. This growing interest is attributed to the compelling evidence that the interleaving of nanofibre mats significantly augments the mechanical and thermal attributes of CFRP/GFRP composites [1].

The strategic inclusion of nanofibre mats within laminated composites yields numerous benefits. A primary advantage is the marked improvement in delamination resistance [2], which is essential for the preservation of the structural integrity of composites. Furthermore, the impact tolerance of these materials shows substantial improvement, thereby bolstering their resilience against physical stresses and strains, a quality of paramount importance in applications subject to dynamic or unpredictable environmental forces.

Furthermore, the fracture and fatigue resistance of CFRP/GFRP composites is considerably reinforced through the introduction of nanofibre mats. This enhancement not only prolongs the useful life of the materials, but also reduces the frequency of necessary repairs or replacements. The interlaminar toughness and crack resistance also show significant improvements, contributing to the overall durability and reliability of these composite structures [3].

Another area of growing interest is the development of self-healing materials and nanofibrous materials with antibacterial properties with textiles [4]–[6]. Incorporation of nanofibre mats into composites is a gateway to pioneering materials capable of autonomously repairing damage, thereby extending their utility and functional lifespan.

Table 1 meticulously catalogues these enhancements, each improvement substantiated by pertinent references. This provides an exhaustive overview of the prevailing research in this domain, emphatically demonstrating the profound impact of nanofibre mats on the performance of composite materials. Table 1 also highlights the significance of integrating nanofibre mats, derived from various materials, into CFRP and GFRP. It elucidates how this integration materially enhances the mechanical and thermal properties of these composites, highlighting improvements in delamination resistance, impact and fracture tolerance, fatigue resistance, and interlaminar toughness and crack resistance.

Table 1. Enhancements in CFRP/GFRP Composites through Nanofibre Mat Interleaving

Application of nanofibre mats in CFRP/GFRP composites	References
Improving the delamination resistance	[7]–[11]
Enhancing the low impact tolerance	[7], [12]–[15]
Augmenting the fracture resistance	[12], [16]–[20]
Enhancing the fatigue resistance	[2], [8], [13], [16]
Improvement in thermal properties	[21]–[26]
Enhancement of mechanical properties	[22]–[31]
Improvement in interlaminar toughness	[32]–[39]
Development of self-healing composite materials	[40], [41]

Table 1 encapsulates the diverse applications of nanofibre mats in reinforcing CFRP and GFRP composites, as delineated in the literature. Each category of improvement is supported by a range of references, illustrating the breadth of research and corroborating the multifaceted enhancements attributed to the inclusion of nanofibre mats. This compilation provides a valuable resource for understanding the scope and depth of current advances in this field.

Notwithstanding these advances, investigations into the tensile strength and thermal properties of nanofibre interleaved composite laminates remain relatively unexplored. Although notable enhancements in tensile strength and thermal degradation resistance are observed with nanofibre mat interleaving, corroborative evidence for similar improvements in tensile strength for interleaved composites is limited. This underscores the need for more comprehensive research into the mechanical and thermal behaviours of nanofibre interleaved composite laminates, particularly in order to determine if this methodology can effectively mitigate one of the fundamental limitations of laminated composites.

The present research focuses on the influence of polyacrylonitrile (PAN) nanofibre mats on the mechanical and thermal properties of epoxy composites. Through the interleaving of various layers of nanofibre mats to fabricate layered structures, this study endeavours to discern their impact on the mechanical and thermal properties of nanocomposites.

2. MATERIALS AND METHODOLOGY

This study delves into the impact of polyacrylonitrile (PAN) nanofibre layers on laminated nanocomposite materials, employing a methodology that integrates the fabrication of electrospun nanofibres, mechanical testing, and thermal analysis.

In the fabrication of electrospun nanofibres, the materials used included PAN powder, with an average molecular weight of 150,000 and a CAS number of 25014-41-9, and N,N-dimethylformamide (DMF), a solvent with a purity of at least 99.8 % and a CAS number of 68-12-2. These materials were obtained from Sigma-Aldrich, Merck KGaA, Darmstadt, Germany. Additionally, the liquid resin epoxy and hardener, identified by the CAS number 964-67-8, were obtained from the Latwood Master razosanas komercfirma Ltd in Latvia. The PAN nanofibre mat was conducted in a manner similar to that previously described in the literature [42]–[45] and employed the hand lay-up method, as previously utilised by the author [25] for reinforced polyamide 6 reinforced nanocomposites. A detailed flow chart of the nanocomposite fabrication process is presented in Fig. 1.

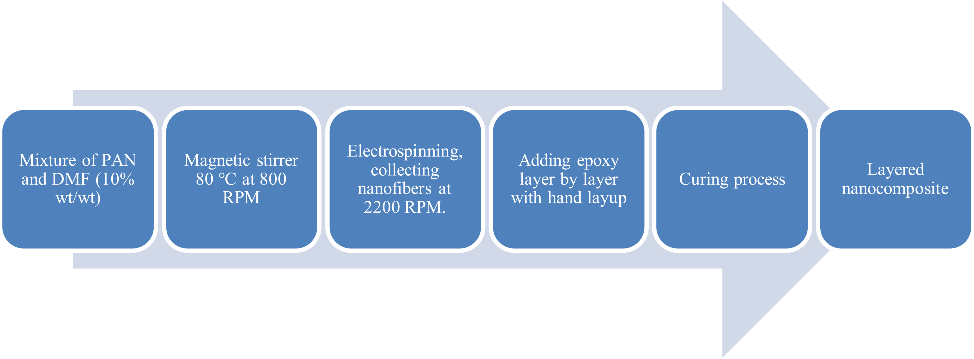

Fig. 1. Comprehensive schematic illustrating the fabrication process of the layered nanocomposite.

For mechanical testing, the tensile properties of the nanocomposites were evaluated using a Mecmesin Multi-Test 2.5-i tensile testing machine, equipped with a 25/250-N sensor, provided by PPT Group UK Ltd., Mecmesin, UK. The consistency and reliability of the results were ensured by conditioning the samples at room temperature according to ISO 139:1973 "Standard Environments for Conditioning and Testing," which stipulates a temperature of 21 ± 1 °C, a relative air humidity of 60 % and atmospheric pressure of 760 mm Hg. The sample dimensions adhered to the ASTM D882-18 standard, measuring 50 mm × 10 mm (length × width), with four measurements taken to accurately determine the tensile properties. The thickness of the nanofibre mats was precisely measured using a digital micrometre (range: 0–25 mm; Digimatic micrometre, MDC-25PX, code No. 293-240-30, serial No. 71912410, Mitutoyo, Japan). For the tensile testing, specimens were prepared both parallel to the nanofibre direction, facilitating testing in longitudinal directions. A specific paper template was used for sample preparation, and the samples were mounted on the tensile testing machine with double-sided thin scotch tape, followed by careful removal of the sides of the paper template. Figure 2 illustrates the tensile test specimen.

Fig. 2. Depiction of post-tensile nanocomposite samples.

The methodology further encompasses a systematic approach to classifying the nanocomposite specimens, which were composed of varying layers of PAN nanofibre mats interleaved within the epoxy matrix. These specimens were designated with specific labels: "CL1", "CL2", and "CL3". Each label corresponds to a distinct composite structure, with "CL1" representing a composite containing a single layer of nanofibre mat, "CL2" for a composite with two layers, and "CL3" for those comprising three layers of nanofibre mats. The initialism "CL" in these designations stands for "Composite Layer", followed by a numeral denoting the number of nanofibre layers incorporated within the composite. This classification system facilitated a structured and precise evaluation of the mechanical and thermal properties of the nanocomposites, allowing for a clear comparison between the varying compositions and structures.

For statistical significance the Halpin-Tsai model was applied to the PAN nanofibre-reinforced epoxy composites, with its predictions compared with experimental data to validate its effectiveness in estimating the mechanical properties of these composites.

$$E_c = \frac{E_m(1 + \zeta\eta V_f)}{(1 - \eta V_f)}, \tag{1}$$

where

E_c – the effective modulus of the composite material, MPa.

E_m – the modulus of the matrix material, MPa.

V_f – the volume fraction of the fibres.

η – the efficiency parameter, which is a function of the aspect ratio of the fibres.

ζ – the reinforcement factor, which relates the modulus of the fibre to the modulus of the matrix.

The Halpin-Tsai model, useful for composites with a high aspect ratio of reinforcement fibres, assumes perfect bonding between fibres and matrix, treating the composite as a homogenised material.

Thermal properties were evaluated by thermogravimetric analysis (TGA), using a TG 209 F1 Libra® thermomicrobalance from NETZSCH, Germany. Samples, weighing between 5 and 6 mg, were placed in Al_2O_3 crucibles and subjected to a temperature range of 20 °C to 800 °C at a heating rate of 10 °C/min, under an inert nitrogen atmosphere with a flow rate of 30 ml/min. Precise weight measurements of the samples were carried out using a laboratory scale from KERN&Sohn GmbH, Germany. The TGA provided insightful data on the thermal stability and decomposition characteristics of the composite materials, with a focus on identifying specific temperatures at which significant mass loss occurred, thus indicating the thermal degradation points of the composite material.

3. RESULTS AND DISCUSSION

The results obtained from the tensile testing of PAN nanofibre mats, pure epoxy, and nanocomposites with varying layers of PAN nanofibre are instrumental in understanding the mechanical behaviour of these materials.

Figure 3 shows the tensile strength and elongation properties of PAN nanofibre mats. The data indicate that the PAN nanofibre mat exhibits a maximum tensile strength of approximately 8.5 ± 0.5 MPa and an elastic modulus of around 920 ± 15 MPa. Furthermore, the material demonstrates an elongation at break of 5.4 ± 0.1 %, suggesting a degree of flexibility inherent in the PAN nanofibre mats.

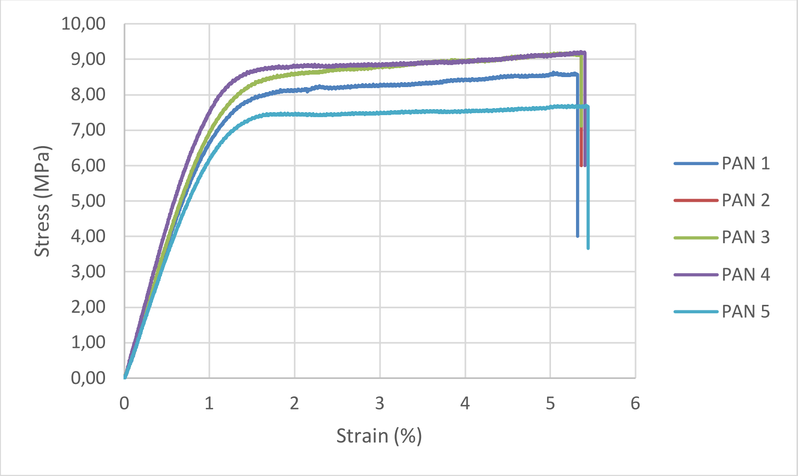

Fig. 3. Results of PAN nanofibre mats.

Figure 4 shifts the results of the focus to the tensile test for pure epoxy. The results reveal that pure epoxy has a higher maximum tensile strength of 12.8 ± 2 MPa compared to the PAN nanofibre mats, although with a lower elastic modulus of 580 ± 12 MPa. The elongation at break for pure epoxy is recorded at 5.1 ± 0.2 %, which is closely aligned with the values observed for the PAN nanofibre mats. In particular, sample Ep 1 was excluded from the analysis due to measurement error.

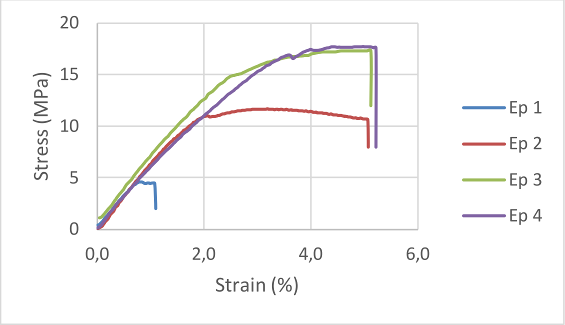

Fig. 4. Results of pure epoxy.

The tensile properties of nanocomposites with different layers of PAN nanofibre are detailed in Figs. 5–7. The single layer nanocomposite, as shown in Figure 5, exhibits a maximum tensile strength of 12.5 ± 2 MPa and an elastic modulus of 610 ± 15 MPa, in conjunction with an elongation at break of 2.1 ± 0.2 %. On the contrary, the two-layer nanocomposite shown in Fig. 6 shows an increase in tensile strength to 16 ± 3 MPa and elastic modulus to 650 ± 18 MPa, with an elongation at break of 3 ± 0.3 %. The three-layer nanocomposite, presented in Fig. 7, further enhances these properties, demonstrating a maximum tensile strength of 18 ± 2 MPa, an elastic modulus of 720 ± 12 MPa, and an elongation at break of 3 ± 0.5 %.

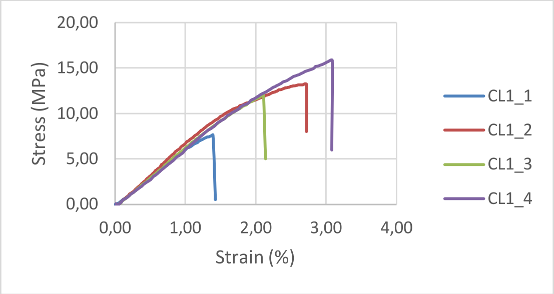

Fig. 5. Tensile test results for single-layer PAN nanofibre-epoxy composite.

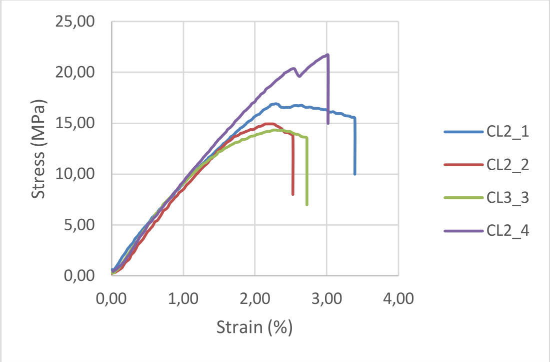

Fig. 6. Results of tensile testing on a two-layer PAN nanofibre-epoxy composite.

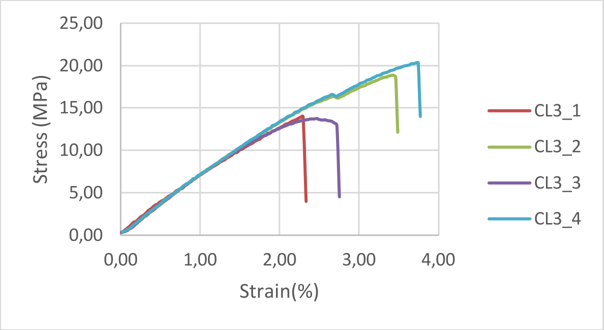

Fig. 7. Results of tensile properties for three-layer PAN nanofibre-epoxy composite.

Table 2 offers a concise summary of the mechanical properties of all the materials tested, including PAN nanofibre mats, pure epoxy, and various layered nanocomposites. Table 1 enables an efficient comparison across different materials, underscoring the incremental improvements in tensile strength and elastic modulus brought about by the addition of PAN nanofibre layers, while moderately affecting their elongation at break.

Table 2. Summary of Mechanical Properties: PAN Nanofibre Mats, Pure Epoxy, and Layered Nanocomposites

Samples	Thickness, t (μm)	Tensile strength σ at break (MPa)	Young's modulus, E (MPa)	Elongation at break, ε at break (%)
PAN	74 ± 10	8.5 ± 0.5	920 ± 15	5.4 ± 0.1
EP	154 ± 7	12.8 ± 2	580 ± 12	5.1 ± 0.2
CL1	200 ± 11	12.5 ± 2	610 ± 15	2.1 ± 1
CL2	270 ± 15	16 ± 3	650 ± 18	3 ± 0.3
CL3	335 ± 18	18 ± 2	720 ± 12	3 ± 0.5

The findings of these tests and analyses highlight that the incorporation of PAN nanofibre mats into epoxy composites significantly improves their mechanical properties, particularly in terms of strength and stiffness. This enhancement in material properties with the addition of nanofibre layers illuminates the potential of nanofibre reinforcement in the development of advanced material applications.

The study also incorporates the application of the Halpin-Tsai micromechanical model to calculate the elastic modulus of the nanocomposites. This model uses specific experimental values, including the modulus of the epoxy matrix (E_E) recorded at 580 MPa and the modulus of the PAN nanofibre mat (E_{PAN}) recorded at 920 MPa.

Upon integrating these values into the model, the resultant calculations for the elastic modulus of the nanocomposites with varying layers of PAN nanofibre are as follows:

- for the composite with one layer of PAN nanofibre mat (E_{CL1}), the calculated elastic modulus is 610 MPa;
- for the two-layer composite (E_{CL2}), the modulus increases to 635 MPa;
- the three-layer composite (E_{CL3}) exhibits a further increase in the elastic modulus, reaching 670 MPa.

These results demonstrate a progressive increase in the stiffness of the composite material with the incorporation of additional layers of PAN nanofibre mats. The calculated values reflect the enhanced mechanical properties of the nanocomposites, confirming the reinforcement efficacy of the PAN nanofibres. This progression aligns with the predictions of the Halpin-Tsai model, highlighting its applicability in estimating the mechanical properties of fibre-reinforced composites.

Figure 8 presents the results of thermogravimetric analysis (TGA) for pure epoxy. The analysis elucidates that the maximum degradation temperature of pure epoxy is recorded at 373.5 °C. This temperature is indicative of the point at which the most significant thermal decomposition occurs, providing an insight into the thermal stability of the epoxy.

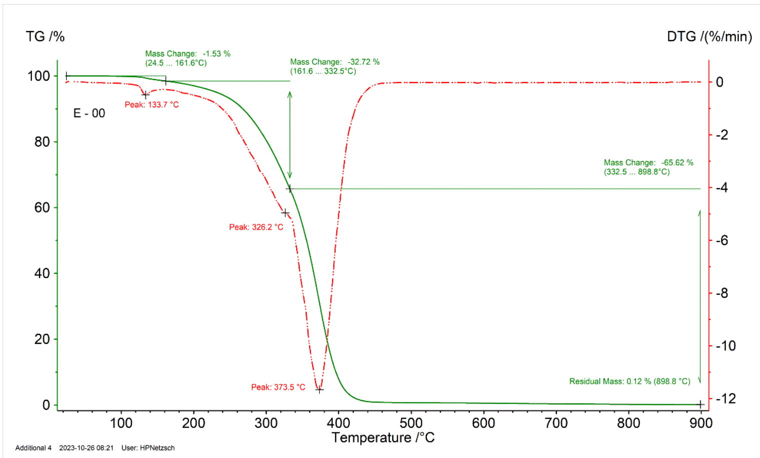

Fig. 8. TGA and DTG graphs of pure epoxy.

Proceeding with the TGA studies, Fig. 9 examines the thermal degradation of the single-layer reinforced nanocomposite. In particular, the peak degradation of this composite was observed at a slightly reduced temperature of 370.5 °C. This marginal decrease, in comparison with pure epoxy, suggests that the incorporation of a single nanofibre layer subtly influences the thermal stability of the composite.

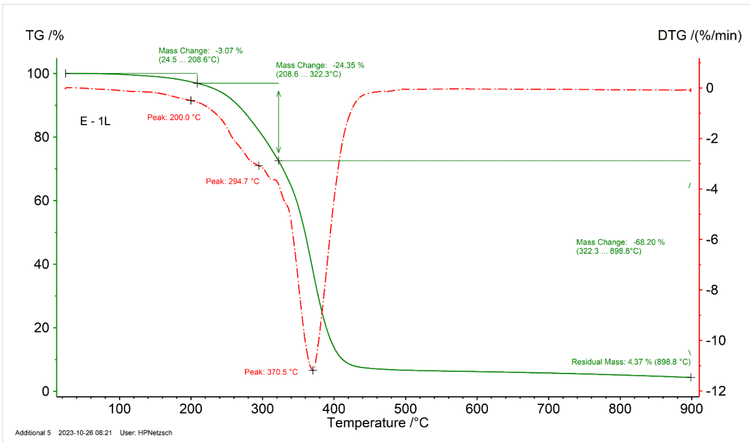

Fig. 9. TGA and DTG graph of the PAN nanofibre reinforced composite.

In the context of the double layer reinforced nanocomposite, as demonstrated in Fig. 10, the maximum degradation temperature was found to be 369.4 °C. This further decline in the peak degradation temperature with the addition of another layer of nanofibres underscores a more pronounced impact on the thermal properties of the composite.

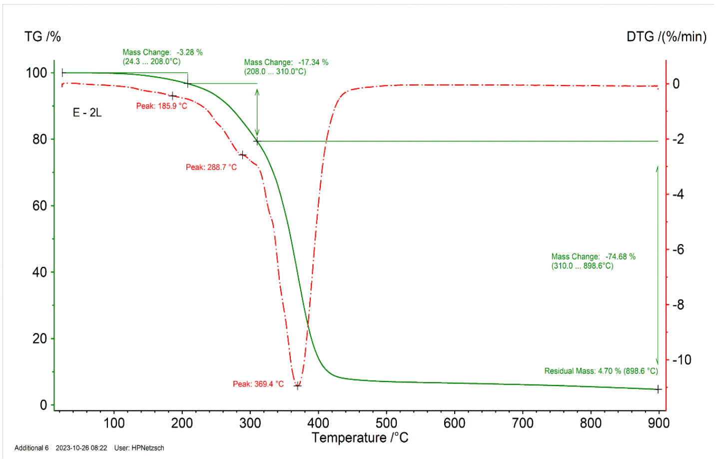

Fig. 10. TGA and DTG graphs of double-layer PAN nanofibre reinforced composite.

Extending this thermal analysis to the reinforced three-layer nanocomposite in Fig. 11, the degradation peak occurs at a lower temperature of 364.2 °C. This consistent reduction in the degradation temperature with each additional layer of nanofibres highlights the significant effect of nanofibre reinforcement on the thermal behaviour of the composites.

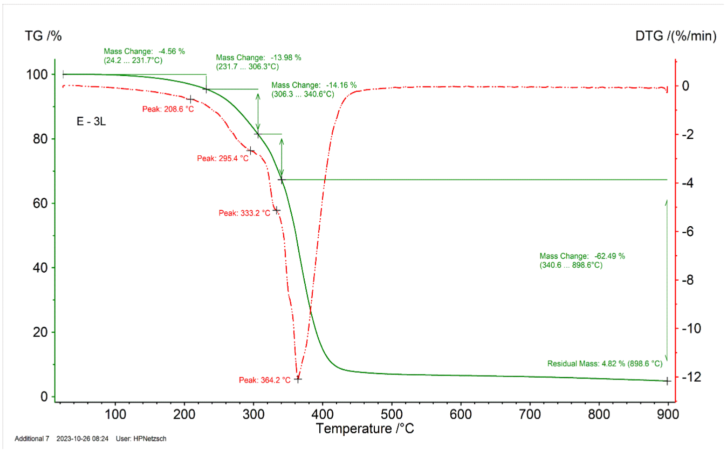

Fig. 11. TGA and DTG graph of three-layer PAN nanofibre reinforced composite.

Figure 12 offers a comparative TGA analysis of all nanocomposites alongside pure epoxy. This juxtaposition provides a lucid visual depiction of the impact of nanofibre layer addition on the thermal degradation behaviour of epoxy composites. It facilitates a straightforward comparison between the thermal stability of the pure epoxy and that of the nanocomposites, accentuating the role of nanofibre reinforcement in modifying the thermal response.

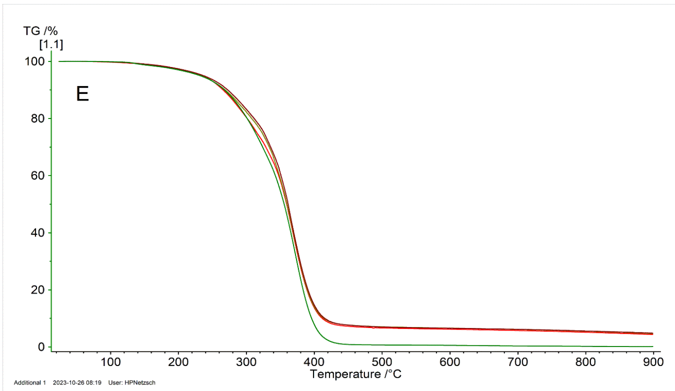

Fig. 12. Comparative thermogravimetric analysis: Nanocomposites versus pure epoxy (highlighted in green).

The thermogravimetric analyses conducted are pivotal in delineating the thermal properties of the nanocomposite materials. The gradual decrease in the peak degradation temperature with the incremental addition of nanofibre layers clearly manifests the influence of nanofibres reinforcement on the thermal behaviour of epoxy composites.

These analyses are instrumental in optimising the design of nanofibre-reinforced composites for specific applications where thermal properties are crucial. The findings emphasise the necessity of comprehending the interactions between the matrix material and the reinforcing nanofibres, since these interactions are determinants of the composite's overall performance and applicability in various scenarios.

Incorporation of the Halpin-Tsai model into our analysis provides a more nuanced understanding of the mechanical enhancements brought about by the inclusion of PAN nanofibre mats in epoxy composites. The predictions of the model, corroborated by our experimental findings, underscore the significant role these nanofibres play in increasing the stiffness of the composites. Notably, the observed progressive increase in elastic modulus with the addition of more nanofibre layers is consistent with theoretical expectations and is experimentally validated, affirming the reinforcing efficacy of the PAN nanofibres.

Tensile strength tests further reinforce the notion that PAN nanofibre mats significantly bolster the mechanical attributes of epoxy composites. The evident increase in tensile strength and elastic modulus with each additional nanofibre layer underscores the effectiveness of this reinforcement strategy, which is also noted in this research [3] the research on composite laminates enhanced with electrospun thermoplastic nanofibres is still very limited and a thorough understanding of the toughening mechanism is still missing. This article provides thorough insights into the micromechanisms that lead to the interlaminar toughening of carbon/epoxy composite laminates interleaved with electrospun polyamide nanofibrous veils. The main mechanism leading to a higher interlaminar fracture toughness, both under Mode I and Mode II loading conditions, was the bridging of (micro. However, this improvement in strength comes with a concomitant decrease in ductility, as evidenced by the reduced elongation at break. This trade-off is a common feature in composite materials, where the infusion of reinforcing elements typically enhances strength at the expense of flexibility.

Thermogravimetric analysis (TGA) reveals an intriguing aspect of the thermal properties of the nanocomposites. While pure epoxy exhibits a higher thermal degradation temperature, the addition of PAN nanofibres induces a reduction in this temperature. This phenomenon suggests a possible alteration in the thermal degradation behaviour of the epoxy matrix upon introduction of the nanofibres. The consistent reduction in the maximum degradation temperature with each layer of nanofibres could imply a cumulative effect of nanofibre reinforcement on the thermal stability of the composites. This observation warrants a deeper investigation into the thermal interaction mechanisms between the epoxy matrix and PAN nanofibres.

4. CONCLUSIONS

This study provides a comprehensive analysis of the mechanical and thermal properties of PAN nanofibre-reinforced epoxy composites, enriched by the application of the Halpin-Tsai model. The progressive increase in stiffness with the addition of more nanofibre layers, as predicted by the model and confirmed by experimental results, highlights the effectiveness of nanofibre reinforcement in improving the mechanical properties (5–24 %) of composites.

The findings of tensile testing and thermogravimetric analyses demonstrate the potential of these composites in applications requiring enhanced mechanical strength and modified thermal properties. The gradual decrease in the maximum degradation temperature with increased nanofibre layers, though warranting further investigation, provides valuable insights into the thermal behaviour of these materials.

In conclusion, the study contributes significantly to the field of composite materials, offering vital information on the interplay between mechanical strength, flexibility, and thermal stability in nanofibre-reinforced composites. Future research should focus on a deeper exploration of the interfacial interactions between the matrix and the reinforcing fibres and the scalability of these composites for practical applications.

ACKNOWLEDGEMENTS

The research has been supported by the Doctoral Grant Programme of Riga Technical University.

REFERENCES

1. Bahrami, A. Cordenier, F., Van Velthem, P., Ballout, W., Pardoen, T., Nysten, B., & Bailly, C. (2016). Synergistic Local Toughening of High Performance Epoxy-Matrix Composites Using Blended Block Copolymer-Thermoplastic Thin Films. *Compos. Part A Appl. Sci. Manuf.*, *91*, 398–405. DOI: 10.1016/J.COMPOSITESA.2016.08.038

2. Brugo, T., Minak. G., Zucchelli, A., Yan, X. T., Belcari, J., Saghafi, H., & Palazzetti, R. (2017). Study on Mode I Fatigue Behaviour of Nylon 6,6 Nanoreinforced CFRP Laminates. *Compos. Struct.*, *164*, 51–57. DOI: 10.1016/j.compstruct.2016.12.070
3. Daelemans, L., van der Heijden, S., De Baere, I., Rahier, H., Van Paepegem, W., & De Clerck, K. (2015). Nanofibre Bridging as a Toughening Mechanism in Carbon/Epoxy Composite Laminates Interleaved with Electrospun Polyamide Nanofibrous Veils. *Compos. Sci. Technol.*, *117*, 244–256. DOI: 10.1016/j.compscitech.2015.06.021.
4. Sanchaniya, J.-V., Kanukuntla, S.-P., Modappathi, P., & Macanovskis, A. (2022). Mechanical Behaviour Numerical Investigation of Composite Structure, Consisting of Polymeric Nanocomposite Mat and Textile. *21st Int. Sci. Conf. Eng. Rural Dev. Proc.*, *21*, 720–726. DOI: 10.22616/erdev.2022.21.tf225
5. Grauda, D., Butkauskas, D., Vyšniauskienė, R., Rančelienė, V., Krasņevska, N., Miķelsone, A., … & Ļašenko, I. (2023). Establishment of Biotesting System to Study Features of Innovative Multifunctional Biotextile. *Proc. Latv. Acad. Sci. Sect. B Nat. Exact, Appl. Sci.*, *77*, 3–4, 186–192. DOI: 10.2478/prolas-2023-0026
6. Asfand, N., & Daukantiene, V. (2023). Study of the Tensile and Bending Stiffness Behavior of Antistatic and Antibacterial Knitted Fabrics. *Fibres Text. East. Eur.*, *31* (3), 1–9. DOI: 10.2478/ftee-2023-0026
7. Ravindran, A. R., Ladani, R. B., Kinloch, A. J., Wang, C. H., & Mouritz, A. P. (2021). Improving the Delamination Resistance and Impact Damage Tolerance of Carbon Fibre-Epoxy Composites Using Multi-Scale Fibre Toughening. *Compos. Part A Appl. Sci. Manuf.*, *150*, 106624. DOI: 10.1016/j.compositesa.2021.106624
8. Mohammadi, R., Akrami, R., Assaad, M., Nasor, M., Imran, A., & Fotouhi, M. (2023). Polysulfone Nanofibre-Modified Composite Laminates: Investigation of Mode-I Fatigue Behavior and Damage Mechanisms. *Theor. Appl. Fract. Mech.*, *127*, 104078. DOI: 10.1016/j.tafmec.2023.104078
9. Daelemans, L., Kizildag, N., Van Paepegem, W., D'hooge, D. R., & De Clerck, K. (2019). Interdiffusing Core-Shell Nanofibre Interleaved Composites for Excellent Mode I and Mode II Delamination Resistance. *Compos. Sci. Technol.*, *175*, 143–150, 2019. DOI: 10.1016/j.compscitech.2019.03.019
10. MacCaferri, E., Mazzocchetti, L., Benelli, T., Brugo, T. M., Zucchelli, A., & Giorgini, L. (2022). Self-Assembled NBR/Nomex Nanofibres as Lightweight Rubbery Nonwovens for Hindering Delamination in Epoxy CFRPs. *ACS Appl. Mater. Interfaces*, *14* (1), 1885–1899. DOI: 10.1021/acsami.1c17643.
11. Ortolani, J., Maccaferri, E., Mazzocchetti, L., Benelli, T., Brugo, T. M., Zucchelli, A., Giorgini, L. (2022). Polyamide Nanofibres Impregnated with Nitrile Rubber for Enhancing CFRP Delamination Resistance. *Macromol. Symp.*, *405* (1), 1–3. DOI: 10.1002/masy.202100232
12. Ladani, R. B., Wu, S., Kinloch, A. J., Ghorbani, K., Zhang, J., Mouritz, A. P., & Wang, C. H. (2016). Multifunctional Properties of Epoxy Nanocomposites Reinforced by Aligned Nanoscale Carbon. *Mater. Des.*, *94*, 554–564. DOI: 10.1016/j.matdes.2016.01.052
13. Ladani, R. B., Wu, S., Kinloch, A. J., Ghorbani, K., Mouritz, A. P., & Wang, C. H. (2017). Enhancing Fatigue Resistance and Damage Characterisation in Adhesively-Bonded Composite Joints by Carbon Nanofibres. *Compos. Sci. Technol.*, *149*, 116–126. DOI: 10.1016/j.compscitech.2017.06.018
14. Daelemans, L., Cohades, A., Meireman, T., Beckx, J., Spronk, S., Kersemans, M., … & De Clerck, K. (2018). Electrospun Nanofibrous Interleaves for Improved Low Velocity Impact Resistance of Glass Fibre Reinforced Composite Laminates. *Mater. Des.*, 141, 170–184. DOI: 10.1016/j.matdes.2017.12.045
15. Garcia, C., Trendafilova, I., & Zucchelli, A. (2018). The Effect of Polycaprolactone Nanofibres on the Dynamic and Impact Behavior of Glass Fibre Reinforced Polymer Composites. *J. Compos. Sci.*, *2* (3), 1–12. DOI: 10.3390/jcs2030043

16. Ladani, R. B., Bhasin, M., Wu, S., Ravindran, A. R., Ghorbani, K., Zhang, J., … & Wang, C. H. (2018). Fracture and Fatigue Behaviour of epoxy Nanocomposites Containing 1-D and 2-D Nanoscale Carbon Fillers. *Eng. Fract. Mech.*, *203*, 102–114. DOI: 10.1016/j.engfracmech.2018.04.033
17. Ladani, R. B., Wu, S., Zhang, J., Ghorbani, K., Kinloch, A. J., Mouritz, A. P., & Wang, C. H. (2017). Using Carbon Nanofibre Sensors for In-situ Detection and Monitoring of Disbonds in Bonded Composite Joints. *Procedia Eng.*, *188*, 362–368. DOI: 10.1016/j.proeng.2017.04.496
18. Nimbagal, V., Banapurmath, N. R., Umarfarooq, M. A., Revankar, S., Sajjan, A. M., Soudagar, M. E. M., … & Elfasakhany, A. (2023). Mechanical and fracture properties of carbon nano fibers/Short Carbon Fiber Epoxy Composites. *Polym. Compos.*, *44* (7), 3977–3989. DOI: 10.1002/pc.27371
19. Maccaferri, E., Mazzocchetti, L., Benelli, T., Brugo, T. M., Zucchelli, A., & Giorgini, L. (2020). Rubbery Nanofibrous Interleaves Enhance Fracture Toughness and Damping of CFRP Laminates. *Mater. Des.*, *195*, 109049. DOI: 10.1016/j.matdes.2020.109049
20. Maccaferri, E., Mazzocchetti, L., Benelli, T., Brugo, T. M., Zucchelli, A., & Giorgini, L. (2021). Rubbery-Modified CFRPS with Improved Mode I Fracture Toughness: Effect of Nanofibrous Mat Grammage and Positioning on Tanδ Behaviour. *Polymers (Basel).*, *13* (12). DOI: 10.3390/polym13121918
21. Gavande, V., Nagappan, S., Seo, B., Cho, Y. S., & Lee, W. K. (2023). Transparent Nylon 6 Nanofibres-Reinforced Epoxy Matrix Composites with Superior Mechanical and Thermal Properties. *Polym. Test.*, *122*, 108002. DOI: 10.1016/j.polymertesting.2023.108002
22. Le, B., Fu, G., Khaliq, J., Huo, D., & Shyha, I. (2023). Experimental Investigation on Thermomechanical Properties and Micro-Machinability of Carbon Nanofibre Reinforced Epoxy Nanocomposites. *J. Manuf. Process.*, *99*, 781–793, 2023. DOI: 10.1016/j.jmapro.2023.05.080
23. Liu, J., Lu, S., Liu, X., Wang, B., Yu, Z., & Che, C. (2023). Effect of Natural Indocalamus Leaf Addition on the Mechanical Properties of Epoxy and Epoxy-Carbon Fiber Composites. *E-Polymers*, *23* (1). DOI: 10.1515/epoly-2023-0039
24. Guadagno, L., Naddeo, C., & Raimondo, M. (2023). Thermal, Mechanical and Electrical Performance of Structural Epoxy Resins Filled with Carbon Nanofibres. *J. Therm. Anal. Calorim.*, *148* (23), 13095–13106. DOI: 10.1007/s10973-023-12521-6
25. Lasenko, I., Sanchaniya, J. V., Kanukuntla, S. P., Ladani, Y., Viluma-Gudmona, A., Kononova, O., … & Selga, T. (2023). The Mechanical Properties of Nanocomposites Reinforced with PA6 Electrospun Nanofibres. *Polymers (Basel).*, *15* (3). DOI: 10.3390/polym15030673
26. Erdal, M. O., Yazman, Ş., Gemi, L., & Yapici, A. (2018). The Effect of Nonwoven Electrospun PAN Nanofibre Mat on Mechanical and Thermal Properties of Epoxy Composites. *Süleyman Demirel Üniversitesi Fen Bilim. Enstitüsü Derg.*, *22* (2), p. 528. DOI: 10.19113/sdufbed.81545
27. Wable, V., Biswas, P. K., Moheimani, R., Aliahmand, N., Omole, P., Siegel, A. P., … & Dalir, H. (2021). Engineering the Electrospinning of MWCNTs/Epoxy Nanofibre Scaffolds to Enhance Physical and Mechanical Properties of CFRPs. *Compos. Sci. Technol.*, *213*, 108941. DOI: 10.1016/j.compscitech.2021.108941
28. Simunin, M. M., Voronin, A. S., Fadeev, Yu. V., Dobrosmyslov, S. S., Kuular, A. A., … & Khartov, S. V. (2023). Influence of the Addition of Alumina Nanofibres on the Strength of Epoxy Resins. *Materials (Basel).*, *16* (4), 1–10. DOI: 10.3390/ma16041343
29. Wang, Y., Sun, Z., Yin, P., Qu, R., Zhang, Y., & Sun, C. (2023). Preparation and Mechanical Properties of UV-Curable Epoxy Acrylate/Modified Aramid Nanofibre Nanocomposite Films. *Nanomaterials*, *13* (22), 2960. DOI: 10.3390/nano13222960

30. Maccaferri, E., Mazzocchetti, L., Benelli, T., Ortolani, J., Brugo, T. M., Zucchelli, A., & Giorgini, L. (2022). Is Graphene Always Effective in Reinforcing Composites? The Case of Highly Graphene-Modified Thermoplastic Nanofibres and Their Unfortunate Application in CFRP Laminates. *Polymers (Basel).*, *14* (24), 5565. DOI: 10.3390/polym14245565
31. Santos, P., Silva, A. P., & Reis, P. N. B. (2023). Effect of Carbon Nanofibres on the Viscoelastic Response of Epoxy Resins. *Polymers (Basel).*, *15* (4). DOI: 10.3390/polym15040821
32. Wu, S., Ladani, R. B., Ravindran, A. R., Zhang, J., Mouritz, A. P., Kinloch, A. J., & Wang, C. H. (2017). Aligning Carbon Nanofibres in Glass-Fibre/Epoxy Composites to Improve Interlaminar Toughness and Crack-Detection Capability. *Compos. Sci. Technol.*, *152*, 46–56. DOI: 10.1016/j.compscitech.2017.09.007
33. Ravindran, A. R., Ladani, R. B., Wu, S., Kinloch, A. J., Wang, C. H., & Mouritz, A. P. (2018). Multi-Scale Toughening of Epoxy Composites via Electric Field Alignment of Carbon Nanofibres and Short Carbon Fibres. *Compos. Sci. Technol.*, *167*, 115–125. DOI: 10.1016/j.compscitech.2018.07.034
34. Daelemans, L., Verschatse, O., Heirman, L., Van Paepegem, W., & De Clerck, K. (2021). Toughening Mechanisms Responsible for Excellent Crack Resistance in Thermoplastic Nanofibre Reinforced Epoxies through In-situ optical and Scanning Electron Microscopy. *Compos. Sci. Technol.*, *201*, 108504. doi: 10.1016/j.compscitech.2020.108504
35. Minosi, S., Cocchi, D., Maccaferri, E., Pirondi, A., Zucchelli, A., Mazzocchetti, L., … & Campanini, F. (2021). Exploitation of Rubbery Electrospun Nanofibrous Mat for Fracture Toughness Improvement of Structural Epoxy Adhesive Bonded Joints. *J. Adv. Join. Process.*, *3*, 100050. DOI: 10.1016/j.jajp.2021.100050
36. Saghafi, H., Palazzetti, R., Heidary, H., Brugo, T. M., Zucchelli, A., & Minak, G. (2020). Toughening Behavior of Carbon/Epoxy Laminates Interleaved by PSF/PVDF Composite Nanofibres. *Appl. Sci.*, *10* (16), 1–12. DOI: 10.3390/app10165618
37. Saghafi, H., Nikbakht, A., Mohammadi, R., & Zarouchas, D. (2021). The Thickness Effect of PSF Nanofibrous Mat on Fracture Toughness of Carbon/Epoxy Laminates. *Materials (Basel).*, *14* (13). DOI: 10.3390/ma14133469
38. Santos, P., Silva, A. P., & Reis, P. N. B. (2023). Effect of Carbon Nanofibres on the Strain Rate and Interlaminar Shear Strength of Carbon/Epoxy Composites. *Materials (Basel)*, *16* (12). DOI: 10.3390/ma16124332
39. Maccaferri, E., Donne, M. D., Mazzocchetti, L., Benelli, T., Brugo, T. M., Zucchelli, A., & Giorgini, L. (2022). Rubber-Enhanced Polyamide Nanofibres for a Significant Improvement of CFRP Interlaminar Fracture Toughness. *Sci. Rep.*, *12* (1), 1–16. DOI: 10.1038/s41598-022-25287-y
40. Torre-Muruzabal, A., Daelemans, L., Van Assche, G., De Clerck, K., & Rahier, H. (2016). Creation of a Nanovascular Network by Electrospun Sacrificial Nanofibres for Self-Healing Applications and its Effect on the Flexural Properties of the Bulk Material. *Polym. Test.*, *54*, 78–83. DOI: 10.1016/j.polymertesting.2016.06.026
41. Brugo, T. M., Maccaferri, E., Cocchi, D., Mazzocchetti, L., Giorgini, L., Fabiani, D., & Zucchelli, A. (2021). Self-Sensing Hybrid Composite Laminate by Piezoelectric Nanofibres Interleaving. *Compos. Part B Eng.*, *212*, 108673. DOI: 10.1016/j.compositesb.2021.108673
42. Sanchaniya, J. V., Lasenko, I., Kanukuntala, S. P., Smogor, H., Viluma-Gudmona, A., Krasnikovs, A., … & Gobins, V. (2023). Mechanical and Thermal Characteristics of Annealed-Oriented PAN Nanofibres. *Polymers (Basel)*, *15* (15), 3287. DOI: doi.org/10.3390/polym15153287
43. Sanchaniya, J. V., Lasenko, I., Kanukuntla, S. P., Mannodi, A., Viluma-Gudmona, A., & Gobins, V. (2023). Preparation and Characterization of Non-Crimping Laminated Textile Composites Reinforced with Electrospun Nanofibres. *Nanomaterials*, *13* (13), 1949. DOI: 10.3390/nano13131949

44. Sanchaniya, J. V., Lasenko, I., Gobins, V., & Kobeissi, A. (2024). A Finite Element Method for Determining the Mechanical Properties of Electrospun Nanofibrous Mats. *Polym.*, *16* (6), 852. DOI: 10.3390/polym16060852
45. Sanchaniya, J. V., Lasenko, I., Vijayan, V., Smogor, H., Gobins, V., Kebeissi, A., … & Goljandin, D. (2024). A Novel Method to Enhance the Mechanical Properties of Polyacrylonitrile Nanofibre Mats: An Experimental and Numerical Investigation. *Polymers (Basel)*, 16 (7), 992. DOI: 10.3390/polym16070992

LATVIAN JOURNAL OF PHYSICS
AND TECHNICAL SCIENCES
2024, N 6

DOI: 10.2478/lpts-2024-0047

OPERATIONAL MANAGEMENT OF TECHNOLOGICAL PROCESSES FOR PREPARING AIRCRAFT FOR DEPARTURE AT THE AIRPORT AS A MULTI-CRITERIA TASK

A. Zabirov*, J. Soldatova, Z. Zabirov, A. Shestakov

Institute of Aeronautics, Riga Technical University,
6B Ķīpsalas Str., Riga, LV-1048, LATVIA
*e-mail: anvarzabirov@yahoo.com

Analysis of the statistics on the regularity of aircraft departures from the airport shows that one of the reasons for delays is poor operational management, leading to deviations from established norms in the timing of individual technological operations preparing aircraft for departure. This article presents an approach to solving this problem, which is considered a multi-criteria task. To address it, an imitation model in the form of a complex of modules has been developed. A corresponding algorithm for the functioning of each module has been devised. To ensure the necessary conformity of the model to real conditions, a check of the technological process variables for stochasticity has been conducted based on daily flight plans of the airport, using Wilcoxon and Smirnov-Kolmogorov criteria. Based on the timing of the duration characteristics of individual technological operations for servicing flights of different aircraft types under various conditions, a "Random Variable Generator" scheme has been developed. Frequency polygons and probability distribution functions of deviations in aircraft arrivals, obtained through statistical analysis, are presented in the paper.

Keywords: *Aircraft, algorithms, flights, simulation modelling, technological processes.*

1. INTRODUCTION

In civil aviation, there are concepts of flight regularity and departure regularity from airports. Flight regularity is determined by the scheduled departure or arrival time of the aircraft at its destination. Departure regularity from airports is determined by the actual departure time compared to the scheduled time. Analysis of the statistics regarding adherence to departure times of aircraft from airports according to the flight schedule shows that one of the significant causes of delays is deviations in the timing of individual technological operations preparing the aircraft for flight from the established norms. Consequently, there is a necessity to investigate the management processes of airport services responsible for carrying out individual technological operations in aircraft preparation for departure. This task belongs to the class of multi-criteria problems. Solving it using classical analysis methods is practically impossible due to its complexity. Simplifying the model could lead to erroneous results. Therefore, the authors have utilised the methodology of simulation modelling as an approach. Simulation modelling proves to be an effective tool for addressing multi-criteria problems associated with mass servicing systems.

This article proposes an approach to addressing the problem of improving operational management of the technological process of preparing an aircraft for departure, considering it as a multi-criteria task. The problem is tackled based on an imitation model in the form of a complex of modules. To achieve this, the technological process of preparing the aircraft for flight is decomposed into a series of local tasks (modules). The developed algorithms within this complex serve as the foundation for the development of an automated system for operational management of the technological process of preparing aircraft for a flight.

2. APPROACH TO DEVELOPING AN IMITATION MODEL

We will conceptualise the model as a set of relationships implemented by a system of blocks. To achieve this, we will decompose [1] the technological process of preparing the aircraft for departure into individual technological operations.

The decomposition diagram of the general task of operational planning of the technological process of flight servicing into individual tasks (technological operations) is presented in Fig. 1.

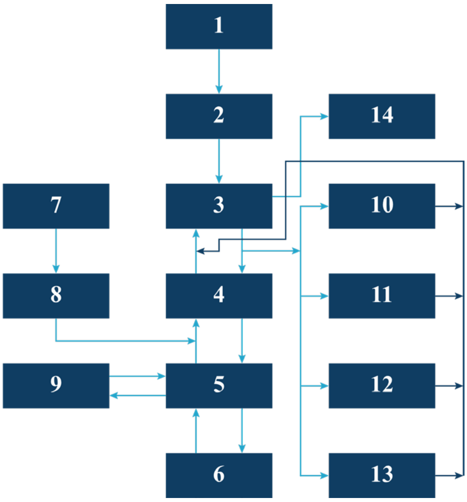

Fig. 1. Graph of the technological process of servicing a flight for the most general case – a transit flight: 1 – aircraft parking determination, 2 – aircraft technician, 3 – pushback tractor, 4 – gangway, 5 – passenger boarding, 6 – bus, 7 – passenger registration, 8 – storage, 9 – tanker, 10 – cargo, 11 – mail, 12 – catering, 13 – luggage, 14 – starting engines.

The sequence of calculations in the model corresponds to the natural sequence of performing technological operations. In this process, the time taken for the last operation determines the completion time of servicing the final flight and the departure time of transit or initial flights.

All indicators characterising the technological process will be grouped together:

1. **Input variables** include parameters characterising the current flight schedule at the airport;
2. **Model constants** are constant values that describe the technical characteristics of the airport and the facilities used for servicing flights;
3. The group of **control parameters** includes: the actual start and end times of servicing for a particular flight, start and end times of breaks in the operation of servicing facilities, and others;
4. **Output parameters** characterise the results of the system's actions and determine the values of target functions such as: departure regularity of aircraft, utilisation time of a particular servicing facility, flight delay magnitude, and others.

By combining the indicators characterising the technological process with the technological operations, we have obtained a complex of blocks [2], as shown in Table 1, each of which is described by a specific set of variables presented in groups.

Table 1. The Complex of Blocks of the Simulation Model

1	Arrival	9	Registration
2	Random Variable Generator	10	Passenger lounge/waiting department
3	Designation of parking lots	11	Luggage
4	Aircraft maintenance technician	12	Mail
5	Pushback tractor	13	Cargo
6	Bus	14	Refueller
7	Boarding stairs	15	Flight catering
8	Meeting and boarding	16	Departure

Based on the condition that the servicing of each individual flight is carried out strictly in accordance with the sequence of technological operations, we obtain the diagram of information flow between the blocks of the simulation model (Fig. 2). According to this diagram, the "Arrival" block (1) generates the initial data for the model based on the schedule of aircraft movements at the airport and the availability of servicing facilities for flights, considering aircraft types. In the "Gate Assignment" block (3), the task of allocating parking spaces for aircraft after their arrival is solved. Tasks such as determining the number of required servicing facilities for other technological operations, scheduling their operation, etc., are solved by blocks 4–14. The "Departure" blocks (15 and 16) simulate the engine start times and generate the protocol of airport model operation: flight departure delays are calculated, regularity values achieved at different threshold levels are determined, a table of local delays for technological operations, etc., is generated.

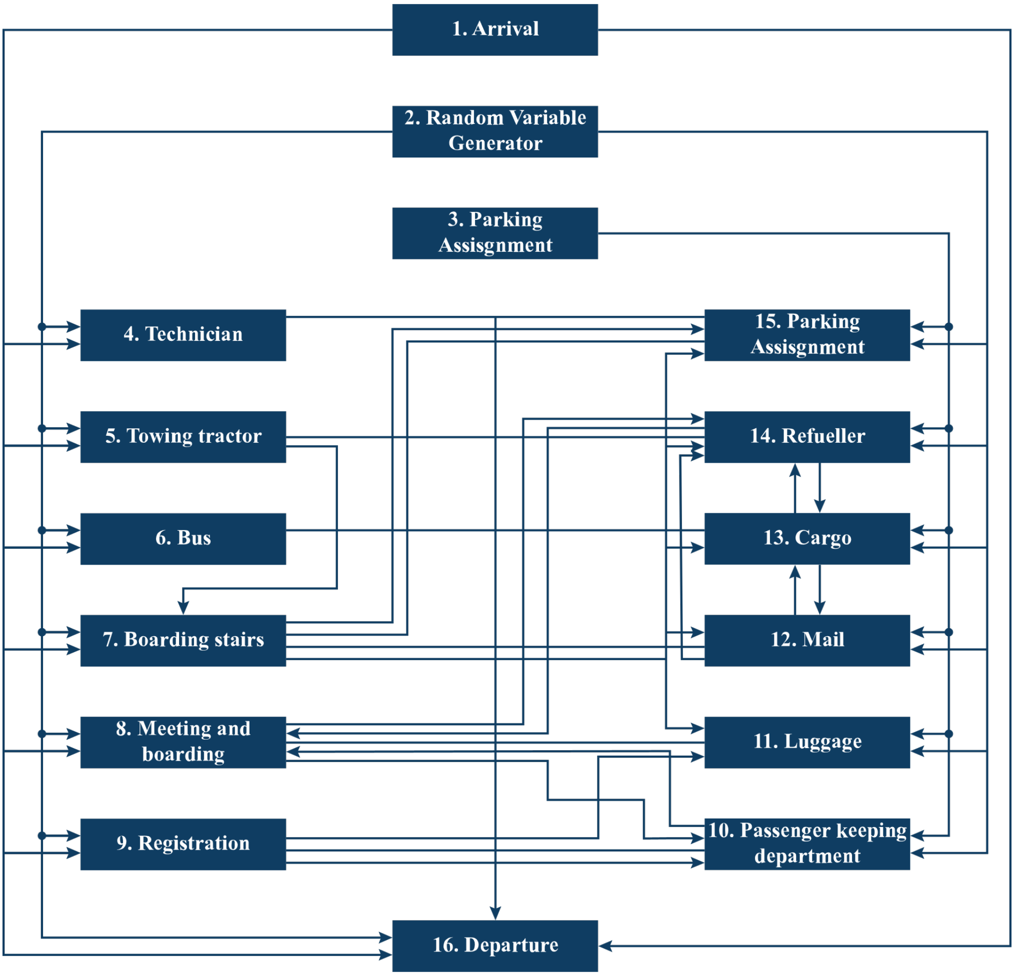

Fig. 2. Scheme of information connections between blocks in the simulation model.

As evidenced by experience, the completion times of practically all technological operations involved in preparing aircraft for a flight exhibit random characteristics [3], [4]. Therefore, to ensure the necessary fidelity of the model to real-world conditions, stochastic variables should be employed. To achieve this, a verification of the variables of the technological process involved in preparing aircraft for a flight for stochasticity was conducted.

3. VERIFICATION OF THE VARIABLES OF THE TECHNOLOGICAL PROCESS INVOLVED IN PREPARING AIRCRAFT FOR A FLIGHT FOR STOCHASTICITY

The primary input variable influencing the achievement of the main goal of airport operational management is the arrival time of aircraft. Deviations in arrival time from the scheduled time are influenced by various factors, among which meteorological conditions along the route and at departure and arrival airports, delays in aircraft servicing at the departure airport, etc., dominate. The nature of these deviations is determined using statistical analysis methods [5]. Data on the deviations between the actual arrival time of aircraft and the scheduled time were obtained based on the daily flight plans of the airport* (Due to confidentiality, airport-related data are not provided). The sample size comprised 1500 flights and ranged from minus (-) 50 minutes to plus (+) 80 minutes. Frequency polygons of arrival time deviations were constructed and investigated for intervals ranging from 3 to 12 minutes. As a result, a grouping interval of 9 minutes was used. With this approach, it is quite likely that the days of the week are relative to the schedule. An analysis of the homogeneity of samples was conducted, i.e., the hypothesis that the samples belong to the same population was tested. Different criteria were used to compare indicators measured under two different conditions on the same sample [6]. Initially, the authors chose the most lenient Wilcoxon criterion [7].

The Wilcoxon criterion is based on counting the number of inversions, where inversions are defined as follows: observations obtained in two samples are arranged in a combined sequence in ascending order of their values. If a value x from one sample precedes a value y from another sample in the combined ordered sequence, then this pair creates an inversion u.

When the size of the first sample is n and the second is m, if $n > 5$ and $m > 10$, the number of inversions is approximately normally distributed with a mean:

$$Mu = \frac{mn}{2} \tag{1}$$

with a variance:

$$Du = 1 + \frac{mn}{12}(m + n + 1) \tag{2}$$

Based on this criterion, the critical region of large absolute deviations was determined. However, during the analysis of various samples, there were instances where the values of inversions u did not fall within the critical region. Upon analysing different samples, it was found that all days of the week in the flight plan exhibited homogeneity in terms of flight deviations from the schedule. To refine the results, the hypothesis was tested using the more sensitive Kolmogorov-Smirnov criterion [8]. This is one of the most widely used statistical criteria, used to test hypotheses of the match between the distribution function of the investigated variable, constructed from the sample, with the distribution function in another sample or with the theoretical distribution function. This criterion is the most stringent as it identifies all types of distribution differences, not just those related to differences in specific parameters.

The statistic used to compare the two samples is the largest difference between the proportions of observations in both samples that do not exceed the same value. The investigation revealed that in our case, it is more appropriate to speak of three groups into which our data can be divided. As a result of the analysis, all data were grouped, and frequency polygons were calculated as follows:

Group I:
Tuesday, Wednesday, Thursday, Friday;

Group II:
Monday, Saturday;

Group III:
Sunday.

Frequency polygons of the grouped data are presented in Fig. 3.

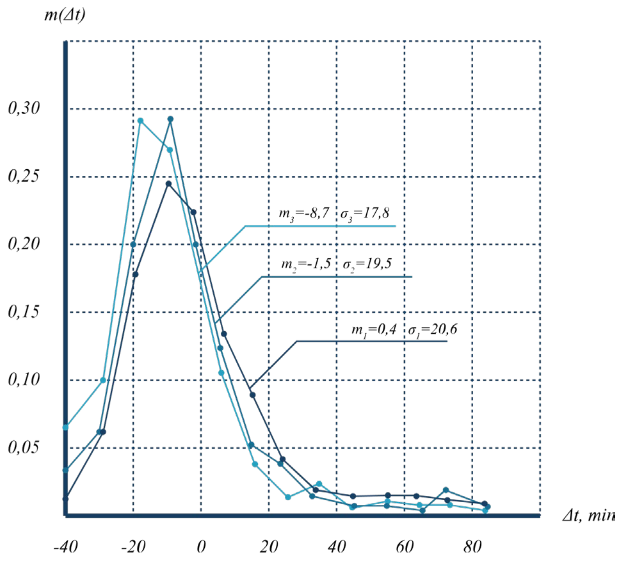

Fig. 3. Frequency polygons of aircraft arrival deviations.

As seen in Fig. 3, the numerical characteristics of the first and second groups are very close in terms of their first and second order moments: the means are m_1 = 0.4 minutes and m_2 = -1.5 minutes, while the standard deviations are σ_1 = 20.6 minutes and σ_2 = 19.5 minutes. The fact that the criterion rejected their homogeneity is presumably explained by differences in higher order moments. Based on the obtained results, empirical distribution functions were selected for use in the model, as presented in Fig. 4.

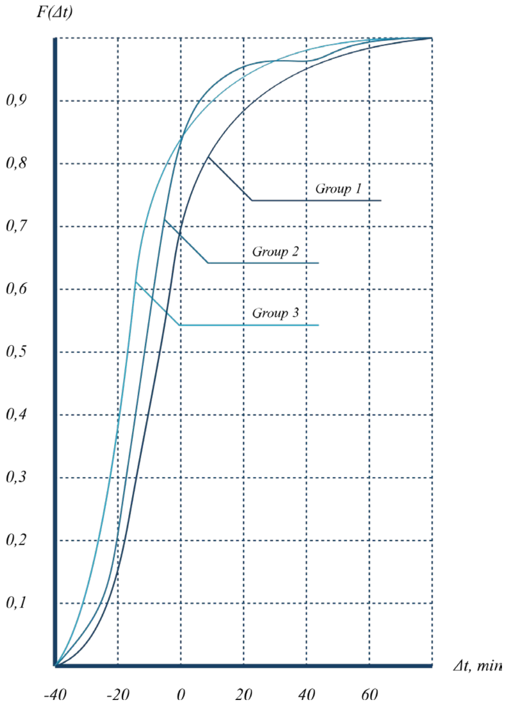

Fig. 4. Probability distribution functions of aircraft arrival deviations at the airport.

To construct the distribution functions, splines were chosen as the approximation tool, which are continuous up to the second derivatives inclusive at the "junctions" [9]. This allows for adjusting the model to approximate reality when using the simulation model. The "Random Variable Generator" is included in the scheme of information links between blocks of the simulation model in Fig. 2. It allows for model adjustment to approximate reality. It also provides the opportunity to adjust the initial data of the model, forming the basis for the operation of functional blocks, which allows predicting the operation of a set of technological processes for servicing flights at the airport. Additionally, to obtain results in operational problem-solving tasks of the model as a whole or its individual blocks, the "Random Variable Generator" may not be applied.

4. DEVELOPMENT OF THE "RANDOM VARIABLE GENERATOR"

During the development of the "Random Variable Generator", the authors proceeded from the condition that the duration of each operation in the technological process of aircraft preparation for a flight was determined by the performance of the servicing equipment used for these purposes, which depended on the volume and nature of the work. This time is set by technical documentation and serves as a standard for it. The actual duration of the equipment operation varies from flight to flight due to differences in the number of passengers, aircraft type, fuelling volume, time of day, etc. Therefore, the completion of each operation can be considered a random variable.

To confirm this circumstance, a chronometric study of the actual time for passenger check-in, boarding, baggage inspection, delivery to the aircraft, as well as boarding (disembarkation) time for aircraft of different types was conducted. Based on the obtained results, probability density functions of the deviations in operation duration from the normative were constructed, as shown in Fig. 5.

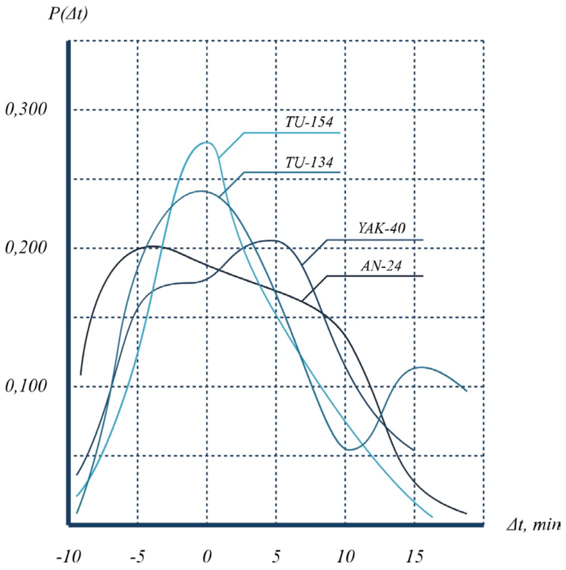

Fig. 5. Probability density function of deviations in the duration of servicing the flight by the passenger handling crew on board the aircraft.

The material obtained in this way allows for the construction of a generator for the time characteristics of the duration of individual technological operations for servicing flights of different types of aircraft at different times of the day, seasons, etc. With its help, adjustments to the model can be made to approximate it to reality. The block diagram of the generator is presented in Fig. 6.

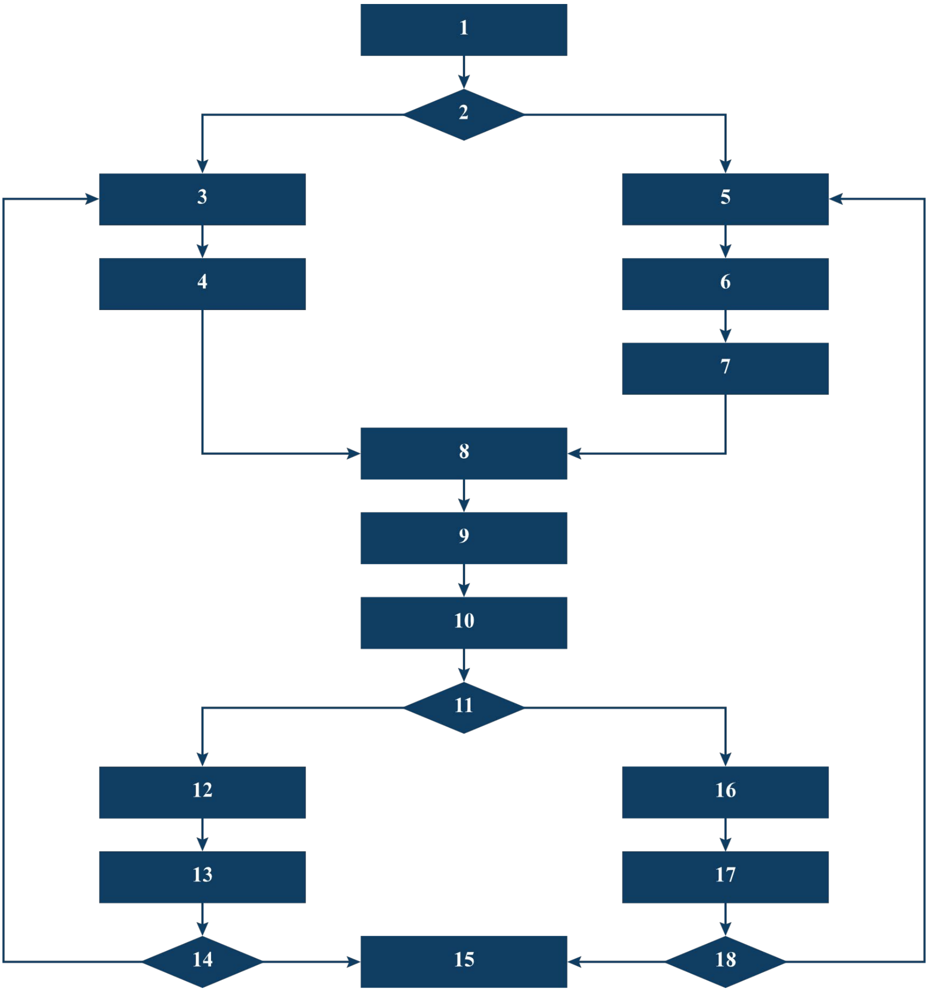

Fig. 6. Block diagram of the "Random Variable Generator".

The operation of the random variable generator is as follows. The generator is activated by Block (1). Subsequently, the type of variable is identified (2). If it concerns the arrival of an aircraft, the day of the week is determined (3), followed by the selection of the necessary distribution function (4). In the case of generating a random deviation value of the duration of a technological operation from the mean, the type of operation (5) and aircraft type (6) are defined, and the corresponding distribution function is chosen. Using the Pseudorandom Uniform Distribution Generator on the interval (0,1) (7), the ordinate value of the distribution function is realised (8). The spline function method (9) is applied to interpolate the value of the function between adjacent nodes and determine its value (10). Subsequently, deviations from normative values of variables are calculated (12, 16), and necessary adjustments are made to the arrival time of the flight or the completion of the technological operation (13, 17). Next, the need for further generation of random variables is checked (14, 18). If such need exists, control is transferred to Blocks (3) or (5). Otherwise, functional blocks of the model are excluded through module (15).

5. CONCLUSIONS

1. The approach based on simulation modelling is presented for investigating the multi-criteria problem of aircraft preparation for departure at an airport. The simulation model consists of a set of modules that combine related variables characterising the states of individual technological operations and transform them into processes.
2. The choice of simulation modelling methodology necessitated:
   - decomposing the overall task of operational planning of the technological process for aircraft preparation for a flight into an interconnected set of modules, reflecting the flow of individual technological processes;
   - developing the structure of connections between individual blocks, reflecting the informational and technological operations of aircraft preparation, and serving as the synthesising algorithm of the simulation model.
3. To ensure the necessary correspondence of the model to real conditions, a verification of the stochastic nature of the variables in the technological process of aircraft preparation for flights was conducted based on the daily flight plans of the airport, using the Wilcoxon and Kolmogorov-Smirnov criteria. The results of this study yielded frequency polygons of grouped data and selected empirical distribution functions for use in the simulation model.
4. Based on the timing of the duration of individual technological operations for servicing flights of different types of aircraft in various conditions, a scheme for the “Random Variables Generator” has been developed. With its help, it is possible to adjust the model to approximate it to reality. It also provides the ability to adjust the initial model data, serving as the basis for the operation of functional blocks. In cases where its use is not necessary, its deactivation is provided.

REFERENCES

1. Frini, A., Guitouni, A., & Martel, J. (2012). A General Decomposition Approach for Multi-Criteria Decision Trees. *European Journal of Operational Research, 220* (2), 452–460.
2. Brodsky, Yu., & Tokarev, V. (n.d.). Systems Analysis and Modeling of Integrated World Systems. *Fundamentals of Simulation for Complex Systems. Encyclopaedia of Life Support Systems* (vol. 1). Available at: https://www.eolss.net/Sample-Chapters/C15/E1-26-05-02.pdf

3. Andronovs, A., Chepurin, E., & Hajiyev, A. (2009). On Solving Statistical Problems for the Stochastic Processes by the Sufficient Empirical Averaging Method. *Statistical Models and Methods for Biomedical and Technical Systems*, 435–444. Boston, US: Birkhäuser. DOI:10.1007/978-0-8176-4619-6_30
4. Feoktistov, O. (2017). Basharina Automation of Queuing System Simulation Modeling in Grid, 2017 DOI: 10.21285/1814-3520-2017-12-105-113.
5. Stirzaker, D. (2005). *Stochastic Processes and Models*. Oxford University Press.
6. Birge, J. R., & Louveaux, F. (2011). Introduction to Stochastic Programming. *Springer Series in Operations Research and Financial Engineering*. DOI: 10.1007/978-1-4614-0237-4.
7. Hayes, A. (2023). *Wilcoxon Test: Definition in Statistics, Types, and Calculation Fundamental Analysis*. Available at: https://www.investopedia.com/terms/w/wilcoxon-test.asp
8. Justel, A., Peña, D., & Zamar, R. (1997). A Multivariate Kolmogorov–Smirnov Test of Goodness of Fit. *Statistics & Probability Letters, 35* (3), 251–259. DOI: 10.1016/S0167-7152(97)00020-5.
9. Vakal, L.P., & Vakal, E.S. (2019). Algorithm for Best Uniform Spline Approximation with Free Knots. *Cybernetics and Computer Analysis, 55* (3). (in Russian). Available at: http://dspace.nbuv.gov.ua/bitstream/handle/123456789/180875/13-Vakal.pdf?sequence=1